IMPLICATIONS FOR THE EPOCH OF REIONIZATION IN THE LOCAL UNIVERSE

by
Bingjie Wang

A dissertation submitted to The Johns Hopkins University in conformity with the requirements for the degree of Doctor of Philosophy

Baltimore, Maryland
October 2021

Abstract

The epoch of reionization is a critical phase transition in cosmic history, during which radiation from very early astronomical objects ionized the neutral hydrogen that once filled the entire universe. Direct observations of the ionizing process, however, are precluded by the neutral intergalactic medium at high redshift. In recent years, small samples of low-z galaxies that have hydrogen-ionizing (i.e., Lyman-continuum; LyC) photons escaping have been discovered, and clues have begun to emerge as to both the indirect signposts of LyC leakage and of the processes that enable the escape. We propose a new technique for finding LyC emitters (LCEs)—use the weakness of the [S II] nebular emission lines relative to typical star-forming galaxies as evidence that the interstellar medium is optically thin to the LyC. Significant LyC fluxes are detected in two out of three [S II]-deficient-selected star-forming galaxies at $z \sim 0.3$ using the Cosmic Origins Spectrograph onboard the Hubble Space Telescope (HST). We show that these galaxies differ in their properties from the benchmark sample of LyC-emitting Green-Pea galaxies at similar redshift: most notably, our sample is more massive. Statistical analyses are then performed with data recently available from the HST Low-redshift LyC Survey. We reaffirm the robustness of the [S II] diagnostic. Moreover, a complex relationship between optical emission-line properties and LyC

escape fractions is found. Considering little is known about the dependence of the escape fraction on galactic properties and circumgalactic environments, we take a closer look at the inner workings of galaxies—in particular, galactic outflows. Their radial structure is inaccessible by conventional absorption-line probes in "down-the-barrel" spectra. Hence we develop a novel method of combining information from the UV spectroscopy and the imaging of resonance absorption and fluorescence emission lines. We find that most of the outflowing material is likely created or injected at radii much larger than the starburst radius. This has important implications for our understanding of the regulating mechanism of the galactic baryonic cycle.

Thesis Readers:

Timothy M. Heckman (Primary Advisor)
Chair and A. Hermann Pfund Professor
Department of Physics and Astronomy
Johns Hopkins University

Marc P. Kamionkowski
William R. Kenan, Jr. Professor
Department of Physics and Astronomy
Johns Hopkins University

Colin A. Norman
Professor
Department of Physics and Astronomy
Johns Hopkins University

Henry C. Ferguson
Astronomer
Space Telescope Science Institute

Claus Leitherer
Astronomer
Space Telescope Science Institute

Acknowledgements

Three years ago to the date I met with my advisor, Tim Heckman, in his office as I was exploring new research fields, unaware of our conversations marking the beginning of my dissertation work. I am deeply grateful for his guidance into the study of extragalactic astronomy, and for his support over the years during my research. This dissertation could not have been written without him.

I would like to thank the rest of my thesis committee—Henry Ferguson, Marc Kamionkowski, Claus Leitherer and Colin Norman—for their insightful questions and comments during the presentation of my dissertation. Additionally, I appreciate the support from my advisory committee, Brice Ménard and David Neufeld, over the years post my candidacy exam.

Looking back, I owe a debt of gratitude to the two former advisors of mine. I thank Toby Marriage for helping me navigate the first two years of graduate school. I thank my undergraduate advisor, Arthur Kosowsky, for inspiring me, a philosophy student at the time, to embark on a journey of scientific inquiry. I also thank Simone Aiola, who, as a graduate student then, supported me as a teammate and as a mentor. I would not be determined to pursue a Ph.D. in Astrophysics without the wonderful experience of working with them during my time in Pittsburgh.

I am grateful to Danielle Berg and Alaina Henry for showing me how real observations were done during our trip to the MMT Observatory. I also would like to express my gratitude to my postdoctoral colleagues then: Kim Boddy, Ely Kovetz, and Vivian Poulin, from whose discussions I benefited greatly.

The path leading to a dissertation can be an isolating one, but I was fortunate enough to be accompanied by my fellow graduate students who made my time at Johns Hopkins some of the best years of my life. In particular, I would like to thank Hsiang-Chih Hwang and Canon Sun: my group mates during the TA orientation who have since become two of my closest friends. I thank my former roommate, Carol Hung, and semi-collaborator, Weichen Wang, for all the memorable time that we spent together. It has been a pleasure to be part of the "study group" with Sihao Cheng, Lingyuan Ji, and Cicero Lu: the days when we enjoyed dim sum and milk teas, and the nights when we chugged coffee and met deadlines will always be cherished in my memory. I also thank Micheal Busch for sharing my sarcasm, D'Arcy Kenworthy for preparing delicious dinners, and Duncan Watts for resolving many of the merge conflicts in our Git repository.

Five years of graduate school sounds like a long time, and yet the time flew by as I met friends and colleagues along the way sharing the ups and downs. While the above is a long list, it is incomplete, and I apologize to anyone who I have left out. I truly appreciate everyone's contribution to this dissertation, and I look forward to connecting again with everyone wherever life takes us.

Dedication

To my family and friends, the stars of my universe.

Contents

List of Tables

List of Figures

Chapter 1

Introduction

A coherent narrative of the cosmic history, in essence, entails linking two well observed and yet radically different views of the universe: a homogeneous and isotropic beginning seeded by small fluctuations as revealed by the cosmic microwave background (CMB; redshift $z \sim 1100$), and the current era where gravity has compressed gas and dark matter into large-scale structures. What happened in between—the dark ages when neutral hydrogen filled the entire universe ($1100 \lesssim z \lesssim 30$) and the epoch of reionization (EoR) when astronomical objects formed and ionized hydrogen—remains largely unexplored. Inferring the latter from the local universe is the focus of this dissertation.

This introductory chapter begins with the calculation of the evolution of the H II volume filling fraction in Section 1.1, and then proceeds with discussions of empirical constraints in Section 1.2. Section 1.3 makes the connection between observations and reionization models. It concludes with an overview of the rest four chapters in this thesis in Section 1.4.

1.1 The Cosmic Reionization

The evolution of the volume filling fraction of ionized hydrogen, $Q_{\rm HII}(z)$, is given by the differential equation

$$\frac{{\rm d}Q_{\rm HII}}{{\rm d}t} = \frac{\dot{n}_{\rm ion}}{\bar{n}_{\rm H}} - \frac{Q_{\rm HII}}{\bar{t}_{\rm rec}}, \tag{1.1}$$

where $n_{\rm ion}$ is the number of hydrogen-ionizing photons per comoving volume produced per unit time, $\bar{n}_{\rm H}$ is the mean comoving number density of hydrogen, and $\bar{t}_{\rm rec}$ is the recombination time. Equation 1.1 can be viewed as describing a competition between a source term proportional to the ionizing emissivity and a sink term due to recombinations (Madau et al., 1998). In what follows, we explain the two terms separately.

1.1.1 The Source Term

The cumulative output of ionizing photons per hydrogen atom by the ionizing sources is

$$\frac{n_{\rm ion}}{n_{\rm H}} = f_{\rm esc} f_\star n_{\rm ion} f_{\rm coll} \left(> M_{\rm min}\right), \tag{1.2}$$

under two assumptions. First, each dark matter halo above a certain minimum mass $M_{\rm min}$ hosts a galaxy. Second, helium, which would have induced an order unity correction coefficient, is neglected.

The fraction of ionizing photons that escape the host halo and make it into the intergalactic medium (IGM), $f_{\rm esc}$, likely depends on each galaxy's configuration of the interstellar and the circumgalactic medium, as well as the host halo mass. Here all those complexities are encapsulated into this single parameter. $f_\star$ is the fraction of

baryons in the halo that have been converted into stars. In the simplest case, we can assume that each halo contains the universal cosmic baryon fraction. The number of ionizing photons produced per baryon converted into stars, $n_{\rm ion}$, depends on the initial mass function (IMF) and metallicity of stellar populations. The hot, massive, and short lived OB stars are widely thought to supply the ionizing photons, although metal-free Pop III stars may also contribute to $n_{\rm ion}$. The fraction of matter that has collapsed into halos above $M_{\rm min}$, $f_{\rm coll}(> M_{\rm min})$, is related to the mass function of halos at a given redshift, z, as

$$f_{\rm coll}(> M_{\rm min}, z) = \frac{1}{\rho_{\rm m0}} \int_{M_{\rm min}}^{\infty} {\rm d}M M \frac{{\rm d}n(z)}{{\rm d}M}, \tag{1.3}$$

where $\rho_{\rm m0}$ is the matter density today, and ${\rm d}n(z)/{\rm d}M$ is the halo mass function (e.g., Sheth et al. 2001). An estimate on $M_{\rm min}$ can be made by considering the virial temperature, $T_{\rm vir}$, required for star formation. Rearranging Equation 26 in Barkana and Loeb (2001), we obtain their relationship at a collapse redshift z

$$M_{\rm min} = \frac{7030.97}{h} \sqrt{\frac{\Omega_m^z}{\Omega_m} \frac{1}{\Delta_c}} \left[\frac{T}{(1+z)\mu} \right]^{\frac{3}{2}} \tag{1.4}$$

$$\Delta_c = 18\pi^2 + 82d - 39d^2, \tag{1.5}$$

where $M_{\rm min}$ is in solar mass, Δ_c is the non-linear over-density relative to the critical density at the collapse redshift (Bryan and Norman, 1998), $d \equiv \Omega_m^z - 1$, and μ is the mean molecular weight. At very high redshifts, gas can cool and ultimately fragment and form stars via the atomic cooling mechanism in haloes of $T_{\rm vir} \gtrsim 10^4$ K, which corresponds to an $M_{\rm min} \sim 10^8 M_{\odot}$.

1.1.2 The Clumping Factor

Turning now to the recombination term in Equation 1.1, the recombination rate scales as the particle density squared; hence it varies thoroughout the inhomogeneous IGM. The clumping-factor approach introduces one parameter to express the IGM inhomogeneity, so that the average time between recombinations can be approximated as

$$\bar{t}_{\rm rec} = \frac{1}{C_{\rm H\ II}\alpha_\beta(T_0)\bar{n}_{\rm H}(1+Y/4X)(1+z)^3} \tag{1.6}$$

$$\approx 0.93{\rm Gyr}\left[\frac{3}{C}\right]\left[\frac{1+z}{7}\right]^{-3}\left[\frac{T_0}{2\times10^4{\rm K}}\right]^{0.7}, \tag{1.7}$$

where α_β is the case-B hydrogen recombination coefficient suitable for the optically thick condition, and T_0 is the IGM temperature at mean density (Kuhlen and Faucher-Giguère, 2012). While both $C_{\rm H\ II}$ and T_0 remain uncertain, studies suggest $C_{\rm H\ II} \sim 1-3$ (McQuinn et al., 2011) and $T_0 \sim 2\times10^4$ K (Hui and Haiman, 2003) during the EoR.

We note that this approach is insufficient for understanding the spatial distribution of the ionized gas, since the clumping factor is not designed to reveal the environments in which absorptions happen. Specifics in the reionization process such as spectra of ionizing sources and the intensity of the ultraviolet (UV) radiation field that incidents on dense regions would need to be considered instead.

1.2 Empirical Constraints

Direct constraints on the reionization process are difficult to obtain. Therefore observations tend to probe the total ionizing radiation coming from galaxies as a product of three quantities

$$\dot{n}_{\rm ion} = f_{\rm esc}\xi_{\rm ion}\rho_{\rm UV}, \tag{1.8}$$

where $\xi_{\rm ion}$ is an efficiency factor in converting the UV luminosity to LyC emission, and $\rho_{\rm UV}$ is the rest-frame UV luminosity density at around 1500 Å. In this section we elaborate on each of the terms in Equation 1.8, in the decreasing order of the degree of being constrained.

1.2.1 UV Luminosity Density

The common method for determining the UV luminosity density $\rho_{\rm UV}$ is to search for high-z galaxies, and then construct the UV luminosity function. The latter is typically parameterized by a Schechter function

$$\frac{{\rm d}n}{{\rm d}L} = \phi(L) = \frac{\phi^\star}{L^\star}\left(\frac{L}{L^\star}\right)^\alpha e^{-L/L^\star}, \tag{1.9}$$

where $\phi^\star$ is the characteristic volume density, $L^\star$ is the characteristic luminosity, and α is the faint end slope (Schechter, 1976). The luminosity function is extrapolated and integrated from the lowest to the highest luminosities that galaxies can attain to obtain

$$\rho_{\rm UV} = \int_{L_{\rm min}}^{L_{\rm max}} \phi(L){\rm d}L. \tag{1.10}$$

The 2012 Hubble Ultra Deep Field campaign results in $\rho_{\rm UV} \approx 10^{26}\,{\rm erg\,s^{-1}\,Hz^{-1}\,Mpc^{-3}}$

at $z \sim 7$, declining to $\rho_{\rm UV} \sim 3.2 \times 10^{25}\,{\rm erg\,s^{-1}\,Hz^{-1}\,Mpc^{-3}}$ at $z \sim 8$ (Ellis et al., 2013; Koekemoer et al., 2013). Firm lower limits on $\rho_{\rm UV}$ are also established in subsequent studies (Robertson et al., 2013; Finkelstein et al., 2015; Bouwens et al., 2021).

1.2.2 Production Efficiency per Unit UV Luminosity

The efficiency factor, $\xi_{\rm ion}$, is defined as the number of hydrogen-ionizing photons produced per second divided by the emergent far-UV luminosity at 1500 Å. It depends on the UV continuum slope β, where β is defined such that $f_\lambda \propto \lambda^\beta$ (Dunlop et al., 2013). By leveraging stellar population synthesis models of Bruzual and Charlot (2003) and the dust model of Charlot and Fall (2000), Robertson et al. 2015 obtain $\xi_{\rm ion} \sim 10^{25.2}\,{\rm erg\,s^{-1}\,Hz^{-1}}$. This is consistent with the direct estimate from $z = 4 - 5$ galaxies based on Hα (Bouwens et al., 2016).

1.2.3 Escape Fraction of Ionizing Photons

The fraction of hydrogen-ionizing photons that escape galaxies, $f_{\rm esc}$, is the least constrained parameter. Its direct measurement during the EoR is precluded by the neutral IGM. Searching for candidate galaxies having ionizing photons escaping at $z \sim 3$ is prone to foreground contaminations. A few detections have been confirmed (Mostardi et al., 2015; Vanzella et al., 2015, 2018). On the other hand, certain progress has been made in the low-redshift searches ($z \sim 0.3$; Borthakur et al. 2014; Izotov et al. 2016a; Leitherer et al. 2016; Wang et al. 2021). The fiducial value of $f_{\rm esc}$ is usually taken to be ~ 0.2. However, the likely dependences of it on galaxy mass, age, star formation history or other properties are yet to be understood.

1.3 Drivers of Reionization

Having reviewed the basics for the reionization process in Section 1.1 and empirical constraints in Section 1.2, this section completes the picture with a discussion on selecting reionization models. We start with the optical depth to reionization.

The free electrons that are made readily available during the EoR interact with CMB photons via Thomson scattering. The probability that a given photon scatters is related to an effective optical depth to reionization τ. This optical depth can be calculated from $Q_{\rm HII}$ as

$$\tau = \int_0^\infty \frac{c(1+z^2)}{H(z)} Q_{\rm HII}(z) \sigma_T \bar{n}_{\rm H} (1 + \eta Y/4X) {\rm d}z, \tag{1.11}$$

where $H(z)$ is the Hubble parameter, and σ_T is the Thomson scattering cross section. Conventionally helium is taken to be singly ionized ($\eta = 1$) for $z > 4$ and doubly ionized ($\eta = 2$) at lower redshift. By examining whether the ionization rate provided by star-forming galaxies can reproduce the optical depth as measured from the CMB, we can test for different reionization models.

The consensus model is that galaxies drive reionization (Madau et al., 1999). The high value of $\tau = 0.089 \pm 0.014$ given by WMAP (Bennett et al., 2013) creates some tension since it requires the presence of a large population of star-forming galaxies at $z \simeq 10 - 15$, in conflict with a decline in $\rho_{\rm UV}$ for $z > 8$ (Oesch et al., 2014; McLeod et al., 2016). However, a lower value of $\tau = 0.054 \pm 0.007$ is later provided by Planck (Planck Collaboration et al., 2020b). The conventional model of faint, star-forming galaxies dominating the reionization process thus remains to be favored (Bouwens et al., 2015; Robertson et al., 2015; Ishigaki et al., 2018).

It is worthy noting that non-conventional models have been proposed given recent progress coming from both observation and simulation fronts. The discovery of a significant population of faint active galactic nuclei (AGNs) at $4 < z < 6.5$ (Giallongo et al., 2015) indicates that it is possible for quasars and AGNs to dominate the reionization process at all epochs (Madau and Haardt, 2015). In addition, simulations suggest that reionization can be prompted by massive galaxies. In one of those models, roughly 5% of the star-forming galaxies with the highest masses and UV luminosities can account for over 80% of the reionization budget (Naidu et al., 2020).

1.4 Organization of the Dissertation

Given the scientific interest in reionization and its relationship with galactic evolution, this dissertation presents new techniques to study the reionization process. It is a compilation of three original contributions to the subject, each deliberated in a separate chapter. The content of each chapter was published in The Astrophysical Journal (Wang et al., 2019; Wang et al., 2020, 2021)[1]. As such, each chapter is self-contained, and a more specific introductory remark is given at the beginning of the respective chapter.

We now outline the organization of this dissertation. In Chapter 2, we present the results of a pilot program aimed to test a new technique for finding LyC-emitting galaxies—using the weakness of the [S II] nebular emission lines relative to typical star-forming galaxies as evidence that the interstellar medium is optically thin to the LyC. We use the Cosmic Origins Spectrograph (COS) on the HST to detect signifi-

[1] © The American Astronomical Society

cant emerging flux below the Lyman edge in two out of three [S II]-weak star-forming galaxies at $z \sim 0.3$. We show that these galaxies differ markedly in their properties from the class of leaky "Green-Pea" galaxies at similar redshifts: our sample galaxies are more massive, more metal-rich, and less extreme in terms of their stellar population and the ionization state of the interstellar medium. Like the Green Peas, they have exceptionally high star-formation rates per unit area. They also share some properties with the known leaky galaxies at $z \sim 3$, but are significantly dustier.

In Chapter 3, we show that the [S II] deficiency is an effective method to select LyC-leaking candidates using data from the Low-redshift LyC Survey, which has detected flux below the Lyman edge in 35 out of 66 star-forming galaxies with the HST/COS. We show that LyC leakers tend to be more [S II] deficient and that the fraction of their detections increases as [S II] deficiency becomes more prominent. Correlational studies suggest that [S II] deficiency complements other LyC diagnostics such as strong Lyman-α emission and high [O III]/[O II]. Our results validate a new way to identify local laboratories for exploring the processes that made it possible for galaxies to reionize the universe.

In Chapter 4, we take a closer look at galaxies themselves. We probe the structure of galactic outflows in low-z starbursts by using a combination of UV spectroscopy and imaging of the fluorescence emission lines (associated with transitions to excited fine-structure levels) and spectroscopy of the corresponding strongly blue-shifted resonance absorption lines. We find that in the majority of cases the observed fluorescence emission lines are much weaker and narrower than the absorption lines, originating in the star-forming interstellar medium and/or the slowest-moving part of the inner outflow. In a minority of cases, the outflowing absorbing material does make a significant

contribution to the fluorescence emission. These latter systems are characterized by both strong Lyα emission lines and weak low-ionization absorption lines (both known to be empirical signs of LyC leakage). We argue that the observed weakness of emission from the outflow seen in the majority of cases is due to the missing emission arising on scales larger than those encompassed by the HST/COS aperture. This implies shallow radial density profiles in these outflows, and suggests that most of the observed absorbing material must be created/injected at radii much larger than that of the starburst. This has important implications for our understanding of both the physics of galactic outflows and for our estimation of their principal properties.

In Chapter 5, we share final thoughts on the progress being made in galaxy formation and the reionization of the universe. We also briefly discuss potential improvements coming from future observations and simulations.

Chapter 2

A New Technique for Finding Galaxies Leaking Lyman-continuum Radiation: [S II] Deficiency

2.1 Introduction

The Epoch of Reionization (EoR) is the period during which the first stars are formed and emit light that ionizes the intergalactic medium (IGM). The history of reionization is primarily inferred from two measurements: large-scale anisotropies in polarization of the cosmic microwave background (CMB) and spectroscopy of distant quasars. The CMB is affected by the total column density of free electrons along the line of sight. The parameterization of its Thomson scattering optical depth τ remains the

least constrained parameter in the ΛCDM model (e.g. Bennett et al. 2013; Planck Collaboration et al. 2020a). Observations of quasar absorption lines via the Gunn-Peterson effect (Gunn and Peterson, 1965) set the limit that reionization is complete by $z \sim 6$ (e.g. Fan et al. 2006; Fan et al. 2006; McQuinn 2016, and references therein).

A conventional picture thus depicts the history of reionization as early galaxies reionizing hydrogen between $z \sim 12$ to 6, and followed by quasars reionizing helium. While deep imaging with the Hubble Space Telescope (HST) indicates that the ultraviolet (UV) luminosity density of early star-forming galaxies is high enough that they are the best candidates to provide the ionizing photons necessary for reionizing the Universe (e.g., Bouwens et al. 2016), the fraction of Lyman-continuum (LyC) photons that actually escape from the galaxies into the IGM, which is required to be significant (> 0.2), is the biggest uncertainty (e.g., Robertson et al. 2015). Unfortunately, since the universe during the EoR is opaque to ionizing photons, direct observations that access the LyC at these redshifts are impossible. Identifying leaky galaxies at low redshifts thus becomes an important step in the investigation into the physical processes that allow LyC photons to escape, as well as in identifying indirect observational signposts of leaky galaxies during the EoR. In addition, we gain sensitivity by looking at local galaxies, which naturally makes the relevant analysis easier.

Over the past few years, convincing detections of escaping LyC photons in a relatively small number of low-redshift starburst galaxies have emerged (Borthakur et al., 2014; Izotov et al., 2016a,b, 2018a,b; Leitherer et al., 2016). The proposed signposts include a high star formation rate (SFR) per unit area, strong nebular emission lines, high flux ratios of the [O III] 5007/[O II] 3727 emission lines, and strong Lyα emission. In this paper, we present a new and independent signpost of

leakiness that could also be measured by future observations of galaxies during the EoR by the James Webb Space Telescope (JWST).

The new signpost is the relative weakness of the [S II] 6717,6731 emission lines, defined with respect to typical star-forming galaxies. This [S II] deficiency is a tracer of gas that is optically thin to ionizing radiation, allowing the escape of LyC photons. Given that the ionization potential for producing [S II] is only 10.4 eV, which is significantly less than a Rydberg, much of the [S II] emission therefore arises in the warm partially-ionized region near and just beyond the outer edge of the Stromgren sphere in a classical H II region. In an H II region that is optically thin to ionizing radiation, this partially ionized [S II] zone is weak or even absent, and the relative intensity of the [S II] emission lines drop significantly as a result (Pellegrini et al., 2012).

In this paper, we validate this idea using HST far-UV observations with the Cosmic Origins Spectrograph (COS; Green et al. 2012) of a sample of three star-forming galaxies. The structure of this paper is as follows. In Section 3.2, we begin by detailing our definition of the [S II] deficiency. In Section 4.2, we summarize the observational data sets, including sample selection, data processing and analysis, and measured ancillary parameters. In Section 2.4, we present our results, namely the escape fractions for the LyC. In Section 2.5, we make comparisons of our galaxies to other known leaky galaxies at both low and high redshift selected in other ways, and assess the various indirect indicators of leakiness. We summarize our conclusions in Section 2.6.

Throughout we adopt the best-fit cosmological parameters from the Planck 2018 analysis (their TT,TE,EE+lowE+lensing+BAO case): $H_0 = 67.66$ km s^{-1} Mpc^{-1},

$\Omega_M = 0.311$, and $\Omega_\Lambda = 0.690$ (Planck Collaboration et al., 2020b).

2.2 Definition of [S II] Deficiency

The [S II] deficiency is established with respect to the sample of SDSS DR 12 star-forming galaxies in the plane of [S II] 6717,6731/Hα versus [O III] 5007/Hβ as shown in Figure 2.1. Here we describe the procedure as follows.

First we select all the galaxies classified as "star forming" in the value added catalog provided by the Portsmouth group (Thomas et al., 2013), with a signal-to-noise cut of five in the flux measurements. We then bin the data in log([O III]/Hβ) and make a histogram in log([S II]/Hα) for each bin, which is subsequently fitted with a Gaussian (or a skewed Gaussian in a few cases) to determine the peak location. Lastly we perform a polynomial fit to the peaks. This is shown as the black dotted curve in Figure 2.1. The resulting fitting formula is

$$\begin{aligned} y &= -0.487 + 0.014\xi + 0.028\xi^2 - 0.785\xi^3 \\ &\quad -3.870\xi^4 + 0.446\xi^5 + 8.696\xi^6 + 0.302\xi^7 \\ &\quad -6.623\xi^8 \end{aligned} \tag{2.1}$$

where ξ is the line ratio of log([O III]/Hβ), and y is the line ratio of log([S II]/Hα).

We define the [S II] deficiency as a galaxy's displacement in log([S II]/Hα) from the ridge line, denoted as Δ[S II]. Uncertainties in the emission-line ratios for individual galaxies are less than 0.1 dex. Uncertainties in the location of the ridge line are negligible except where the data are sparse. In these cases, we estimate uncertainties

via bootstrap. These are shown in gray in Figure 2.1.

2.3 Data

2.3.1 Sample Selection

In the HST program GO-15341 (PI T. Heckman) we observed a sample of five galaxies selected in the SDSS DR7 plus GALEX GR6 catalogs based on the following criteria.

1. An [S II] deficiency relative to normal star-forming galaxies of at least 0.2 dex as shown in Figure 2.1. In this paper the value of Δ[S II] for J1242 is just below 0.2 dex. This is because, since the original sample definition, we updated the sample of normal galaxies to SDSS DR 12, which results in a slight change in the ridge-line.

2. A seeing-de-convolved half-light radius of less than 0.5″ (typically smaller than 1 kpc) based on SDSS u-band images. This mimics the small sizes of galaxies in the EoR.

3. An estimated far-UV flux inside the COS aperture of larger than 2×10^{-16} $s^{-1}\,cm^{-2}\,Hz^{-1}\,sr^{-1}$. This was derived by using SDSS u-band images to make an aperture correction to the GALEX far-UV flux.

4. Redshifts higher than 0.26. This ensures that the Lyman edge falls at wavelengths over which the COS has high sensitivity ($>$ 1150 Å).

5. An SDSS optical spectrum dominated by a starburst (not an active galactic nucleus).

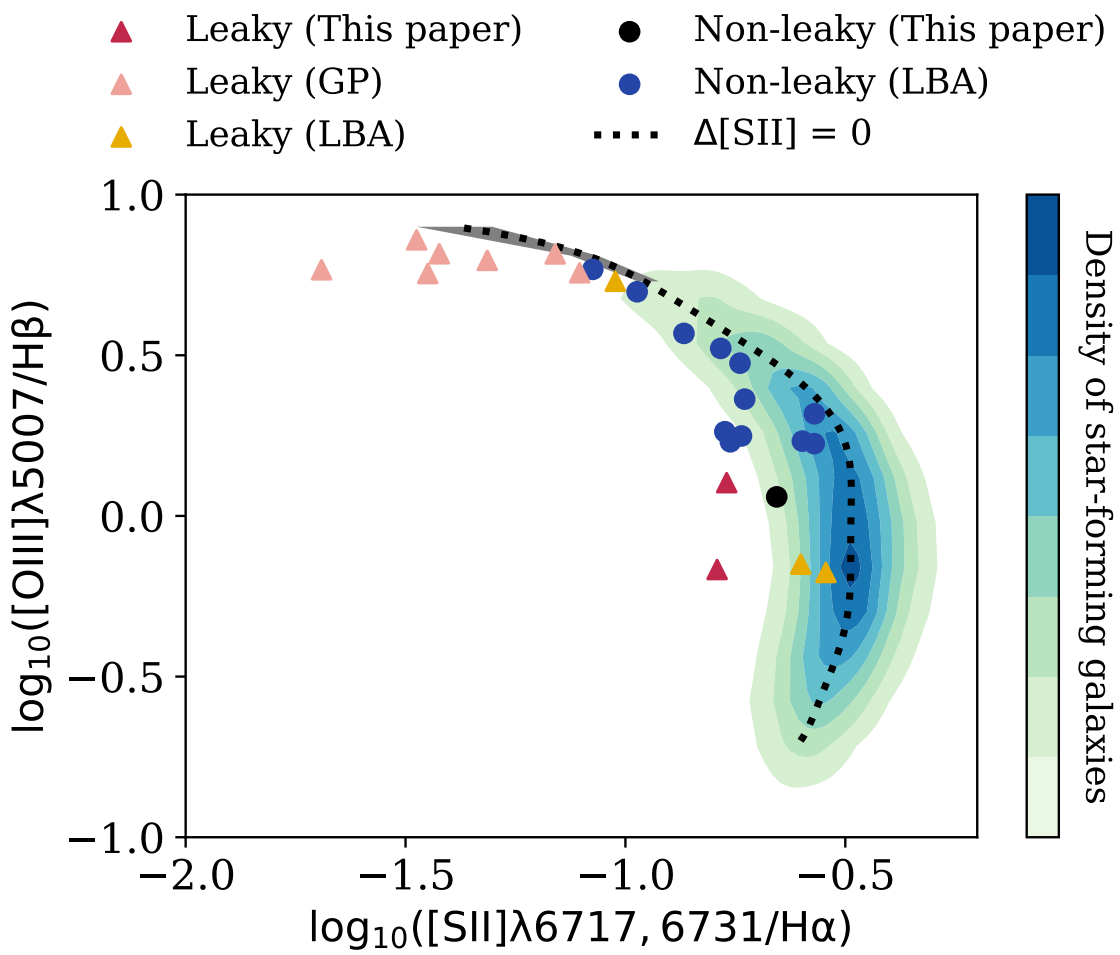

Figure 2.1: Definition of [S II] deficiency, where the flux ratio of [S II] 6717,6731/Hα is plotted against that of [O III] 5007/Hβ. The contours show the density distribution of the SDSS DR 12 star-forming galaxy sample. The black dotted line is fitted to the locus of the peak density of this distribution. The [S II] deficiency is defined as a galaxy's displacement in log([S II]/Hα) from this ridge line. Uncertainties in the ridge line are negligible except in the upper left, where they are indicated in gray. The red triangles represent the two leaky star-forming galaxies of this paper, while the black dot represent the non-leaky one. Also plotted are leaky Green Pea galaxies in Izotov et al. (2016a,b, 2018a,b) (pink triangles) and Lyman break analogs in Alexandroff et al. (2015) (orange triangles and blue dots), both of which are discussed in Section 2.5.

Table 2.1: Observation Logs

	Galaxy	z	COS FUV Grating
J2226	SDSSJ222634.07-090106.2	0.299	G140L
J1119	SDSSJ111905.27+592514.1	0.290	G140L
J0910	SDSSJ091021.35+610550.2	0.272	G140L
J1432	SDSSJ143256.4+274249.6	0.266	G140L
J1242	SDSSJ124206.24+011537.5	0.271	G140L
	COS NUV ACQ Image Exposure Time (s)	Exposure Time (s)	Date of HST Observation
J2226	241	7681.728	2018-05-25
J1119	120	5502.720	2018-09-26
J0910	161	8336.640	2018-09-21
J1432	97	5100.704	2018-06-25
J1242	161	7832.864	2018-08-10

The resulting sample is listed in Table 2.1. Subsequent observations with the COS show that, in the first two galaxies (J2226 and J1119), the far-UV spectrum is dominated by light from a quasar (a featureless continuum and a strong and very broad Lyα emission line), even though the SDSS optical spectrum is dominated by a starburst. We do not discuss these targets further in this paper. For the three remaining targets, we will demonstrate that they are indeed dominated by starlight in the far-UV by using the fit of Starbust99 (hereafter SB99; Leitherer et al. 1999) model spectra in Section 2.3.3.

2.3.2 Data Processing

All the COS far-UV spectra were obtained using the G140L grating in the 1105 setting. This covers the observed wavelength range from 1110 to 2150 Å, corresponding

to roughly 880 - 1690 Å in the rest frame. The spectral resolution is about 0.5 Å.

We first retrieve our COS data from the MAST archive which had been processed through the standard COS pipeline `CalCOS`. The most technically challenging part of the data analysis is trying to accurately subtract the dark counts, which contribute significantly to the net counts in the region of the LyC. Therefore, following the procedure in the Appendix of Leitherer et al. (2016), we create a super-dark image to replace the standard COS pipeline version. A super-dark image for a given galaxy is obtained by selecting all the COS dark frames taken within ± 1 month of the target observing time, and taking an average. The choice of ± 1 month is due to the fact that there are temporal fluctuations in the dark count rate. We therefore turn off the native background correction in `CalCOS`, and modify the procedure to subtract the super-dark from the science exposure just before extraction of the spectrum.

By examining the individual dark frames that were used to create a given super-dark, we estimate that the temporal variations in the dark count rate lead to an uncertainty in the dark count rate at the time of the observations of ± 17%. This will be one factor in the accuracy of our measurement of the escaping LyC flux described below.

We also test possible contamination of the galaxy spectra below the Lyman edge due to scattered light in the wings of the Lyα airglow lines, or other weak emission. To do so, we compare an average of five G140L exposures of blank fields provided by the COS team with our spectra. This comparison is shown in Figure 2.2, and establishes that there is no significant sky contamination below the Lyman limit.

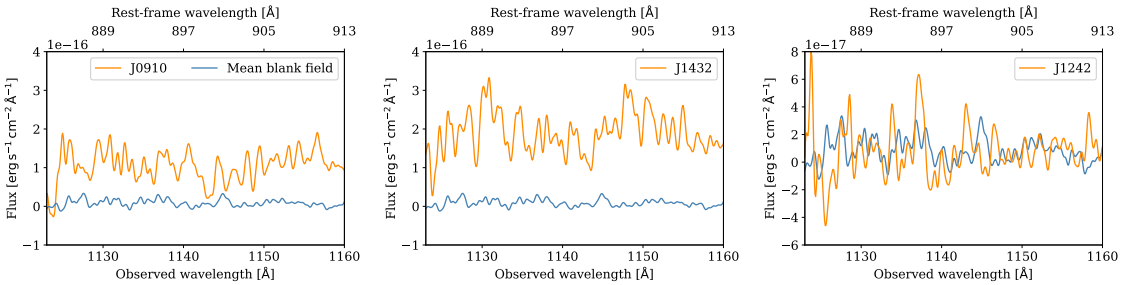

Figure 2.2: Observed spectra plotted in the region below the Lyman limit after super-dark subtraction. The orange lines are the COS spectra of our three galaxies, while the blue line is the average of five G140L exposures of blank fields. Note that the blank sky spectrum shows no contaminating signal.

2.3.3 Data Analysis

Given the relatively low signal-to-noise ratio in the extracted spectra, we smooth all the spectra used with a Gaussian kernel before further analysis. The full width at half maximum of the kernel is chosen to be about 0.5 Å to reach the native resolution.

For each spectrum, we first correct for Milky Way (MW) extinction in the observed frame using the reddening law proposed in Mathis (1990), and $E(\mathrm{B}-\mathrm{V})_{\mathrm{MW}}$ taken from the NASA Extragalactic Database for a given position on the sky. We then transform the observed spectra to the rest frame of the galaxy using SDSS spectroscopic redshifts, conserving the quantity λF_λ.

Synthetic spectra are generated based on stellar evolutionary synthesis models using SB99. We produce our models based on a star formation history of a continuous and constant rate of star formation. The stellar population is parameterized by a Kroupa initial mass function (IMF; Kroupa 2001). The stellar population evolves from the zero-age main sequence using the evolutionary models of the Geneva Group. The model spectra are described in detail in Leitherer et al. (2010). In all, we generate

eight sets of SB99 models based on two choices each for burst age (10^7 and 10^8 yr), metallicity (solar or 1/7 solar), and whether or not models using stellar rotation are employed.

A model spectrum is interpolated into the same wavelength array as its corresponding COS spectrum, and also convolved with the same Gaussian kernel, ensuring that they have the same resolution. A best fit is chosen by eye; more specifically, we closely examine the match between the synthetic and observed spectra of the two strong stellar wind features due to O VI 1032,1038 and N V 1238,1242. These P-Cygni features trace the most massive stars, which are the ones responsible for producing most of the ionizing continuum. For O VI we could only examine the redshifted emission component, as the blueshifted absorption is contaminated by the [O I] airglow line. From these comparisons, we find that the best fits for J0910 and J1432 come from the solar metallicity models that have ages of 10^7 yr, and that incorporate stellar rotation, while J1242 is better fitted with a 10^8 yr model. The overall best fits are shown in Figure 2.3, and a zoom-in on these wind lines is shown in Figure 2.4. As seen from the figures, each stellar spectrum alone is a good fit to the data, and hence we infer that the far-UV light in all three targets is in fact dominated by hot massive stars. The only stellar feature the model does not fit well is the blend of the Ş1176 and the Ą/N IV 1169 lines. We are exploring this and will describe the results in a future paper dealing with the stellar populations in these galaxies.

Having chosen a model, we then vary the internal (extragalactic) extinction, $E(\mathrm{B-V})_{\mathrm{int}}$, as a free parameter until the slope of a given observed spectrum matches its SB99 model. To do so, we use the extragalactic reddening law derived in Calzetti et al. (1999). There is an alternative proposed by Reddy et al. (2015, 2016), which

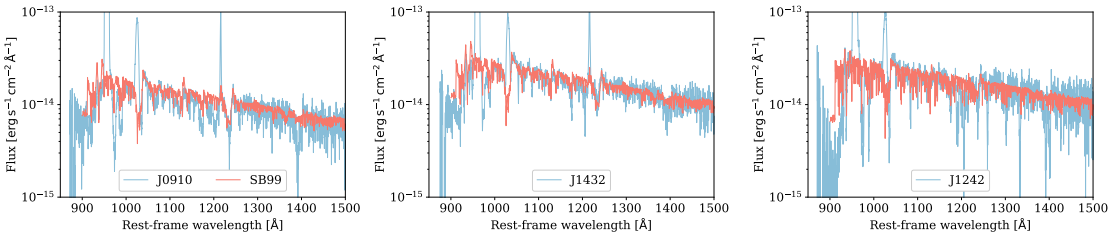

(a) (b) (c)

Figure 2.3: Spectra of the three star-forming galaxies with Milky Way extinction and internal extinction removed (in blue), and over-plotted with SB99 best fits (in coral). The extinction values are: (a) $E(\mathrm{B-V})_{\mathrm{MW}} = 0.041$, $E(\mathrm{B-V})_{\mathrm{int}} = 0.239$; (b) $E(\mathrm{B-V})_{\mathrm{MW}} = 0.016$, $E(\mathrm{B-V})_{\mathrm{int}} = 0.243$; and (c) $E(\mathrm{B-V})_{\mathrm{MW}} = 0.016$, $E(\mathrm{B-V})_{\mathrm{int}} = 0.314$.

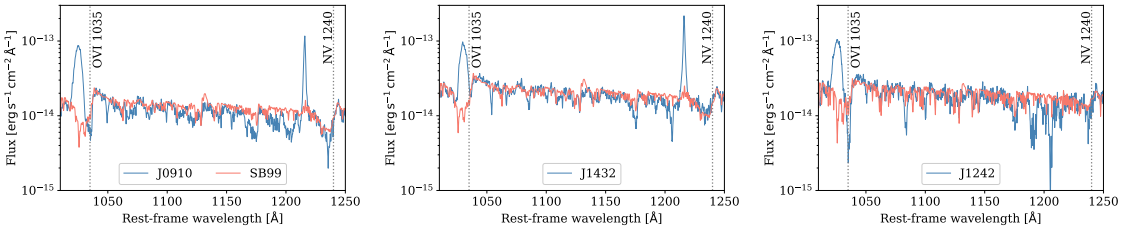

(a) (b) (c)

Figure 2.4: Same as Figure 2.3, but zooming in on the O VI and N V stellar wind lines, which are used for deciding the best-fit SB99 model spectra. The strongest residuals (data minus model) are due to the O I telluric airglow emission, Lyα emission, and interstellar absorption lines.

Table 2.2: Measured Ancillary Parameters

	$\mathrm{SFR_{UV}}$ ($M_\odot \mathrm{yr}^{-1}$)	$\mathrm{SFR_{H\alpha}}$ ($M_\odot \mathrm{yr}^{-1}$)	$\mathrm{SFR_{IR}}$ ($M_\odot \mathrm{yr}^{-1}$)	$A(\mathrm{H}\alpha)$	r_{50} (kpc)	$\mathrm{SFR_{IR}}/A$ ($M_\odot\,\mathrm{yr}^{-1}\,\mathrm{kpc}^{-2}$)	$M_\star$ ($\log M_\odot$)
J0910	128	35	125 ± 11	1.24	0.22	394	10.44
J1432	209	19	134 ± 10	0.75	0.17	705	10.54
J1242	100	21	55 ± 10	0.96	0.50	34	10.38

deviates from the former at short wavelengths ($\lambda < 1250$ Å). We briefly describe the effect of adopting the Reddy reddening law in Section 2.4 below.

2.3.4 Measured Ancillary Parameters

In this section we list important ancillary parameters, and describe how they are determined. The values are all listed in Table 2.2.

We measure the SFRs in three ways. In all cases we use the same IMF as that used in our SB99 fit (see above). $\mathrm{SFR_{UV}}$ is inferred from COS UV data by taking a ratio between a dereddened galaxy flux spectrum and an SB99 spectrum generated assuming an SFR of 1 $M_\odot \mathrm{yr}^{-1}$. $\mathrm{SFR_{IR}}$ is calculated by using the WISE IR data at 12 and 22 μm (Wright et al., 2010) to estimate the rest-frame 24 μm luminosity, and then using the relation given in Kennicutt and Evans (2012). This has the advantage of being independent of any uncertain correction to the UV fluxes. $\mathrm{SFR_{H\alpha}}$ is calculated from extinction-corrected fluxes. The MPA-JHU catalog provides the fluxes of Hα and Hβ. We calculate $E(\beta-\alpha)$, defined as $E(\beta-\alpha) = A(\mathrm{H}\alpha) - A(\mathrm{H}\beta)$ with A being

the extinction in magnitude, as

$$\begin{aligned} E(\beta-\alpha) &= 2.5\log[F(\mathrm{H}\alpha)_{\mathrm{obs}}/F(\mathrm{H}\beta)_{\mathrm{obs}}] \\ &\quad -2.5\log[F(\mathrm{H}\alpha)/F(\mathrm{H}\beta)] \end{aligned} \tag{2.2a}$$

Assuming a temperature of 10^4 K, which translates to an intrinsic ratio of $F(\mathrm{H}\alpha)/F(\mathrm{H}\beta) = 2.86$, the extinction in magnitude for Hα is then

$$A(\mathrm{H}\alpha) = 2.29\,E(\beta-\alpha) \tag{2.2b}$$

And so finally we have the extinction-corrected Hα flux as

$$F(\mathrm{H}\alpha)_{\mathrm{corr}} = 10^{0.4A(\mathrm{H}\alpha)}\,F(\mathrm{H}\alpha)_{\mathrm{obs}} \tag{2.2c}$$

Following Table 1.1 in Calzetti (2011), we estimate $\mathrm{SFR}_{\mathrm{H}\alpha}$ in units of $M_\odot \mathrm{yr}^{-1}$ via

$$\mathrm{SFR}_{\mathrm{H}\alpha} = 5.5\times10^{-42}\,L(\mathrm{H}\alpha) \tag{2.3}$$

where L is the luminosity in erg s^{-1}.

After examining the COS near-UV acquisition images as shown in Figure 2.5, we find that all targets are well located inside the SDSS and COS apertures, which are taken to be 1.5″ and 1.2″ respectively. We therefore do not apply any aperture corrections to SFRs. We also note that the fluxes in the images are consistent with the GALEX near-UV flux.

Additionally we use the COS near-UV images to compute the half-light radius for a given galaxy by finding an ellipse that encloses half of the total near-UV emitted

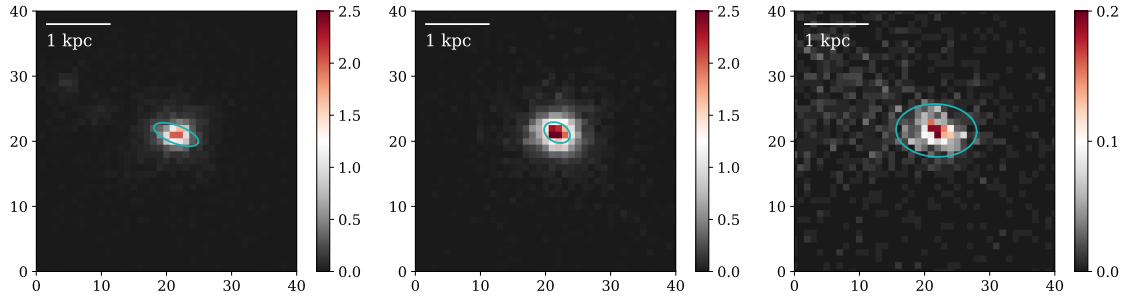

(a) (b) (c)

Figure 2.5: COS near-UV acquisition images of the three [S II]-weak star-forming galaxies: (a) J0910; (b) J1432; and (c) J1242. Also over-plotted in turquoise are the ellipses that enclose half of the total near-UV emitted light. The images are 1.032″ by 1.032″, and the color bars indicate counts per second.

light. The listed value for r_{50} is the semimajor axis of the ellipse in kpc. During the process, the background is estimated from the mean of an annulus of $r_{\rm in}$=0.9″ and $r_{\rm out}$=1.1″. A small correction for the effect of the point-spread function is also applied.

The values for the rest-frame equivalent width (EW) of the Hα emission line are taken from the MPA-JHU catalog, and the stellar masses are taken from the median of the corresponding probability density function in the same catalog.

The oxygen abundance of the interstellar medium (ISM) in each galaxy is estimated following Pettini and Pagel (2004):

$$12 + \log({\rm O/H}) = 8.73 - 0.32 \times {\rm O3N2} \tag{2.4a}$$

where

$${\rm O3N2} = \log \frac{[{\rm O\,III}]\lambda 5007/{\rm H}\beta}{[{\rm N\,II}]\lambda 6584/{\rm H}\alpha} \tag{2.4b}$$

This relation is valid for -1 <O3N2< 1.9. Since the wavelength of Hα is close to [N II] and Hβ is close to [O III], this method is insensitive to dust extinction. Then we use the conversion: $12 + \log(\mathrm{O/H}) = 8.7$ corresponding to solar metallicity.

To characterize the Lyα line, we use the following procedure. Each observed galaxy spectrum is first normalized by fitting a second-order polynomial function to the continuum and the spectrum is divided by this function. We do the same for the corresponding best-fit SB99 spectrum, which is then subtracted from the normalized galaxy spectrum to remove the stellar spectral component. Lastly we add a value of 1 to this difference spectrum to produce a normalized spectrum with stellar features removed.

To measure the Lyα EWs, we fit a (multi-component) Gaussian. We estimate that the resulting EWs have errors on the order of 10%–15% dominated by systematics in the polynomial fit to the continuum emission and the subtraction of SB99 models.

Next, we use the starlight-subtracted spectra to quantify the different Lyα profile shapes using the parameter $R_{\mathrm{Ly}\alpha}$, which is defined to be the ratio of the EW of the blueshifted portion of the profiles to that of the redshifted portion. We define the EW for emission to be positive, and for absorption to be negative. Therefore, a negative $R_{\mathrm{Ly}\alpha}$ indicates blueshifted absorption and redshifted emission (i.e. a traditional P-Cygni profile) while a positive value for $R_{\mathrm{Ly}\alpha}$ indicates significant blueshifted emission.

2.4 Results

As can be seen in Figure 2.2, we detect a significant flux below the Lyman edge in J0910 and J1432, and measure only an upper limit in J1242. To characterize this

Table 2.3: Observed Flux Densities Used in Quantifying the Escape Fractions

	LyC range[a]	F_{900}[b]	F_{900}[c]	$\frac{F_{900}}{F_{1500}}$[c]	$\left(\frac{F_{900-}}{F_{900+}}\right)_{\rm obs}$[d]	$\left(\frac{F_{900-}}{F_{900+}}\right)_{\rm obs}$[e]
J0910	885 – 910	$1.38 \pm 0.17 \pm 0.05$	2.16	0.38	0.538	0.482
J1432	888 – 910	$2.52 \pm 0.19 \pm 0.08$	2.99	0.32	0.460	0.406
J1242	885 – 910	$0.10 \pm 0.16 \pm 0.08$	1.04	0.02	0.046	0.039

Notes. The LyC ranges are wavelength ranges over which an average is taken in calculating F_{900} and F_{900^-}. The first uncertainties in F_{900} are estimated from Poisson statistics, and the second ones are from dark fluctuations.

[a] In Å.

[b] $\times 10^{-16}$ $\mathrm{s^{-1}\,cm^{-2}\,Hz^{-1}\,sr^{-1}}$; uncorrected for extinction.

[c] $\times 10^{-16}$ $\mathrm{s^{-1}\,cm^{-2}\,Hz^{-1}\,sr^{-1}}$; corrected for MW extinction only.

[d] Corrected for MW and internal extinctions, assuming extragalactic reddenning law in Calzetti et al. (1999).

[e] Same as c, but assuming extragalactic reddenning law in Reddy et al. (2015, 2016).

emission, we take the mean of flux densities, uncorrected for extinction, in a spectral window from $\sim$ 885 to 910 Å. The resulting values are listed in Table 4.4 as F_{900}. The exact spectral windows for each of the galaxies are also listed in Table 4.4 under the column LyC range. These particular choices are motivated by avoiding the detector edge where dark count rates increase significantly. The errors quoted account for both the statistical (Poisson) errors, which are extracted from the corresponding `x1d` files, and the systematic errors associated with dark subtraction.

In the following paragraphs, we consider three ways to measure the escape fraction, each with advantages and disadvantages. Relevant measurements of flux densities are all listed in Table 4.4. The first and also the simplest way is to measure the ratio of the observed fluxes in the LyC to those at a rest wavelength of 1500 Å. This measurement is made after correcting the fluxes for MW extinction only. The advantage of this parameter is that it is most directly connected to actual observational estimation of the

rate of escaping ionizing radiation during the EoR. That is, the observed luminosity density due to star-forming galaxies at a rest-frame 1500 Å can be measured from the far-UV luminosity functions during the EoR. Knowing the mean ratio of LyC to 1500 Å fluxes for a representative ensemble of star-forming galaxies (from observations of lower-z analogs) yields an estimate of the LyC luminosity density produced by the EoR galaxies. This quantity, F_{900}/F_{1500}, for the three [S II]-weak star-forming galaxies are listed in Table 4.4. For F_{1500} we fit a simple low-order polynomial to the continuum between the 1100 and 1500 Å rest frame and use the resulting value at 1500 Å since the data are noisy at this wavelength.

Next, we calculate what is sometimes referred to as the relative escape faction, $f_{\rm esc,rel}$. This is essentially the ratio of the observed flux decrement across the Lyman break (after correction for MW and internal extinctions) compared to the intrinsic decrement in the best-fit SB99 model spectrum. As such, the value of the relative escape fraction is independent of the effects of dust extinction, and is probing only radiative transfer effects associated with the photoelectric absorption of the LyC due to hydrogen.

In our specific case we define $f_{\rm esc,rel}$ as

$$f_{\rm esc,rel} = \left(\frac{F_{910^-}}{F_{910^+}}\right)_{\rm obs} \left(\frac{F_{910^+}}{F_{910^-}}\right)_{\rm int} \tag{2.5}$$

where F_{910^-} is the average extinction-corrected flux densities taken between rest frame $\sim$ 885 and 910 Å (again, the exact spectral windows are listed in Table 4.4), and F_{910^+} is the average taken between 1050 and 1150 Å. The latter choice is made to avoid the effects of the Lyα airglow line and the confluence of the high-order Lyman series

lines near the Lyman edge.

Finally, we note that dust can be a significant source of opacity for both ionizing and non-ionizing far-UV radiation in galaxies. We therefore measure what is commonly referred to as the absolute escape fraction, $f_{\rm esc,abs}$ (the ratio of emergent LyC flux to the intrinsic flux, including the effect of dust extinction). Conventionally this is calculated as

$$f_{\rm esc,abs} = f_{\rm esc,rel} 10^{-0.4 A_{910}} \tag{2.6a}$$

where

$$A_{910} = \kappa(910\text{Å}) E(\text{B}-\text{V})_{\rm int} \tag{2.6b}$$

is the absorption at 910 Å. We obtain $\kappa(910\text{Å})$ by extrapolating the fitting formulae provided in Calzetti et al. (1999); Reddy et al. (2015, 2016) slightly toward short wavelength, since the original formulae end at 1200 and 915 Å, respectively.

A major source of systematic uncertainty in Equation 2.6 is in the UV extinction. To assess this we compare the values for the escape fractions based on the extinction laws adopted by Calzetti et al. (1999) and Reddy et al. (2015, 2016) (see Table 2.4). There we see that the effects are modest but noticeable; hence we adopt a second approach to circumvent this uncertainty. We use $\text{SFR}_{\rm IR}$ to predict the LyC flux in the best-fit SB99 model, and then compare this to the observed LyC flux corrected only for the MW extinction. This quantity is listed in the last column in Table 2.4.

In addition, there are systematic uncertainties in escape fraction associated with the intrinsic Lyman break in the SB99 models. Therefore we compare the values for both solar and 1/7 solar metallicity models, for burst ages of 10^7 and 10^8 yr, and for models with and without stellar rotation employed (i.e. `Geneva v40` and `Geneva v00`,

Table 2.4: Relative and Absolute Escape Fractions

	$E(\mathrm{B-V})_{\mathrm{int}}$ [a]	$f_{\mathrm{esc,rel}}$ ($\times 10^{-2}$)	$f_{\mathrm{esc,abs}}$ ($\times 10^{-2}$)	
J0910	0.239	$93.3^{+10.2+3.2}_{-10.0-3.1}$	$3.3 \pm 0.4 \pm 0.1$	
J1432	0.243	$79.8^{+5.6+2.3}_{-5.5-2.3}$	$2.7 \pm 0.2 \pm 0.1$	
J1242	0.314	< 28.3	< 0.4	
	$E(\mathrm{B-V})_{\mathrm{int}}$ [b]	$f_{\mathrm{esc,rel}}$ ($\times 10^{-2}$)	$f_{\mathrm{esc,abs}}$ ($\times 10^{-2}$)	$f_{\mathrm{esc,abs}}$ [c] ($\times 10^{-2}$)
J0910	0.257	$83.6^{+9.1+2.8}_{-8.9-2.8}$	$4.0 \pm 0.4 \pm 0.1$	$3.5 \pm 0.5 \pm 0.3$
J1432	0.252	$70.4^{+6.6+2.1}_{-6.2-2.1}$	$3.5 \pm 0.3 \pm 0.1$	$4.1 \pm 0.4 \pm 0.3$
J1242	0.325	< 24.4	< 0.5	< 0.7

Notes. The measurements quoted for J1242 are upper limits inferred from a $3\,\sigma$ limit on dark fluxes. The first uncertainties are estimated from Poisson statistics, and the second ones are from dark fluctuations.

[a] Assuming reddenning law in Calzetti et al. (1999).

[b] Assuming reddenning law in Reddy et al. (2015, 2016).

[c] Obtained by taking the ratio between MW extinction-corrected $(F_{900})_{\mathrm{obs}}$ and $(F_{900})_{\mathrm{int}}$ inferred from SB99 given $\mathrm{SFR}_{\mathrm{IR}}$.

respectively). For completeness, we list the Lyman-break amplitudes defined as the ratio between the average flux density over 1050-1150 Å and that over 900-910 Å for different SB99 models in Table 2.5. The largest variation is with burst duration. The values we quote for the relative and absolute escape fractions for J0910 and J1432 are obtained from SB99 models with a constant SFR for 10^7 yr, while for J1242, they are from SB99 models with a constant SFR for 10^8 yr. Those spectra better fit the O VI and N V wind lines. Taking an older burst age for the former two would increase the escape fractions by ~ 0.2 dex (pushing the relative escape fractions above 1).

Table 2.5: Lyman-break Amplitudes, $F_{(1050-1150\AA)}/F_{(900-910\AA)}$, for Different SB99 Models

	$Z_\odot$, no rotation	$Z_\odot$, rotation	$Z_{1/7\odot}$, no rotation	$Z_{1/7\odot}$, rotation
J0910 (10^7 yr)	2.084	1.736*	1.792	1.756
J0910 (10^8 yr)	3.268	2.925	2.682	2.830
J1432 (10^7 yr)	2.083	1.735*	1.792	1.756
J1432 (10^8 yr)	3.268	2.923	2.684	2.830
J1242 (10^7 yr)	2.084	1.736	1.792	1.756
J1242 (10^8 yr)	3.268	2.924*	2.683	2.829

Note. The values used in calculating $f_{\rm esc}$ are indicated with asterisks.

2.5 Discussion

In this section we will place the leaky [S II]-weak galaxies in context. First, we will compare their properties to those of the leaky Green Pea galaxies, which comprise a large majority of the confirmed low-z leaky galaxies. We will then compare the properties of all the known low-z leaky galaxies to non-leaky low-z starburst galaxies. This will allow us to assess the robustness of the various proposed indirect signposts of leaky galaxies. Finally, we will compare the properties of the [S II]-weak leaky galaxies to leaky galaxies at $z \sim 3$ to 4.

2.5.1 Comparisons of [S II]-weak and Green Pea Leaky Galaxies

For the Green Pea galaxies, $M_\star$ [O III]/[O II], $\mathrm{EW}_{\mathrm{H}\alpha}$ are taken from the respective references, while the remaining quantities are calculated the same way as presented in Section 2.3.4 for consistency. Specifically, for $\mathrm{SFR}_{\mathrm{H}\alpha}$ we estimate the luminosity of Hα to be used in Equation 2.3 as $2.86L_{\mathrm{H}\beta}$, where $L_{\mathrm{H}\beta}$ is taken from the references;

for the SFR_{UV}, we retrieve their COS spectra from MAST, and deredden them using the reddening law of Calzetti et al. (1999). Since the Green Peas are nearly dust-free, this calculation of SFR_{UV} is subject to less systematic uncertainty due to internal extinction correction.

As seen in Figure 4.5, one major difference between the [S II]-weak and Green Pea samples is the stellar mass: the median masses are $10^{8.8}$ and $10^{10.4}\,M_{\odot}$ for the Green Peas and [S II]-weak galaxies respectively. This large difference in mass leads to a difference in gas-phase metallicity: median values of $12 + \log(\mathrm{O/H})$ of 8.6 and 7.9 for the [S II]-weak and Green Pea samples, where a value of 8.7 corresponds to solar metallicity.

The [S II]-weak galaxies have extraordinarily high values of SFR/area (mean of 550 $M_{\odot}\mathrm{yr}^{-1}\mathrm{kpc}^{-2}$), compared to a median value of about 75 $M_{\odot}\mathrm{yr}^{-1}\mathrm{kpc}^{-2}$ for the Green Peas. In terms of $\mathrm{SFR}/M_{\star}$, the Green Peas are more extreme (median value $10^{-7}\,\mathrm{yr}^{-1}$, about an order of magnitude larger than the values for the [S II]-weak galaxies. This is consistent with the significantly lower values of the Hα EWs in the [S II]-weak galaxies compared to the Green Peas, and together these two results suggest that the current bursts in the [S II]-weak galaxies are occurring in the presence of more significant prior star-formation on timescales longer than a few Myr compared to the Green Peas.

Other emission-line properties of the [S II]-weak galaxies are also much less extreme that those of the Green Peas. As with Hα, the Lyα EWs of the [S II]-weak galaxies are smaller than those of the Green Peas by a factor of ~ 3 (23 versus 75 Å). Moreover, as seen in Figure 2.7, the [S II]-weak galaxies do not exhibit the extraordinarily high ionization level that is characteristic of the Green Peas (with median [O III]/[O II]

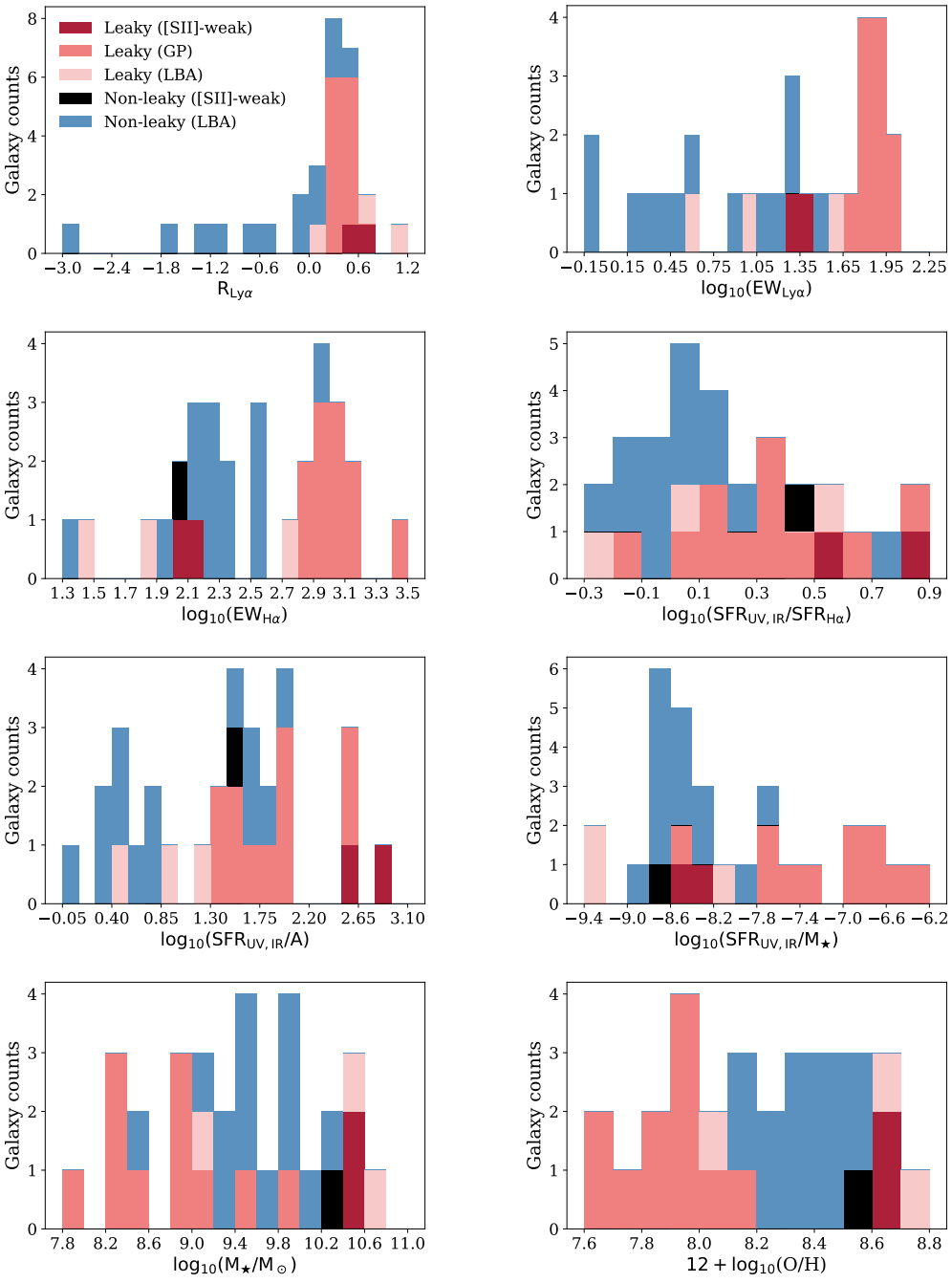

Figure 2.6: Histograms of various characteristics of the low-z galaxy samples considered in this paper. Measurements of the three [S II]-weak galaxies are tabulated in Table 2.2. We also provide those of the Green Peas and of the Lyman break analogs in the Appendix.

fluxes ratios of 1.4 versus 8.0 respectively).

In summary, the [S II]-weak galaxies differ significantly in many of their key properties from the Green Peas: they are more massive and more metal-rich, are less-dominated by stars formed in the last few Myr, have a considerably lower ionization state, and have lower absolute LyC escape fractions.

2.5.2 Signposts of Leakiness

There are a number of galaxy characteristics that have been previously identified as potential signposts of LyC leakage from galaxies. In this section we evaluate these signposts in light of our discovery of this new class of leaky galaxy. To do so, we assemble a sample of known leaky galaxies at low-z and compare their properties to a control sample of strong starbursts at similar redshifts that are unlikely to be leaky. For the sake of consistency, we include only galaxies with COS data and with the set of galaxy parameters that can be measured using the spectra in the SDSS.

These samples are drawn from the union of the [S II]-weak galaxies presented in this paper, the leaky Green Peas in Izotov et al. (2016a,b, 2018a,b), and the Lyman break analogs in Alexandroff et al. (2015). In the last sample, J0921 has been directly detected below the Lyman edge (Borthakur et al., 2014). For the other sample members, we use the residual intensity in the Lyβ absorption line as an indicator of leakiness, following the results in Chisholm et al. (2018), and see also Steidel et al. (2018). This adds J0213 and J0926 as leakers, with the 13 other galaxies in Table 2.8 being classified as non-leaky. Alexandroff et al. (2015) list all the relevant quantities, except for [O III]/[O II], which we calculate using fluxes obtained from the MPA-JHU catalog. We note that our definition for [S II]-deficit differs from that in Alexandroff

et al. (2015) by taking the horizontal displacement from the parametric ridge line as shown in Figure 2.1 instead of the perpendicular distance between each galaxy and the ridge line, so measurements of Δ[S II] are also remade according to our definition.

We have already compared some of the proposed signposts in the [S II]-weak and Green Pea galaxies in the previous section. In Figure 4.5, we see that the class of leaky galaxies as a whole has somewhat larger values for SFR/area than the non-leaky starbursts (median values of 51 versus 6 $M_{\odot}\mathrm{yr}^{-1}\mathrm{kpc}^{-2}$). The leaky galaxies are more extraordinary in this regard when compared to typical low-z star-forming galaxies, which have an SFR/area of only $\sim 10^{-2}\, M_{\odot}\mathrm{yr}^{-1}\mathrm{kpc}^{-2}$ (Kennicutt and Evans, 2012). We also see that the leaky galaxy sample has a significantly higher median value for the Lyα EW than the non-leaky galaxies (65 and 4 Å respectively).

Another common property of the leaky galaxies is that they have a significant amount of blue-shifted Lyα emission (with median value for the $R_{\mathrm{Ly}\alpha}$ parameter of 0.4 for leaky sample versus 0.0 for the non-leaky sample. Recently the Lyα profiles and their implication for the escape of LyC in Green Peas is discussed in Jaskot et al. (2019). There is also a trend for the leaky galaxies to have significantly higher SFRs based on the IR luminosity or the extinction-corrected far-UV luminosity than those based on the extinction-corrected Hα emission-line luminosity, and larger than the values in the non-leaky galaxies (median ratios of 2.3 versus 1.1; also see Figure 10 in Overzier et al. 2009).

Interestingly, although the leaky Green Peas exhibit a range of Δ[S II] and were not selected based on [S II]-weakness, they all have Δ[S II] < 0. In fact, the five galaxies with the largest [S II] deficiency observed so far in the Lyman continuum (three Green Peas and our two targets) are all leaky (see Figure 2.7).

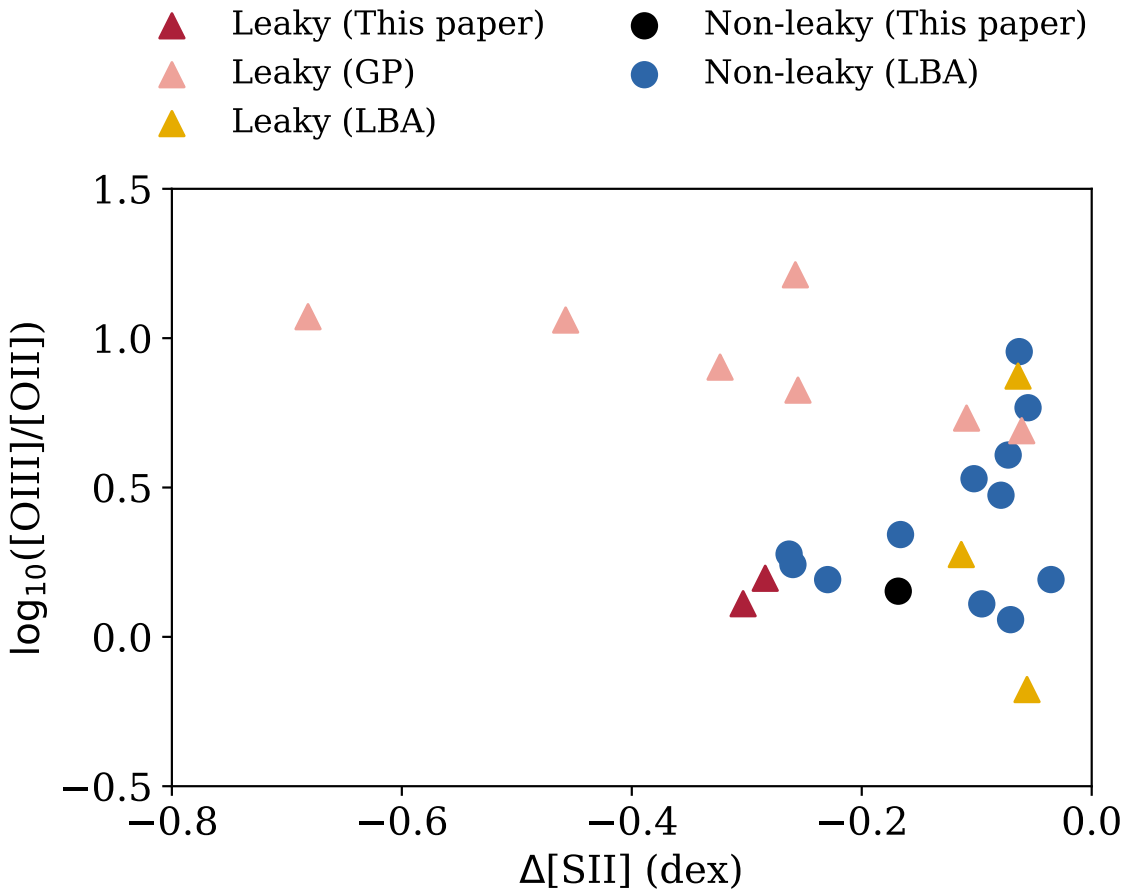

Figure 2.7: Flux ratio of [O III] 5007/[O II] 3727 versus [S II] deficiency for the union of galaxy samples considered in this paper. The two leaky [S II]-weak galaxies are shown as red triangles, while the other non-leaky [S II]-weak galaxy is shown as a black dot. We see that the [S II]-weak leakers do not exhibit the extraordinarily high ionization level that is characteristic of the Green Peas (pink triangles). The remaining galaxies are drawn from Lyman break analogs.

Thus far, we have opted not to discuss in depth any statistical significance which may be manifested in Figure 4.5 due to the still small sample of confirmed leaky galaxies. Rather, we think it is more suitable at present time to describe qualitative trends among the signposts for leakiness to guide future studies. In light of this, we conclude that the following signposts appear to be robust (i.e. properties that are in common among the different classes of low-z leaky galaxies): a high SFR/area, lower values for the SFR measured from Hα luminosity than from the far-UV plus IR continuum luminosity, strong Lyα emission with a significant fraction that is blue-shifted, and abnormally weak [S II] emission.

All these signposts have physically plausible connections to the escape of LyC radiation. We have already discussed why [S II]-weakness could be connected to LyC leakage. A high SFR/area leads directly to a high intensity (flux/area) of ionizing radiation, which can lead to an ISM that is optically thin to the LyC. It also leads to large values for radiation pressure and the ram-pressure of a starburst-driven wind (e.g., Heckman et al. 2015). The outward forces these generate can act to expel the ISM and create channels for the escape of ionizing radiation. As ionizing radiation escapes the ISM, the rate of Hα emission produced by recombination will decrease. A large Lyα EW implies clear channels through which photons resonantly scattered off H I atoms can escape, and the blue-shifted emission suggests that we are seeing Lyα photons scattered off the near side of an outflowing wind (e.g., Borthakur et al. 2014).

Finally, it is important to emphasize that these signposts are based on global/isotropic galaxy properties (i.e. properties that should depend only weakly on the observer's particular line of sight to the galaxy). This would imply that leakage occurs in a

rather isotropic way, instead of just along certain lines of sight.

2.5.3 The Role of Dominant Central Objects

We have discussed the evidence above for a general connection between a high SFR/area and the escape of LyC radiation. Here we return to the suggestion in Heckman et al. (2011) and Borthakur et al. (2014) that this escape is made possible by the extreme feedback effects produced by a "dominant central object" (DCO). These DCOs were discovered to be present in 20% of a sample of Lyman break analog low-z galaxies imaged with the HST (Overzier et al., 2009). They are defined to be compact (marginally resolved by HST), very massive, young objects located at or near the galactic nucleus, and much brighter in the UV than any other star-forming cluster or clump in the galaxy. Heckman et al. (2011) noted that three of the four candidate leaky galaxies in the sample which they analyzed contained a DCO.

As seen in Figure 2.5, DCOs are present in both of the two leaky [S II]-weak galaxies, and produce nearly all the UV emission. In the third (non-leaky) galaxy there is a significant fraction of diffuse UV emission. While we do not have robust estimates of the masses of just the DCOs themselves, we can obtain rough values based on the SB99 models for the far-UV spectra since DCOs dominate the far-UV light. The estimated SFRs of 125 and 134 $M_{\odot}\mathrm{yr}^{-1}$, and ages of 10^7 yr imply that $M_{\star,\mathrm{DCO}} > 10^9\,M_{\odot}$). These masses are similar to the values derived from multi-band spectral energy density fits to the six DCOs in Overzier et al. (2009). The measured radii are ~ 300 pc versus a mean value of 150 pc for the DCOs in the aforementioned reference. Overzier et al. (2009) showed that the properties of the DCOs are consistent with their being the progenitors of the central "extra light" component found in the

centers of cuspy elliptical galaxies, which would have formed during a strong starburst in a dissipative galaxy merger.

2.5.4 Comparisons at Higher Redshift

Before proceeding to further comparisons, we would like to address the validity of our selection criterion when it is extended to higher redshifts. Strom et al. (2018) reported spectral measurements from the Keck Baryonic Structure Survey (KBSS) of about 150 star-forming galaxies at $z \sim 2$ to 3. Those galaxies fill the upper left region in Figure 2.1 which is sparsely sampled in the SDSS (low [S II]/Hα but high [O III]/Hβ). We find that the ridge line in our Figure 2.1 passes right through the center of the data points in Figure 6 of Strom et al. (2018): see Figure 2.8. This shows that the method presented in this paper can be straightforwardly applied to higher redshifts, even though we drew our reference for defining the [S II] deficiency based on the SDSS. It also shows that a minority population of [S II]-weak galaxies are present at these higher redshifts.

We now compare the properties of the [S II]-weak leaky galaxies to other leaky galaxies at higher redshifts. Steidel et al. (2018) (hereafter S18) reported the detection of LyC flux in 15 individual galaxies at $z \sim 3$ (out of sample of 124 galaxies), and in stacked spectra binned according to various galaxy properties. Marchi et al. (2018) have observed 401 galaxies at $z \sim 4$, and detected LyC flux in stacks of spectra binned in various ways. Vanzella et al. (2018) reported the highest redshift individually confirmed LyC-leaky galaxy at $z = 4$, and Vanzella et al. (2020) found evidence of a compact region emitting LyC radiation at $z \sim 3$.

The results on the properties of these leaky galaxies are qualitatively consistent

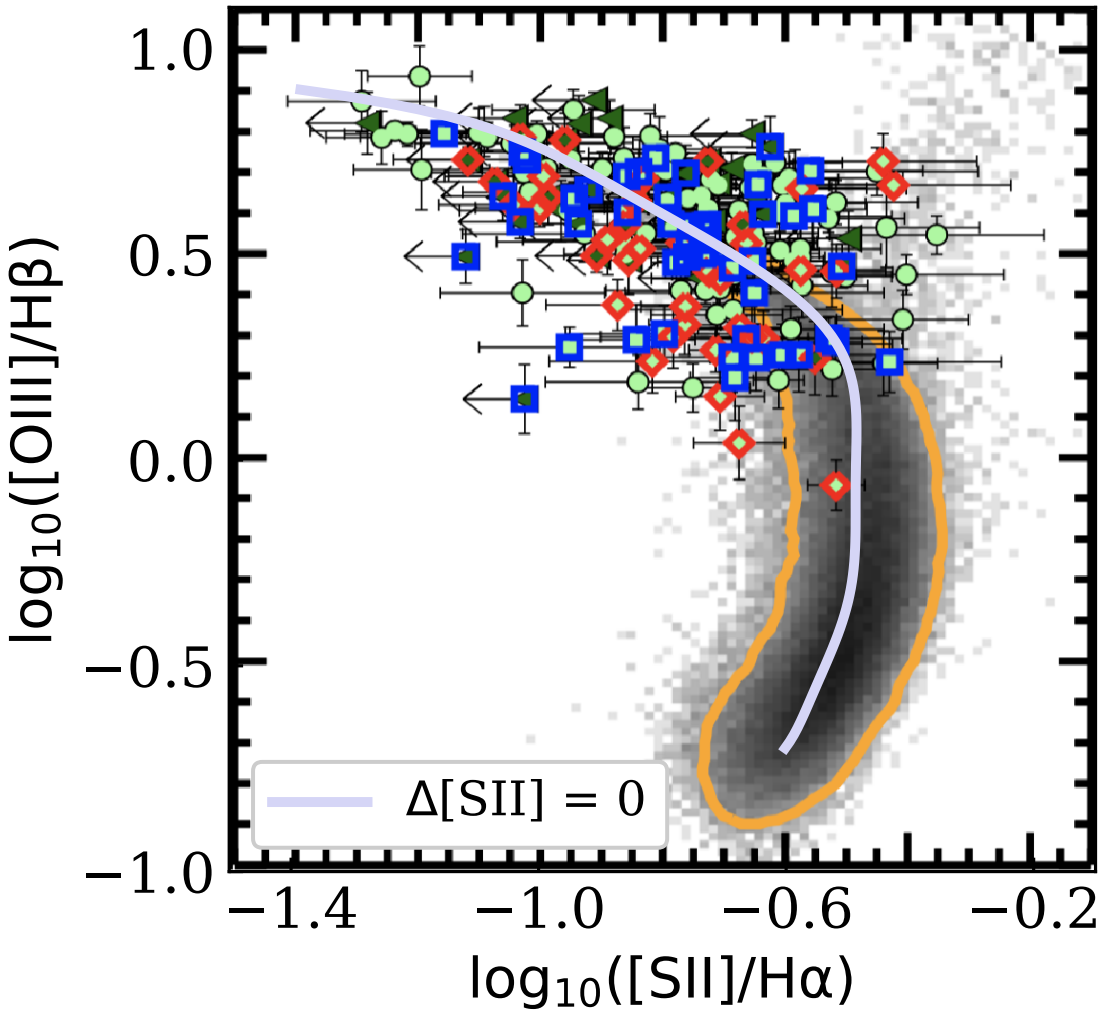

Figure 2.8: Adapted from Figure 6 of Strom et al. (2018). The light purple line is our reference line from which [S II] deficiency is quantified. The locus of $z \sim 0$ galaxies from the SDSS is shown in greyscale, with an orange contour enclosing 90% of the sample. $\langle z \rangle = 2.3$ galaxies from the Keck Baryonic Structure Survey are shown as green dots, and galaxies with $2\,\sigma$ upper limits on [S II] are shown as dark green triangles.

Table 2.6: Comparisons between the Two Leaky [S II]-weak Galaxies of This Paper, and S18

	M_{FUV} (AB mag)	log $M_\star$ $M_\odot$	$E(B-V)_{int}$ (mag)	$EW_{Ly\alpha}$ (Å)	$R_{Ly\alpha}$	SFR ($M_\odot yr^{-1}$)	SFR/$M_\star$ (Gyr^{-1})	F_{900}/F_{1500}	$f_{esc,rel}$	$f_{esc,abs}$
[S II]	-21.4	10.5	0.25	23	0.60	130	4.2	0.35	0.77	0.04
S18	-20.9	9.8	0.045	28	0.35	25	4.0	0.36	1.21	0.70

Notes. Comparisons between the mean values calculated from measurements of our two leaky [S II]-weak Galaxies, and the median of the S18 sample. For the [S II]-weak sample, we use the values based on the extinction law in Reddy et al. (2015, 2016). Unless otherwise noted, the values for the S18 sample are taken directly from S18. The SFR for S18 is based on the bolometric luminosity in S18 and the prescription in Kennicutt and Evans (2012). The value for $M_\star$ assumes that these galaxies lie along the star-forming main sequence (Reddy et al., 2012). The value for $R_{Ly\alpha}$ is our estimate based on the published stacked spectrum in S18.

with the results presented above for the low-z leaky galaxies: a higher escape fraction is associated with compact sizes (radii < 300 pc) and with strong Lyα emission. Since S18 tabulate the median properties of their individual detections, we directly compare these values to those of our two leaky [S II]-weak galaxies. This is presented in Table 2.6.

In many respects, the galaxies in the two samples are similar, including the properties of the Lyα emission line, the specific SFR, F_{900}/F_{1500}, and $f_{esc,rel}$. The [S II]-weak galaxies are somewhat more massive, and have higher SFRs. The biggest difference is in the larger amount of dust extinction in the [S II]-weak galaxies, which leads to smaller absolute escape fractions. This may reflect higher ($\sim$ solar) ISM metal abundances (higher dust-to-gas ratio) in the [S II]-weak galaxies.

2.6 Conclusions

We have reported on observations with COS on HST of three low-z ($z \sim 0.3$) starburst galaxies, selected on the basis of the relative weakness of the [S II] 6717,6731 nebular emission lines defined with respect to normal star-forming galaxies. This is a proposed signpost for galaxies that are optically thin to ionizing radiation. We detect a significant flux below the Lyman limit in two of the three galaxies, with relative escape fractions of 93% and 80% respectively and absolute escape fractions of 3% and 4%.

We have compared these [S II]-weak galaxies to other known classes of "leaky" galaxies. Compared to the low-z Green Peas, the [S II]-weak leaky galaxies have significantly larger stellar masses, higher metallicities, larger amounts of dust extinction, a much lower ionization state (as traced by the nebular emission lines), smaller Lyα emission line EWs, and have optical spectra that are less dominated by a very young (few Myr old) starburst.

We have compared the properties of the entire known set of low-z leaky galaxies to non-leaky starbursts at similar redshifts. We find that the leaky galaxies have higher SFR per unit area, stronger Lyα emission lines, and a greater fraction of the Lyα emission produced by blue-shifted material. Interestingly, we find that while the Green Peas were not selected based on [S II] properties, they too have relatively weak [S II] emission lines. We also find that leaky galaxies have significantly lower SFRs based on Balmer emission-line luminosity than those based on the intrinsic far-UV plus IR continuum luminosity (as required if a large fraction of ionizing photons escape).

We have also compared the [S II]-weak galaxies to samples of leaky galaxies at $z \sim$ 3 to 4. We find overall similarities, including compact sizes and relatively strong Lyα emission. Compared to the sample of galaxies at $z \sim 3$ that are individually detected in the LyC, the [S II]-weak galaxies differ most strongly in having larger amounts of dust extinction, which results in significantly smaller values for the absolute escape fraction (even though the relative escape fractions are similar). This may reflect a higher ($\sim$ solar) ISM metallicity and a correspondingly higher dust/gas ratio in the [S II]-weak galaxies. We have also shown that our technique for selecting [S II]-weak galaxies can be applied out to redshifts $\sim$ 2 to 3, based on existing spectra.

We thus conclude that [S II]-weakness is a highly effective way to identify galaxies that are likely to be leaking a significant amount of LyC radiation. Since the leaky galaxies described in this paper are so different from Green Peas, this technique potentially expands the range of galaxy properties over which such searches for leaky galaxies can be done. This will improve our opportunities to use low-z leaky galaxies as local laboratories in which the physical processes and characteristics that allow LyC photons to escape can be investigated. It also suggests that there may be a variety of different physical conditions and processes that make galaxies leaky. Finally, it gives us an additional technique to identify leaky galaxies during the EoR using spectroscopic observations with the JWST.

B.W. thanks Sihao Cheng and Hsiang-Chih Hwang for valuable conversations, Kate Rowlands for assistances on SDSS data sets, and Weichen Wang for clarifications on dust extinction. This work is supported by HST-GO-15341, provided by NASA through a grant from the Space Telescope Science Institute, which is operated by the Association of Universities for Research in Astronomy, Inc., under

NASA contract NAS5-26555. R.A.O. is grateful for financial support from FAPESP grant 2018/02444-7. This publication made use of data products from the Wide-field Infrared Survey Explorer, which is a joint project of the University of California, Los Angeles, and the Jet Propulsion Laboratory/California Institute of Technology, funded by the National Aeronautics and Space Administration; the NASA/IPAC Extragalactic Database, which is operated by the Jet Propulsion Laboratory, California Institute of Technology, under contract with the National Aeronautics and Space Administration; and the NASA Astrophysical Data System for bibliographic information.

Appendix

All numerical values used in producing the histograms are given in Tables 2.7 and 2.8.

Table 2.7: Measurements of Green Pea galaxies in Izotov et al. (2016a,b, 2018a,b)

	$M_\star$ ($\log M_\odot$)	r_{50} (kpc)	$\frac{\mathrm{SFR_{UV}}}{\mathrm{SFR_{H\alpha}}}$	$\mathrm{SFR_{UV}}/A$ ($M_\odot \mathrm{yr}^{-1}\mathrm{kpc}^{-2}$)	$\mathrm{SFR_{UV}}/M_\star$ ($\log \mathrm{yr}^{-1}$)	$\mathrm{EW_{Ly\alpha}}$ (Å)	$R_{\mathrm{Ly}\alpha}$	$\mathrm{EW_{H\alpha}}$ (Å)	[O III]/[O II]	Δ[S II] (dex)	12+log(O/H)
J1152	9.59	0.49	2.33	43	-7.78	54.66	0.52	1320	5.4	-0.11	8.0
J1333	8.5	0.56	6.38	32	-6.71	60.62	0.22	817	4.8	-	7.76
J1442	8.96	0.25	5.01	325	-6.86	80.55	0.24	1122	6.7	-0.26	7.93
J1503	8.22	0.29	2.0	102	-6.49	69.17	0.24	1438	4.9	-0.06	7.95
J0925	8.91	0.35	2.32	112	-6.99	68.91	0.39	732	5.0	-	7.91
J0901	9.8	0.37	1.57	24	-8.48	106.83	0.3	831	8.0	-0.32	8.16
J1011	9.0	0.13	2.63	365	-7.38	74.96	0.52	1052	27.1	-	7.99
J1243	7.8	0.24	1.99	86	-6.31	83.87	0.52	740	13.5	-	7.89
J1248	8.2	0.25	1.19	75	-6.72	107.54	0.47	2561	11.8	-0.68	7.64
J1256	8.8	0.24	1.39	29	-7.77	60.2	0.24	955	16.3	-0.26	7.87
J1154	8.2	0.18	0.68	25	-7.51	86.48	0.44	1150	11.5	-0.46	7.62

Table 2.8: Measurements of Lyman Break Analogs in Alexandroff et al. (2015)

	Type	$M_\star$	r_{50}	$\frac{\mathrm{SFR_{UV}}}{\mathrm{SFR_{H\alpha}}}$	$\mathrm{SFR_{UV}}/A$	$\mathrm{SFR_{UV}}/M_\star$	$\mathrm{EW_{Ly\alpha}}$	$R_{\mathrm{Ly\alpha}}$	$\mathrm{EW_{H\alpha}}$	[O III]/[O II]	Δ[S II]	12+log(O/H)
		($\log M_\odot$)	(kpc)		($M_\odot \mathrm{yr}^{-1}\mathrm{kpc}^{-2}$)	($\log \mathrm{yr}^{-1}$)	(Å)		(Å)		(dex)	
J0055	×	9.7	0.32	0.82	36.65	-8.33	2.32	-1.25	375	3.38	-0.1	8.28
J0150	×	10.3	1.37	1.88	3.17	-8.73	3.04	-1.72	199	2.2	-0.17	8.4
J0213	▲	10.5	0.39	3.33	19.84	-9.22	9.2	0.69	31	1.89	-0.11	8.76
J0921	▲	10.8	0.78	1.25	7.68	-9.33	4.01	1.04	72	0.67	-0.06	8.69
J0926	▲	9.1	0.69	0.59	3.47	-8.08	36.22	0.14	577	7.47	-0.06	8.05
J1025	×	9.2	0.61	0.62	3.23	-8.32	20.71	0.02	395	5.85	-0.06	8.11
J1112	×	10.2	0.33	1.16	41.9	-8.74	7.6	-0.63	205	1.75	-0.26	8.52
J1113	×	9.6	1.09	5.67	0.95	-8.75	0.85	-0.09	24	1.14	-0.07	8.35
J1144	×	9.9	0.76	1.26	2.45	-8.95	0.78	-2.89	85	1.56	-0.04	8.4
J1414	×	8.5	0.63	0.81	2.06	-7.79	1.83	0.28	351	-	-	-
J1416	×	10.0	0.19	1.17	102.94	-8.63	1.69	0.5	183	1.89	-0.26	8.47
J1428	×	9.6	0.71	0.7	4.39	-8.46	19.65	0.04	249	2.98	-0.08	8.31
J1429	×	9.4	0.29	0.74	50.72	-7.97	32.17	0.27	850	9.01	-0.06	8.12
J1521	×	9.5	0.37	0.98	6.8	-8.73	3.96	-1.07	145	4.06	-0.07	8.27
J1525	×	9.4	0.51	1.43	5.54	-8.44	16.57	-0.01	126	1.29	-0.1	8.46
J1612	×	10.0	0.31	1.12	59.87	-8.44	13.6	-0.41	174	1.55	-0.23	8.51

Notes. "▲" and "×" stand for "leaky" and "non-leaky" galaxies respectively.

Chapter 3

The Low-redshift Lyman-continuum Survey: [S II] Deficiency and the Leakage of Ionizing Radiation

3.1 Introduction

The epoch of reionization (EoR), the phase during which the universe transitions from fully neutral to ionized, remains largely unexplored observationally. At the center is the question regarding the sources responsible for the EoR. Deep imaging with the Hubble Space Telescope (HST) indicates that the ultraviolet (UV) luminosity density of early star-forming galaxies is high enough for them to be the best candidates to provide the ionizing photons necessary for reionizing the universe (e.g., Bouwens et al.

2016). Unfortunately, since the universe during the EoR is opaque to ionizing photons, direct observations that access the Lyman continuum (LyC) at these redshifts are impossible.

Identifying LyC emitters (LCEs) at low redshifts thus becomes an important step in the investigation of how galaxies could reionize the universe. Over the past decade, the community has invested in a huge effort to identify small samples of LCEs. Several proxies for LyC escape have been suggested. Strong Lyα emission is perhaps the most known one, and has been shown to correlate with LyC emission both in individual galaxies at low z (Verhamme et al., 2017) and in stacked samples at $z \sim 3$ (Marchi et al., 2018; Steidel et al., 2018). However, the absorption due to the neutral intergalactic medium limits its utility at $z \gtrsim 6$. High [O III]/[O II] flux ratios, which indicate a high ionization state, have been used to select LyC-emitting Green Pea galaxies (Izotov et al., 2016a; Jaskot et al., 2019). This class of galaxies constitutes the majority of LCEs in the literature so far. LyC predictors based on UV absorption lines and Mg II emission have also been proposed recently (Chisholm et al., 2018; Chisholm et al., 2020).

Among those efforts, Wang et al. (2019) (hereafter W19) tested a new diagnostic for LyC leakage, the relative weakness of [S II] nebular emission lines (Δ[S II]), in a pilot HST program. Significant emerging flux below the Lyman edge was detected in two out of three [S II] deficiency-selected star-forming galaxies at $z \sim 0.3$.

In this paper, we explore the connection between LyC leakage and [S II] deficiency with the expanded data set from the Low-redshift LyC Survey (LzLCS)—a large HST program aiming for a first statistical sample at $z \sim 0.3$. The full sample consists of 66 star-forming galaxies, and is described in Flury et al. (2021a).

The structure of this paper is as follows. In Section 3.2, we begin by reviewing the physical basis for the [S II] deficiency diagnostic and its definition. In Section 4.2, we summarize the galaxy samples and the relevant analyses. In Section 3.4, we assess the robustness of the [S II] deficiency test, and compare it to other proposed LyC diagnostics. In Section 4.4, we discuss the implications for the physical properties of LCEs at low- and high-z. Finally, we summarize our conclusions in Section 3.6.

3.2 [S II] Deficiency

The relative weakness of the [S II] 6717, 6731 emission lines was first proposed as a signpost to identify galaxies that likely allow the escape of LyC radiation by Alexandroff et al. (2015). This was motivated by a simple physical argument: the ionization potential for producing [S II] is only 10.4 eV, which is less than that for ionizing neutral hydrogen. Therefore much of the [S II] emission arises in the warm partially ionized region near and just beyond the outer edge of the Strömgren sphere in a classical H II region. This region is weak or even absent when the medium is optically thin to the LyC, resulting in a significant drop in the relative intensity of [S II] emission lines (Pellegrini et al., 2012).

We measure the [S II] deficiency in a differential sense: as a quantity relative to the majority of star-forming galaxies in the Sloan Digital Sky Survey (SDSS). To do this, we first use the BPT/VO [N II]/Hα *vs.* [O III] 5007/Hβ diagnostic diagram (Baldwin et al., 1981; Veilleux and Osterbrock, 1987) to exclude AGN and composite objects, based on the criteria in Kewley et al. (2006). We then use this sample of star-forming galaxies and the BPT/VO diagram of [S II] 6717, 6731/Hα *vs.* [O III] 5007/Hβ. We

follow the procedure outlined in W19 in this paper, but with the slight modification of including the star-forming galaxies in the Baryon Oscillation Spectroscopic Survey (BOSS) to improve the sampling of high-excitation galaxies. All fluxes are taken from the value added catalog provided by the Portsmouth group (Thomas et al., 2013), and a signal-to-noise (S/N) cut of five is imposed. Both emission-line ratios are dust-extinction corrected based on the observed Balmer lines. Measured values of log([S II]/Hα) are binned in log([O III]/Hβ), and the Gaussian mean (or skewed Gaussian mean when more suitable) of each bin is then calculated. We define the [S II] deficiency as a galaxy's displacement in log([S II]/Hα) from a polynomial fit to Gaussian means. The fitting formula is

$$y = -0.475 - 0.051\xi - 0.589\xi^2 - 0.360\xi^3, \tag{3.1}$$

where ξ is log([O III]/Hβ), and y is log([S II]/Hα).

We note that the uncertainty in Equation 3.1, which is estimated via bootstrap, becomes significant only at very large values of log([O III]/Hβ) > 0.8. Although the difference between the new curve and the one used in W19 or that in Ramambason et al. (2020) is well within $1\,\sigma$ even for log([O III]/Hβ) > 0.8, we have tested the result of excluding galaxies lying above this value on the subsequent analysis in the paper, and find that there are no changes to our conclusions.

One other potential issue is that while the ratio of [O III]/Hβ generally increases with decreasing O/H, it reaches its maximum value at $12 + 1\log(\mathrm{O/H}) \sim 7.9$, below which it slowly falls (Maiolino et al., 2008). For galaxies below this metallicity value, a decrease in [O III]/Hβ could potentially mimic a [S II] deficiency in Figure 3.1. To

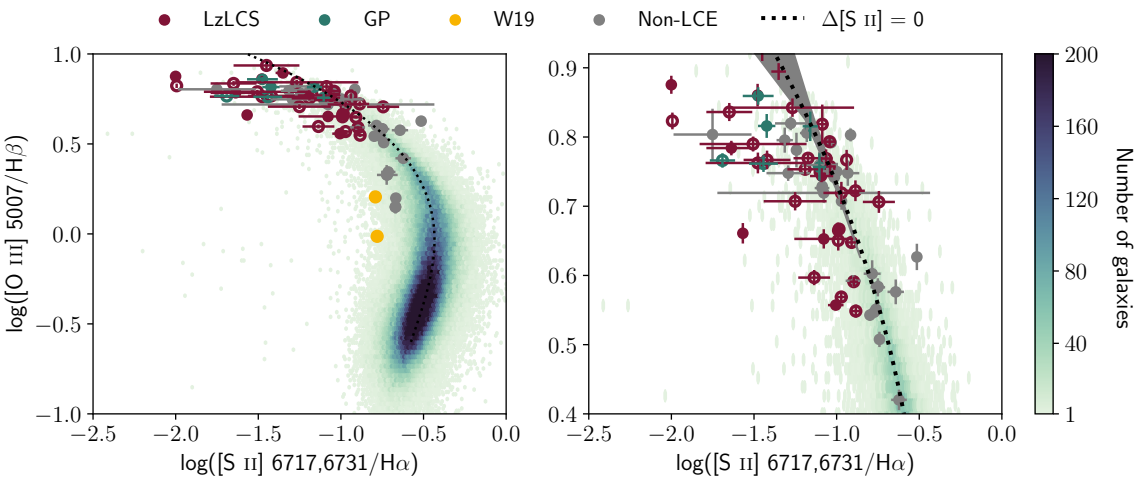

Figure 3.1: (Left) This BPT/VO diagram drawn from the SDSS DR12 + BOSS DR8 star-forming galaxy sample is used for defining Δ[S II]. The colorbar shows the number of galaxies in each hexbin. The black dotted line is fitted to the locus of the peak density of this distribution. Its uncertainty (gray shade) is negligible expect for $\log([\text{O III}]/\text{H}\beta) > 0.8$, where data becomes sparse. The [S II] deficiency is defined as a galaxy's displacement along the x-axis from this ridge line. Also plotted are the galaxy samples considered in this paper: LzLCS, Green Pea galaxies (GP; Izotov et al. 2016a,b, 2018a,b), and [S II] deficiency-selected galaxies (W19; Wang et al. 2019). (Right) A zoom-in on the upper part of the left figure. Solid colored dots represent strong LCEs, circles represent weak LCEs, and gray dots are nondetections.

check on the potential effects of this we have also tested the result of excluding the 10 sample members with $12 + \log(\text{O/H}) \leq 7.9$. We again find that there are no changes to our conclusions.

The samples of galaxies are shown as filled and unfilled circles in the Figure 3.1 and their relevant analyses are presented in Section 4.2.

3.3 Data

3.3.1 Galaxy Samples

LzLCS (HST-GO-15626; PI A. Jaskot) consists of a sample of 66 star-forming galaxies at $z \sim 0.3$, selected to meet at least one of the following three criteria: [O III]/[O II] flux ratio > 3, UV spectral slope $\beta < -2$, or $\Sigma_{\rm SFR} > 0.1\,M_{\odot}{\rm yr}^{-1}{\rm kpc}^{-2}$.

We additionally consider the following two samples from the literature. First, three star-forming galaxies were selected based on [S II] deficiency in a pilot program (HST-GO-15341; PI T. Heckman), two of which have been observed with significant LyC flux in W19. Second, 11 Green Pea galaxies (GPs) are included, which constitute the majority of confirmed low-z LCEs in the existing literature before LzLCS (Izotov et al., 2016a,b, 2018a,b).

3.3.2 Data Analysis

Processing of the Cosmic Origins Spectrograph (COS) spectra in LzLCS is presented in detail in Flury et al. (2021a). UV continuum fitting is discussed in Saldana-Lopez et al. (2021). Here we describe the additional analyses performed for the purpose of this paper.

The fluxes of [S II] emission lines in SDSS spectra of are remeasured for all sources in LzLCS. This is done out of caution as some LzLCS spectra are found to have low S/N in the [S II] lines. However, this does not imply that the fluxes of the SDSS reference sample used to draw the curve of $\Delta[{\rm S\,II}] = 0$ are subject to a similar error, since only emission lines with S/N ≥ 5 are selected.

For SDSS spectra of the LzLCS sample, we categorize them into three subgroups

based on S/N and each is subjected to a different treatment: 1) both lines of the [S II] doublet, when detected, are simultaneously fitted with Gaussians, and $1\,\sigma$ uncertainties as provided in SDSS spectra are propagated; 2) when only one of the [S II] lines is detected with significance, the undetected line is inferred from the detection; that is, its Gaussian fit is constrained by the line-center shift, amplitude (after taking the typical ratio of the doublets into account), and the full width at half maximum of the detected line; 3) when neither of the [S II] lines are available, $3\,\sigma$ upper limits are inferred from uncertainties. We list the measured flux along with [S II] deficiency in Section 4.5.

3.3.3 Escape Fractions

Given the complications in estimating escape fractions ($f_{\rm esc}$) of the LyC photons, two approaches are considered. First, the ratio between the flux of LyC and of the stellar continuum at $\sim$ 1100 Å rest frame ($f_{\rm LyC}/f_{1100}$) is used as a proxy of $f_{\rm esc}$. It has the advantage of being less model dependent. Second, it is common to estimate $f_{\rm esc}$ by comparing the observed ratio of flux density at $\sim$ 900 Å to that at $\sim$ 1500 Å (F_{900}/F_{1500}) with the intrinsic ratio (Steidel et al., 2001). After accounting for the dust attenuation, we obtain the absolute $f_{\rm esc}$, denoted as $f_{\rm esc}^{\rm UV}$(LyC) in this paper. Specifically, we derive $f_{\rm esc}^{\rm UV}$(LyC) by finding an intrinsic UV spectrum following the fitting methods of Chisholm et al. (2019) and presented in Saldana-Lopez et al. (2021). We fit the observed stellar continuum as a linear combination of multiple single-age and single-stellar-metallicity bursts. We use 50 possible theoretical Starburst99 models (Leitherer et al., 1999, 2010) that span a range of ages (1 – 40 Myr) and metallicities (0.05 – 2 $Z_{\odot}$) that are relevant to the young starbursts in the LzLCS. We assume

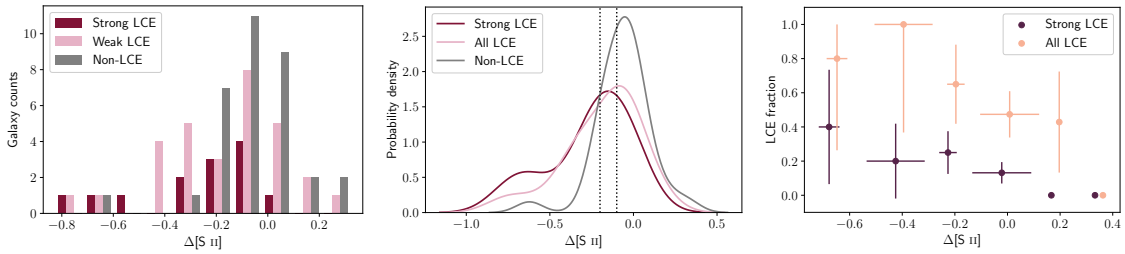

(a) (b) (c)

Figure 3.2: (a) Histograms and (b) Gaussian KDEs showing distributions of Δ[S II] among the whole sample. The two dotted lines represent Δ[S II] = -0.2 and -0.1 respectively. (c) Fractions of strong and all LCE detections in bins of Δ[S II]. Results from different samples are offset in Δ[S II] for clarity. Correlations are exhibited despite of substantial Poisson uncertainties driven by small number counts (see Table 3.1).

a standard Kroupa initial mass function (Kroupa, 2002) and use the Geneva stellar evolution tracks with high-mass-loss rates (Meynet et al., 1994). Finally, we account for dust attenuation using the Reddy et al. (2016) law, which is observationally defined down to 950 Å. We fit to the stellar continuum redward of 950 Å by masking the strong interstellar medium (ISM) absorption features and fitting the best-fit linear coefficients and dust attenuation parameter. We then extend the stellar continuum fit blueward to LyC and take the ratio of the fit to the observations to determine $f_{\rm esc}^{\rm UV}$(LyC).

3.4 Results

3.4.1 Statistical Tests of the [S II] Deficiency Diagnostic

The larger sample size of LzLCS allows for a first statistical study on the reliability of the [S II] deficiency diagnostic. Before proceeding to present the results, we would

Table 3.1: Correlations between Δ[S II] and $f_{\rm esc}$ / LCE Fractions

	Kendall's τ	p-value
$f_{\rm LyC}/f_{1100}$[a]	-0.256	0.001
$f_{\rm esc}^{\rm UV}$(LyC)[a]	-0.229	0.003
F(s)[b]	-0.828	0.022
F(all)[c]	-0.867	0.017

[a] Correlations are calculated from the whole sample (see Figure 3.5).

[b] Fractions of strong LCEs in bins of Δ[S II] (see Figure 3.2c).

[c] Fractions of all LCEs in bins of Δ[S II].

first like to reiterate definitions of LCEs in the survey (Flury et al., 2021a). The classification is determined based on two criteria: the probability ($P(>N|B)$) that the observed or gross counts within the extraction window of the LyC are due to background fluctuations (Worseck et al., 2016), and escape fraction ($f_{\rm esc}$) or its proxy $f_{\rm LyC}/f_{1100}$. First, we define LCEs as having $P(>N|B) < 0.02275$. Second, a subset of LCEs having $P(>N|B) < 2.867\times10^{-7}$ and $f_{\rm esc}$ or $f_{\rm LyC}/f_{1100} > 0.05$ are defined as "strong" detections. The rest are considered non-LCEs. We note that using different definitions of $f_{\rm esc}$ yields qualitatively similar results.

We address the robustness of the [S II] deficiency diagnostic from two perspectives. First, distributions of Δ[S II] among the different groups are compared. Figure 3.2(a)-(b) show the histograms and Gaussian kernel density estimates (KDEs) of Δ[S II], respectively. A preference for the class of LCEs to have more negative Δ[S II] than that of the non-LCEs is present.

To quantify the above, we calculate an Anderson-Darling statistic for the LCEs (and strong LCEs) of 3.0 (2.3), suggesting that the null hypothesis that the two samples come from the same distribution can be rejected at about a 98.0% (96.3%)

level.

Second, we calculate fractions of LCE detections in bins of Δ[S II], as shown in Figure 3.2(c). Significant correlations are exhibited, despite substantial Poisson uncertainties on fractions which are driven by the small number counts. We list the correlation coefficients in Table 3.1.

Taken together, those results indicate that a candidate's likelihood of being an LCE increases as [S II] deficiency becomes more prominent.

3.4.2 Comparison to Other LyC Diagnostics

A number of galaxy characteristics have been identified as potential signposts of LyC leakage (e.g., Verhamme et al. 2015; Izotov et al. 2016a; Chisholm et al. 2018; for results from LzLCS, see Flury et al. 2021b). Here we evaluate the [S II] deficiency diagnostic in context of its relationship to other signposts. We note that the velocity separation ($v_{\rm sep}$) of the two Lyα peaks and $f_{\rm esc}$ of the LyC has been shown to be tightly correlated (Izotov et al., 2018b; Izotov et al., 2021). However, LzLCS lacks the necessary observations using the low-resolution COS/G140L grating to measure $v_{\rm sep}$. We hence neglect a discussion regarding $v_{\rm sep}$ in what follows.

Figure 3.3 shows the galaxy distributions in the plane of Δ[S II] *vs.* other signposts, color coded in $f_{\rm esc}$ (see Section 3.5.2 for details on $f_{\rm esc}$). The corresponding Kendall's τ correlation coefficients and their significance (p-values) are also shown in the figures. Their uncertainties are estimated via bootstrap. Most of the correlations are rather weak. Among the strongest ones are between Δ[S II] and the half-light radii (r_{50}) measured from COS NUV ACQ images and the star formation rate per unit area ($\Sigma_{\rm SFR,H\beta}$). This is consistent with the frequent identification of LCEs as being highly

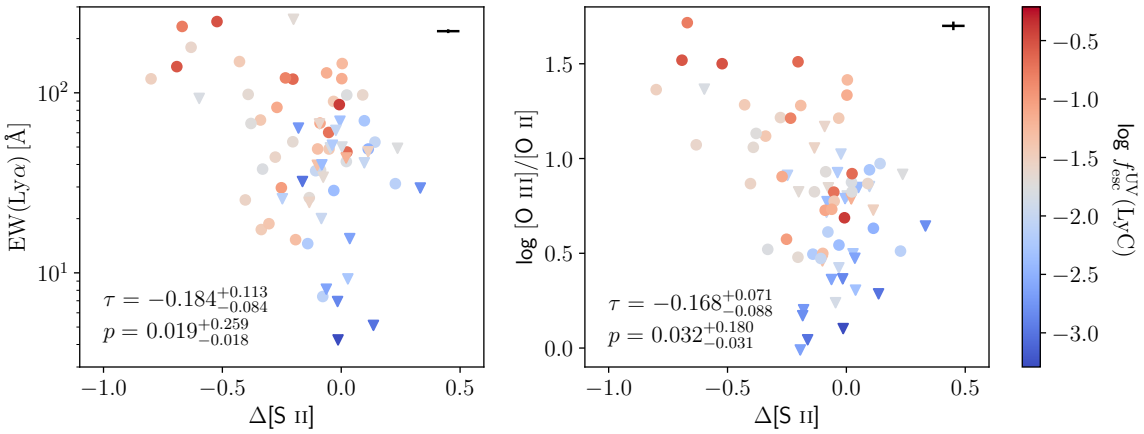

Figure 3.3: Scatter plots showing correlations between Δ[S II] and other galaxy characteristics. Colors indicate $f_{\rm esc}$. Triangles indicate that the associated $f_{\rm esc}$ are upper limits. τ and p are Kendall's correlation coefficient and the p-value, respectively. All show substantial scatter; the rest of the plots can be found in Section 4.5.

compact. It is then reasonable to speculate that LyC escape can be made possible by the extreme feedback effects produced by a "dominant central object." These objects are defined to be compact, very massive, and young objects located at or near the galactic nucleus (Heckman et al., 2011; Borthakur et al., 2014). Similar findings have likewise been reported in Wang et al. (2019); Hogarth et al. (2020); Kim et al. (2020, 2021).

Although adopting the standard discriminant of $p = 0.05$ means that most of the correlations are not significant, we do see significant additional correlations with EW($H\beta$), $M_{\rm FUV}$, $M_{\rm NUV}$, [O III]/[O II], and SFR$_{\rm UV}/M_\star$ In all cases, the scatter is substantial. This suggests that [S II] deficiency is providing information on LyC leakage that is largely independent of the other signposts.

To further demonstrate this, we construct pairs of [S II]-weak (Δ[S II] ≤ -0.2) and non-[S II]-weak galaxies ("twins") that share the closest values for each of the

Table 3.2: LCE Fractions in [S II]-weak Galaxies vs. Their Twins

	LCE Fraction[a]	Sig.[b]	Strong LCE Fraction	Sig.
$f_{\rm esc}$(Lyα)	0.59 ± 0.09	2.34	0.18 ± 0.09	2.97
[O III]/[O II]	0.62 ± 0.10	2.00	0.15 ± 0.10	3.02
[O I]/Hβ	0.62 ± 0.12	1.74	0.31 ± 0.12	1.78
EW(Hβ)	0.50 ± 0.11	2.76	0.21 ± 0.11	2.48
EW(Lyα)	0.71 ± 0.12	1.06	0.29 ± 0.12	1.91
EW(C II 1334)	0.47 ± 0.10	3.14	0.20 ± 0.10	2.66
EW(Si II 1260)	0.35 ± 0.09	4.33	0.18 ± 0.09	2.97
$M_{\rm FUV}$	0.54 ± 0.10	2.62	0.15 ± 0.10	3.02
$M_{\rm NUV}$	0.40 ± 0.09	4.06	0.13 ± 0.09	3.35
UV β	0.39 ± 0.10	3.88	0.22 ± 0.10	2.57
$M_\star$	0.53 ± 0.09	2.89	0.13 ± 0.09	3.35
r_{50}	0.56 ± 0.12	2.20	0.31 ± 0.12	1.78
SFR$_{\rm H\beta}$/area	0.47 ± 0.10	3.14	0.20 ± 0.10	2.66
SFR$_{\rm UV}$/area	0.59 ± 0.09	2.34	0.18 ± 0.09	2.97
SFR$_{\rm H\beta}/M_\star$	0.50 ± 0.11	2.78	0.25 ± 0.11	2.26
SFR$_{\rm UV}/M_\star$	0.47 ± 0.09	3.47	0.13 ± 0.09	3.35

[a] Pairs of [S II]-weak (Δ[S II] ≤ -0.2) and non-[S II]-weak galaxies sharing similar values of each parameter listed in column 1 are selected, and this column lists the LCE fractions in non-[S II]-weak samples. These can be compared to the LCE fraction in the [S II]-weak sample of 0.86 ± 0.07, and to the strong LCE of 0.59 ± 0.10.

[b] Significance in the difference between a LCE fraction in the [S II]-weak sample and that in the non-[S II]-weak sample.

other parameters shown in Figure 3.3 and in Section 4.5. For example, in the case of the EW(Lyα) parameter, for each [S II]-weak galaxy, we find a non-[S II]-weak galaxy that is the closest match in EW(Lyα). When one galaxy has multiple twins, we remove the duplicates from calculations. We then compare LCE fractions between the two subsamples and test the statistical significance of the difference. The results

are listed in Table 3.2. We note that LCE fractions in the [S II]-weak sample are greater than those in the twin samples in all cases, although for some parameters the large uncertainties due to the relatively small sample size lead to statistically insignificant results.

3.5 Discussion

3.5.1 Implications for Photoionization Models

Fundamentally, there are two different mechanisms by which LyC leakage can occur from a star-forming region—a density-bounded nebula and a radiation-bounded nebula with holes (Zackrisson et al., 2013). The former refers to a scenario in which regions undergoing intense stellar formation fully ionize their surroundings and have ionizing photons leftover that can escape, while the latter refers to a "picket-fence" scenario in which supernovae or stellar winds clear out low-density channels in the neutral ISM, through which LyC photons escape (Bergvall et al., 2006).

The density-bounded case is the simplest picture explaining the correlation between weak [S II] and LyC escape, as the absence of H I near the edge of a Strömgren sphere leads to a significant decrease in [S II] emissions. However, a simple density-bounded model cannot account for the majority of LyC detections in UV absorption-line studies (Chisholm et al., 2018; Gazagnes et al., 2018), and for the observed optical emission-line ratios (Ramambason et al., 2020).

The "picket-fence" model therefore seems to be favored by observations. In this case, [S II] deficiency indicates that a significant fraction of the total solid angle as seen from the star-forming region is optically thin in the LyC. We also note that

a reduced column density of the neutral gas in the fence is required to explain the largest observed $f_{\rm esc}$ (Gazagnes et al., 2020; Ramambason et al., 2020).

Instead of the above two classical one-zone models, Ramambason et al. (2020) propose two-zone photoionization models, in which ionization parameters and covering fractions are varied along different lines of sight. The two-zone models successfully reproduce the observed emission-line properties in low-z LCEs, including [S II] deficiency, and are compatible to results from UV absorption-line studies.

In Figure 3.4 we show schematic diagrams of such a two-zone model for a LCE and a non-LCE in the context of a simple windblown shell. In the former case, only the optically thick clouds contribute to [S II] emission while both the clouds and the optically thin regions between the clouds contribute to emission from Balmer and high-ionization metal lines. In the latter case the entire shell contributes to the [S II] emission.

3.5.2 Implications for Escape Fractions

The relationship between Δ[S II] and $f_{\rm esc}$ shows substantial scatter, as evident in Figure 3.5. Generalized Kendall's τ correlation coefficients which account for upper limits in $f_{\rm esc}$ are listed in Table 3.1 (Isobe et al., 1986). Our finding is in agreement with Ramambason et al. (2020), who find that although [S II] deficiency can select LCE candidates, it is not obvious how to infer a numerical value for $f_{\rm esc}$ directly from Δ[S II].

Several factors could contribute to the observed complexity. The simplest explanation is line-of-sight variations caused by porous H II regions. Observations from the Keck Lyman Continuum Spectroscopic Survey (Steidel et al., 2018) and another sam-

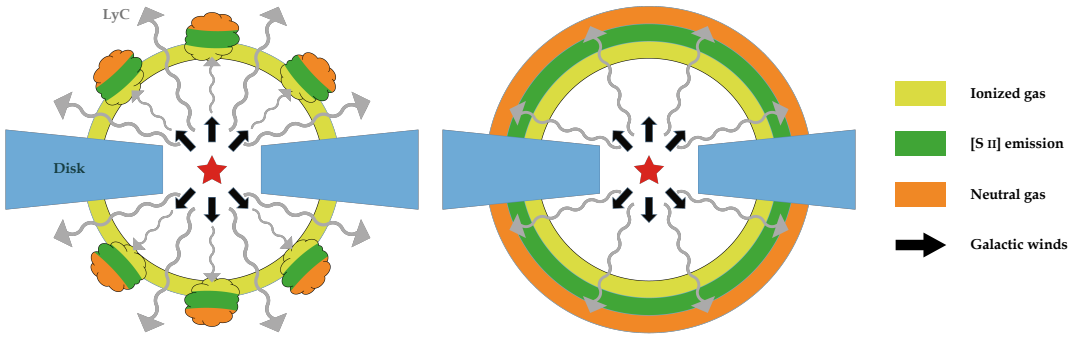

Figure 3.4: Schematic diagrams for a LCE (left panel) and a non-LCE (right panel) in the context of a simple wind-blown shell. In the case of a LCE, only the optically thick clouds contribute to [S II] emission while both the clouds and the optically thin regions between the clouds contribute to emission from Balmer and high ionization metal lines. In the case of a non-LCE, the entire shell contributes to the [S II] emission. We note that they only represent the simplest cases where isotropy is assumed.

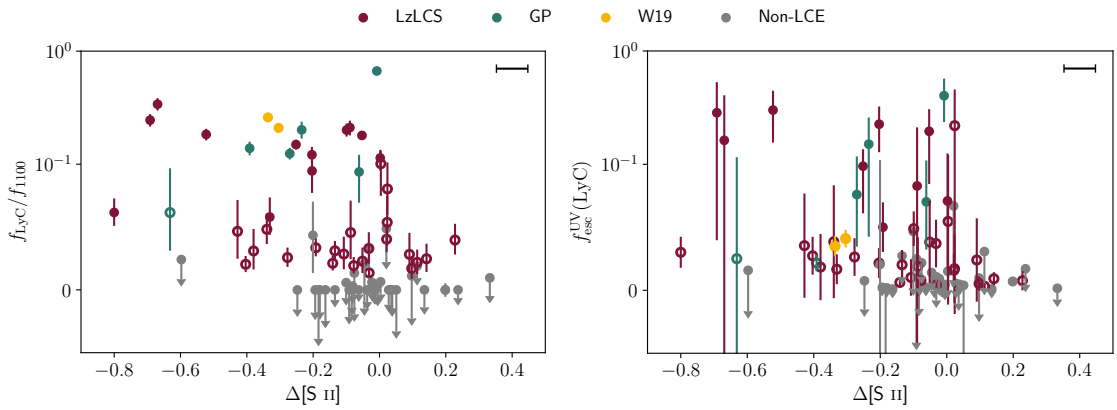

Figure 3.5: Escape fractions are plotted as functions of [S II] deficiency. A linear scale is used for $f_{esc} < 0.1$. Colored dots represent strong LCEs, circles represent weak LCEs, and gray dots represent upper limits. Most of the [S II]-deficit galaxies (Δ[S II] $\lesssim -0.2$) are LCEs, but only weak (albeit statistically significant) correlations are found with f_{esc} (see Table 3.1).

ple of galaxies at $z \sim 3$ having high [O III]/O II] but low $f_{\rm esc}$ (Nakajima et al., 2020) are both consistent with this picture. Using resolved stars to measure $f_{\rm esc}$ also shows that $f_{\rm esc}$ can vary significantly both due to the viewing angle and spatial resolution, even for the same galaxy (Choi et al., 2020).

A complication, though, arises from the possibility of anisotropically escaping LyC photons (e.g., Zastrow et al. 2011; Cen and Kimm 2015). This directly leads to ambiguity in the interpretation of non-detections—it is unclear if a galaxy not observed to have LyC escaping is truly a nondetection or if this is due to a particular orientation toward the observer. With a larger sample, we would be able to infer the fraction of LCEs with its proportional relationship to the H I covering fraction.

In short, an intricate interplay among factors dictates $f_{\rm esc}$. Althoug unified models for describing different samples of LCEs have been proposed (Cen, 2020), it is likely that a combination of other properties (e.g., those shown in Figure 4 and with Mg II studied in Henry et al. 2018; Chisholm et al. 2020) is needed for accurately inferring $f_{\rm esc}$.

In the face of this complexity, it seems that the determination of leakiness based on indirect signposts can only be done on a statistical basis rather than for individual objects (see Runnholm et al. 2020 for predicting Lyα radiation using multivariate regression). This reinforces the need for large samples, which was the main driver for the LzLCS. Even larger samples will ultimately be needed in the future.

3.5.3 Analogs to High-z Galaxies

Having discussed what can be learned from low-z LCEs, this final subsection addresses whether they can truly represent the galaxies during the EoR. One question is the

degree to which our definition of [S II] deficiency is based on galaxies at low z, which differ significantly from EoR galaxies. This can be addressed through spectroscopy using the James Webb Space Telescope (JWST) to construct BPT/VO diagrams like Figure 3.1 for EoR galaxies. It is promising that galaxies at $\langle z \rangle \sim 2.3$ do follow the same locus as low-z galaxies in Figure 3.1 (Strom et al., 2018; Wang et al., 2019).

In a recent analysis of simulated Lyman-break galaxies, Katz et al. (2020) claim that the sample of $z \sim 3$ LCEs (Nakajima et al., 2020) are good analogs of EoR galaxies, while the [S II]-deficient galaxies in W19 may not necessarily be so. The argument is largely based on whether the analogs populate the same regions in respective BPT/VO diagnostic diagrams. Katz et al. (2020) find that the LCEs in their simulations have deficits both in [S II] and [O III], indicating that the dominant effect is metallicity or mass rather than a property of the ISM.

We agree that metallicity or mass possibly play important roles (Jaskot et al., 2019), especially given that many LCEs fall at the top (metal-poor) end of the BPT/VO diagram as shown in Figure 3.1. It is also true that galaxies are intrinsically complex systems, and thus it is difficult to disentangle primary and secondary correlations. The issue of whether high-z and local galaxies can be analogs to one another is further complicated by the finding based on the MOSDEF–LRIS Survey that a similarity in the location of high-z and local galaxies in the BPT/VO diagrams may not always be indicative of a similarity in their physical properties (Topping et al., 2020).

In general, while simulations shed light on the study of EoR galaxies, the multiphase nature of the interstellar and circumgalactic media as well as the high spatial resolution needed to explicitly simulate the LyC-escaping process reinforce the need

for robust observational evidence. Given the relatively small pool of LCEs, the different physical properties exhibited by some of the [S II]-deficient LCEs nevertheless offer valuable insights into the possibly different ways in which LyC can escape from galaxies.

3.6 Conclusions

We have reported on using the relative weakness of the [S II] 6717, 6731 nebular emission lines defined with respect to normal star-forming galaxies as an indicator for galaxies that are optically thin to ionizing radiation. This method was proposed in Wang et al. (2019), and statistically tested in this paper with new HST/COS observations of 66 star-forming galaxies in LzLCS (Flury et al., 2021a). We find that [S II] deficiency is an effective way to identify candidates for LyC-emitting galaxies, and can complement other proposed LyC predictors.

More specifically, we have shown that the LyC-emitting galaxies are more [S II]-deficient than the other galaxies, that the detection fraction of them increases strongly as a function of [S II] deficiency, and that the value of the far-UV based escape fractions have statistically significant (but weak) correlations with [S II] deficiency. In addition, we have also shown that [S II] deficiency does not show a significant correlation with most of the other proposed indirect signposts of LyC leakage with the exception of the compactness of the starburst. This implies that [S II] deficiency is an independent indicator of LyC leakage.

We have discussed the photoionizing process in light of the scatter seen in the relationship between [S II] deficiency and $f_{\rm esc}$. This likely indicates line-of-sight varia-

tions in ionization parameters and covering fractions, and/or anisotropically escaping LyC photons, which is in agreement with several other studies at low to intermediate redshifts (Steidel et al., 2018; Ramambason et al., 2020).

To summarize, the increased sample size of low-z LyC-emitting galaxies from LzLCS allows us to statistically confirm that [S II] deficiency is a robust technique for finding galaxies leaking a significant amount of the LyC radiation. Although it is yet not obvious how accurately the numerical value of the escape fraction of LyC could be inferred from [S II] deficiency for individual galaxies, it is very useful in the context of statistical estimates for samples of galaxies. This gives us an additional technique to identify potential LyC-emitting galaxies at low z and during the EoR with future observations with the JWST.

B.W. thanks Yiwei Sun for help making the schematic diagrams. This work is supported by HST-GO-15626, provided by NASA through a grant from the Space Telescope Science Institute, which is operated by the Association of Universities for Research in Astronomy, Inc., under NASA contract NAS5-26555. This publication made use of the NASA Astrophysical Data System for bibliographic information. This project also made use of SDSS data. Funding for the Sloan Digital Sky Survey IV has been provided by the Alfred P. Sloan Foundation, the U.S. Department of Energy Office of Science, and the Participating Institutions. SDSS-IV acknowledges support and resources from the Center for High-Performance Computing at the University of Utah. The SDSS web site is www.sdss.org. SDSS-IV is managed by the Astrophysical Research Consortium for the Participating Institutions of the SDSS Collaboration including the Brazilian Participation Group, the Carnegie Institution for Science, Carnegie Mellon University, the Chilean Participation Group, the

French Participation Group, Harvard-Smithsonian Center for Astrophysics, Instituto de Astrofísica de Canarias, The Johns Hopkins University, Kavli Institute for the Physics and Mathematics of the Universe (IPMU) / University of Tokyo, the Korean Participation Group, Lawrence Berkeley National Laboratory, Leibniz Institut für Astrophysik Potsdam (AIP), Max-Planck-Institut für Astronomie (MPIA Heidelberg), Max-Planck-Institut für Astrophysik (MPA Garching), Max-Planck-Institut für Extraterrestrische Physik (MPE), National Astronomical Observatories of China, New Mexico State University, New York University, University of Notre Dame, Observatário Nacional / MCTI, The Ohio State University, Pennsylvania State University, Shanghai Astronomical Observatory, United Kingdom Participation Group, Universidad Nacional Autónoma de México, University of Arizona, University of Colorado Boulder, University of Oxford, University of Portsmouth, University of Utah, University of Virginia, University of Washington, University of Wisconsin, Vanderbilt University, and Yale University.

Appendix

Here we list the LCE classifications of all galaxies in LzLCS, the remeasured SDSS [S II] flux, and [S II] deficiency in Table 3.3. The scatter plots in Figure 3.6 show correlations between Δ[S II] and other galaxy characteristics in the same way as Figure 3.3. The scattering is substantial in all cases.

Table 3.3: Flux Measurements of Galaxies in LzLCS.

Galaxy	LCE Type[a]	[S II]	Δ[S II]
J0036	×	8.17 ± 4.44	-0.60 ± 0.24
J0047	○	51.06 ± 4.63	0.02 ± 0.04
J0113	○	45.98 ± 10.24	0.23 ± 0.10
J0122	○	11.81 ± 3.82	-0.34 ± 0.14
J0129	×	98.92 ± 10.38	-0.10 ± 0.05
J0723	×	54.75 ± 2.56	0.00 ± 0.02
J0804	●	4.33 †	-0.67
J0811	○	1.60 †	-0.80
J0814	×	207.83 ± 7.99	-0.03 ± 0.02
J0826	×	19.14 ± 5.77	-0.25 ± 0.13
J0834	×	104.46 ± 12.70	-0.01 ± 0.05
J0909	●	4.30	-0.69
J0911	○	149.60 ± 13.13	-0.20 ± 0.04
J091207	×	124.31 ± 4.79	-0.05 ± 0.02
J091208	×	44.18 ± 4.50	-0.08 ± 0.04
J0917	●	79.66 ± 8.61	-0.25 ± 0.05
J0925	×	20.05 ± 29.71	-0.08 ± 0.64
J0933	●	11.55 ± 4.00	-0.52 ± 0.15
J0940	×	49.59 ± 5.64	0.03 ± 0.05
J0952	○	9.64 ± 7.02	-0.40 ± 0.32
J0957	×	302.97 ± 14.10	-0.19 ± 0.02
J0958	○	13.43 ± 10.01	-0.38 ± 0.32
J1014	×	23.52 ± 3.09	-0.18 ± 0.06
J1026	○	23.63	0.14
J1033	●	72.51 ± 11.64	-0.05 ± 0.07

(To be continued)

Galaxy	LCE Type	[S II]	Δ[S II]
J1038	○	158.05 ± 8.43	-0.14 ± 0.02
J1051	×	45.32 ± 4.46	0.04 ± 0.04
J1053	○	225.05 ± 15.12	-0.08 ± 0.03
J1055	×	36.27 ± 4.04	0.14 ± 0.05
J1104	×	32.19 ± 4.98	0.11 ± 0.07
J1122	○	11.44 ± 5.24	0.00 ± 0.20
J1128	○	26.65 ± 3.34	0.11 ± 0.06
J1129	×	15.49 ± 3.67	-0.04 ± 0.11
J1133	○	41.98 ± 8.48	-0.09 ± 0.09
J1158	○	218.07 ± 12.62	-0.10 ± 0.03
J1159	○	8.38 ± 2.68	-0.43 ± 0.14
J1209	×	164.70 ± 6.13	-0.08 ± 0.02
J1219	○	22.67	-0.11
J1235	•	29.19 ± 11.95	-0.19 ± 0.18
J1240	×	21.31	-0.13
J1244	×	264.26 ± 11.60	0.10 ± 0.02
J1246	○	87.90 ± 4.44	0.10 ± 0.02
J1248	○	108.88 ± 9.37	0.09 ± 0.04
J1249	×	26.51 ± 4.13	0.05 ± 0.07
J1255	×	53.52	0.24
J1257	×	46.72 ± 4.23	-0.02 ± 0.04
J1300	×	6.14	-0.18
J1301	○	55.34 ± 13.69	-0.13 ± 0.11
J1305	•	10.05	-0.20
J1310	○	37.72 ± 8.34	-0.33 ± 0.10
J1314	×	178.42 ± 11.23	-0.02 ± 0.03

(To be continued)

Galaxy	LCE Type	[S II]	Δ[S II]
J1319	×	78.26 ± 7.72	-0.16 ± 0.04
J1326	○	72.90 ± 5.34	0.02 ± 0.03
J1329	×	145.64 ± 15.73	-0.01 ± 0.05
J1345	×	208.06 ± 11.61	0.04 ± 0.02
J1350	×	39.36	0.33
J1403	○	27.32 ± 23.46	-0.03 ± 0.37
J1410	●	24.62 ± 2.44	0.00 ± 0.04
J1440	○	199.28 ± 11.96	-0.03 ± 0.03
J1517	●	78.45 ± 4.58	-0.09 ± 0.03
J1540	×	189.29 ± 12.16	-0.06 ± 0.03
J1559	×	90.14 ± 7.19	0.02 ± 0.03
J1604	×	34.26 ± 7.46	-0.09 ± 0.09
J1646	○	26.62 ± 11.65	-0.28 ± 0.19
J1648	○	11.68 ± 2.90	0.02 ± 0.11
J1720	○	28.40	-0.05

[a] Classes of LCEs: • strong LCEs, ○ weak LCEs, × non-LCEs.

[†] Upper limit inferred from $3\,\sigma$ background.

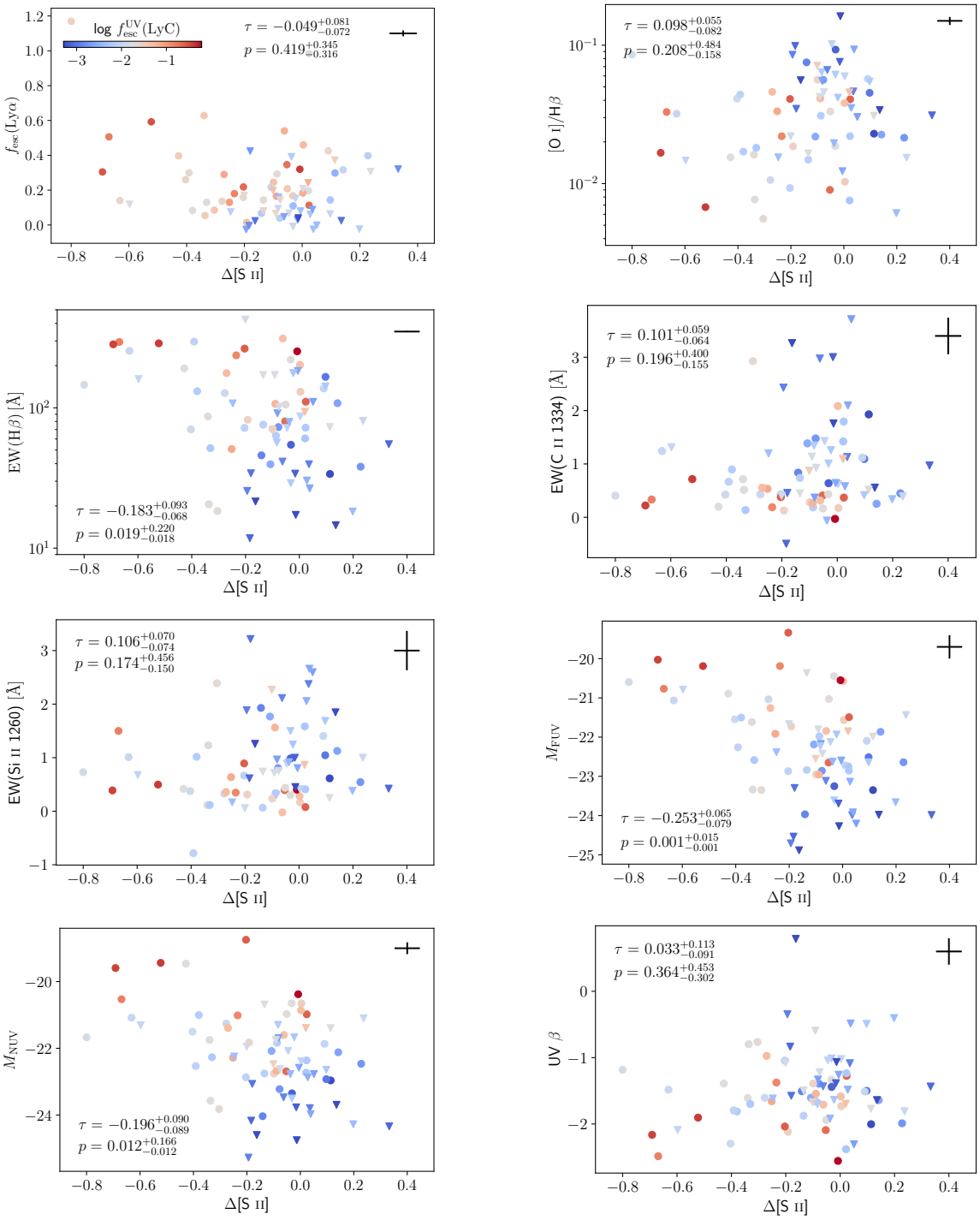

Figure 3.6: Same as Figure 3.3, but with different galaxy characteristics. Colors indicate $f_{\rm esc}$. Triangles indicate that the associated $f_{\rm esc}$ are upper limits. τ and p are Kendall's correlation coefficient and the p-value, respectively.

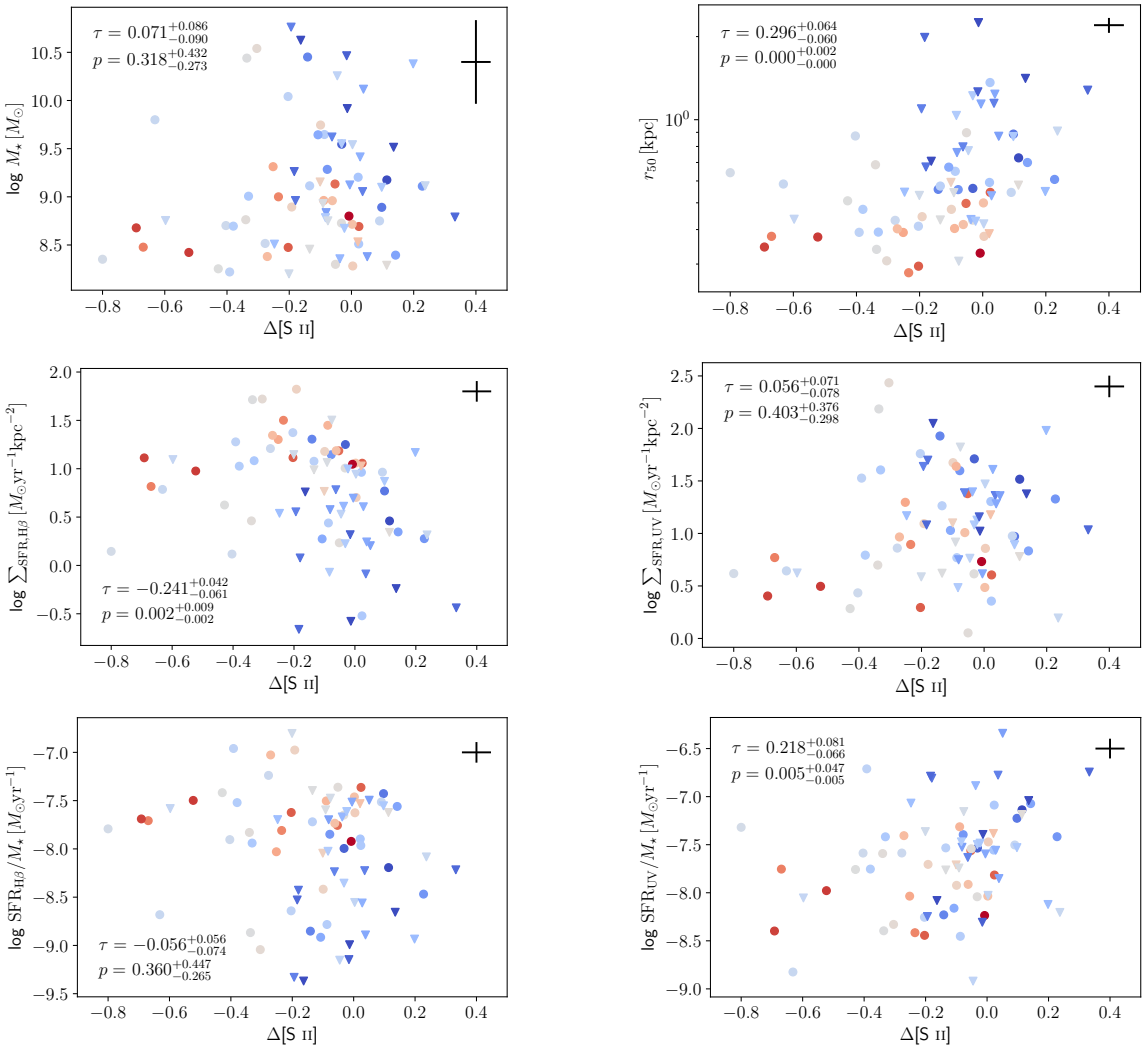

Figure 3.6: (Continued.)

Chapter 4

A Systematic Study of Galactic Outflows via Fluorescence Emission: Implications for Their Size and Structure

4.1 Introduction

Galactic outflows are invoked as the principal feedback mechanism in models of galaxy formation and evolution. Despite of a general agreement on their importance in regulating the galactic baryonic cycle, outflows are often parameterized in models or simulations by descriptions based on simple theoretical arguments and/or empirical relations. This is because the interplay among the relevant physical processes operates at scales below the resolution of any current simulation (see Somerville and Davé 2015,

and references therein).

Detailed observations of outflows spanning multiple scales would provide valuable inputs for "sub-grid" physics in simulations as well as help contribute to a more complete understanding of feedbacks, but they too have been proven to be difficult; see Veilleux et al. (2005); Heckman and Thompson (2017); Veilleux et al. (2020) for recent reviews. Most of our knowledge has come from data on resonance lines seen in absorption in "down-the-barrel" spectra, from which characteristic outflow speeds and column densities can be inferred (e.g., Heckman et al. 2000, 2015; Chisholm et al. 2017). Unfortunately, those data alone provide little information on the radial structure of outflows, since they result from the integrated absorption along the line of sight. This makes it difficult to assess how and where outflows impact the rest of the galaxy's gas supply.

One problem in particular is that the estimation of the outflow rates derived from the absorption lines depends directly on the effective size that is assumed for the absorbing material. That is, simple dimensional analysis implies that the mass outflow rate will be proportional to the column density times the outflow velocity times the outflow size. The first two quantities can be estimated from the absorption-line data, but the outflow size cannot. It is often assumed to be on the order of a few times the radius of the starburst (e.g., Heckman et al. 2015). Thus, one of the most important missing pieces of data would be an estimate of the size of the region of outflowing absorbing material.

This requires mapping the outflow in emission. While this is commonly done using nebular emission lines like Hα (e.g., Armus et al. 1990), these nebular lines may not fairly trace the same material seen in absorption (they preferentially trace the

highest-density gas). Ideally, the outflow could be mapped using the resonance lines in themselves in emission. Many of these resonance transitions also have associated transitions to excited fine-structure levels that can produce fluorescence emission lines (e.g., Rubin et al. 2011; Erb et al. 2012; Jones et al. 2012; Tang et al. 2014; Finley et al. 2017). These fluorescence lines offer a major advantage over the resonance lines for probing the outflow structure. This is because it is not straightforward to disentangle the separate contributions of emission and absorption to the observed properties of the resonance lines. In contrast, the fluorescence lines are always optically thin, and (in most cases) sufficiently offset in wavelength from the associated resonance lines that the profiles of the fluorescence and resonance lines are unaffected by the other. For this reason, the fluorescence emission lines will be the focus of this paper.

According to standard outflow models (Prochaska et al., 2011; Scarlata and Panagia, 2015; Zhu et al., 2015), the observed resonance absorption takes place in material located directly along the line-of-sight toward a background light source. For each absorbed resonance photon, a photon will be re-emitted isotropically. For ions with fine-structure splitting, this can either be a resonantly scattered photon or a fluorescent photon. In the simple case of a spherically symmetric outflow with no dust, the number of photons is conserved, such that the net absorbed flux should be equal to the sum of the resonantly scattered and fluorescence emission. In contrast, observations typically show that the emission lines are significantly weaker than the absorption lines (e.g., Erb et al. 2012; Kornei et al. 2013; Tang et al. 2014; Alexandroff et al. 2015; Finley et al. 2017; Finley et al. 2017; Steidel et al. 2018). There are a number of ways in which weaker emission can occur. The most straightforward explanation is that the angular size of the absorbing/emitting region significantly exceeds the

size of the spectroscopic aperture ("slit loss"). This has been directly established for the Lyα emission line in Lyman Break Galaxies (LBGs; Steidel et al. 2011). We are particularly interested in testing this possibility more generally, since it would have direct implications for the size and radial structure of outflows. In this paper, we therefore undertake a systematic comparison of the properties of the fluorescence emission lines and resonance absorption lines for a sample of star-forming galaxies driving outflows. We will utilize a combination of information coming from both ultraviolet (UV) spectroscopy and imaging.

The structure of this paper is as follows. In Section 4.2 we summarize the observational data sets, including both the new data taken by the Hubble Space Telescope (HST) and archival data, as well as their analysis. In Section 4.3 we present results on the relative strengths and widths of the fluorescence emission lines from the Cosmic Origins Spectrograph (COS; Green et al. 2012), and discuss imaging of the fluorescence emission from the Wide Field Camera 3 (WFC3). In Section 4.4 we highlight correlations between line strengths and galaxy/starburst properties, and discuss implications for wind structure. We then conclude our findings in Section 4.5.

All the transitions considered in this paper are listed in Table 4.1. Also, when applicable, we adopt the best-fit cosmological parameters from the Planck 2018 analysis: $H_0 = 67.66$ km s^{-1} Mpc^{-1}, $\Omega_M = 0.311$, and $\Omega_\Lambda = 0.690$ (Planck Collaboration et al., 2020b).

Table 4.1: Atomic Data for the Transitions Considered

	λ (Å)	$A_{\rm ul}$ (s^{-1})	$f_{\rm lu}$	$E_{\rm l}$ (cm^{-1})	$E_{\rm u}$ (cm^{-1})
Si II	1190.42	6.53×10^{8}	0.277	0	84004.26
	1193.29	2.69×10^{9}	0.574	0	83801.95
Si II*	1194.50	3.45×10^{9}	0.738	287.24	84004.26
	1197.39	1.40×10^{9}	0.150	287.24	83801.95
Si II	1260.42	2.57×10^{9}	1.224	0	79338.50
Si II*	1265.00	4.73×10^{8}	0.113	287.24	79338.50
Si II	1304.37	3.64×10^{8}	0.093	0	76665.35
Si II*	1309.28	6.23×10^{8}	0.080	287.24	76665.35
Si II	1526.72	3.81×10^{8}	0.133	0	65500.47
Si II*	1533.45	7.52×10^{8}	0.134	287.24	65500.47
Fe II	2586.65	8.94×10^{7}	0.072	0	38660.05
	2600.17	2.35×10^{8}	0.239	0	38458.99
Fe II*	2612.65	1.20×10^{8}	0.122	384.7872	38660.05
	2626.45	3.52×10^{7}	0.046	384.7872	38458.99

Note. Data are taken from the NIST Atomic Spectra Database.

4.2 Data

4.2.1 Sample Selection

In the HST program GO-15340 (PI T. Heckman) we observed a sample of five galaxies with COS and WFC3. They were selected from Sloan Digital Survey (SDSS) based on the following criteria.

1. Redshift range $0.064 < z < 0.066$. This range is determined by the transmission curve of F280N, which covers Fe II* 2626 at $0.057 < z < 0.072$. A narrower redshift range is chosen to ensure the coverage of the bluer Fe II* 2613 line, while excluding the Fe II 2600 absorption.

2. Specific star-formation rate (sSFR) greater than $10^{-9}\mathrm{yr}^{-1}$ and equivalent width (EW) of [O II] greater than 50 Å. Together they indicate substantial starbursts—and therefore large outflow rate and extended fluorescence emission.

3. NUV magnitude less than 19 mag. This ensures the feasibility for COS G130M observations.

4. Diverse morphology. About 50 galaxies that pass the above criteria are categorized based on the optical morphology, including inclination. The galaxy with the highest NUV flux and/or [O II] EW is selected in each group.

5. An estimated NUV flux of the star-bursting region inside a 3″ aperture less than 19.5 mag. This is inferred by assuming the difference between the total magnitude and the aperture magnitude in the NUV to be about the same as that in the SDSS u-band.

The resulting sample is listed in Table 4.2.

4.2.2 Archival Data

In addition to the five new observations listed above, we also include the following four samples from the literature.

Table 4.2: Observation Logs

	Galaxy	z	WFC3 Filter/COS Grating (Central Wavelength)	Exposure Time (s)
J0831(S)	GALEX-J083101.8+040317	0.065	F280N (2832.2)	1560+1560+2400
			F343N (3435.3)	720
			F395N (3955.2)	720
			G130M (1291)	4928.384
			MIRRORA	270
J0831(N)	GALEX-J083101.8+040318	0.064	G130M (1291)	4928.352
			MIRRORA	270
J1157	GALEX-J115747.0+583503	0.064	F280N (2832.2)	1840+1760+2640
			F343N (3435.3)	720
			F395N (3955.2)	720
			G130M (1291)	5425.344
			MIRRORA	270
J1210	GALEX-J121014.3+443958	0.065	F280N (2832.2)	1600+1600+2520
			F343N (3435.3)	720
			F395N (3955.2)	720
			G130M (1291)	2060.384
			MIRRORA	170
J1618	GALEX-J161832.6+274352	0.065	F280N (2832.2)	1600+1560+2400
			F343N (3435.3)	720
			F395N (3955.2)	720
			G130M (1291)	2060.320
			MIRRORA	150

First, we analyze the individual spectra of the Lyman break analogs (LBAs), which were previously investigated by Heckman et al. (2011); Alexandroff et al. (2015) (HST-GO-11727 and HST-GO-13017; PI T. Heckman). Second, we consider the Lyα-

emitting galaxies (LAEs) as compiled in Scarlata and Panagia (2015). Finally, we compare to two samples of high-z ($z \gtrsim 3$) galaxies: the LBGs (Jones et al., 2012) and star-forming galaxies in the Keck Lyman Continuum Spectroscopic Survey (KLCS; Steidel et al. 2018).

4.2.3 Data Processing and Analysis

Spectra

A COS FUV spectrum usually consists of two segments. In our case, one segment covers the observed wavelength range approximately from 1286 Å to 1429 Å while another one covers from 1131 Å to 1274 Å. We first convert both segments to the rest frame of the galaxy, and then merge and smooth them with Gaussian kernels of $\sigma \sim 0.14$ Å. An average is taken for any overlapping parts, weighted by the respective inverse uncertainties. We then remove the spectral features produced by stars using synthetic spectra generated from Starburst99 (hereafter SB99; Leitherer et al. 1999) in order to focus on the properties of the interstellar gas. The models are produced based on a star formation history of a continuous and constant rate of star formation. The stellar population, parameterized by a Kroupa initial mass function (IMF; Kroupa 2001), evolves from the zero-age main sequence using the evolutionary models of the Geneva Group. Both spectra are normalized to some local continuum near the spectral lines of interest. Those spectra are shown in three segments in Figure 4.1, each zooming in on: (1) Si II 1190, Si II 1193, Si II* 1195; (2) Si II 1260, Si II* 1265; and (3) Si II 1304, Si II* 1309.

We fit the spectral lines with Gaussians—or multi-component Gaussians in the

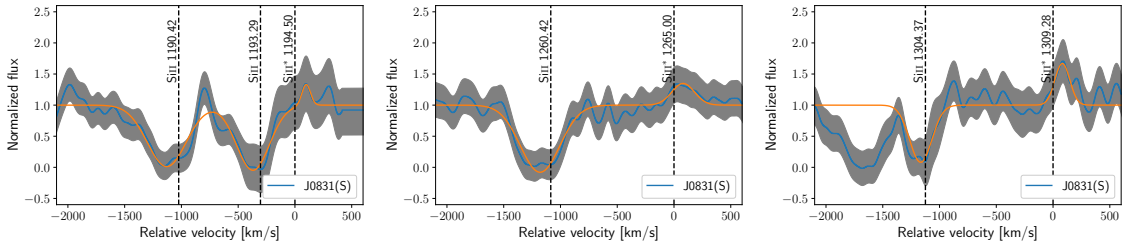

Figure 4.1: Continuum-normalized spectra of J0831(S) with the stellar features removed, zooming in on lines of interest. Gray shades indicate $1\,\sigma$ uncertainty. Overplotted in orange are the Gaussian fits. Each velocity scale is relative to the vacuum wavelength of the fluorescence emission line. Similar plots for the rest of the four galaxies can be found in the Appendix.

case of blended lines. We then measure EW, full width at half maximum (FWHM), and velocity centroid ($V_{\rm ctr}$). Since stellar features including the stellar continuum are removed, the average continuum level in the processed spectra lies at zero. For the purpose of defining the EW, we shift each spectrum along the y-axis to have the continuum lie at unit flux. Unless otherwise stated, all measurements can be assumed to have errors on the order of 10-15% dominated by systematics in the polynomial fit to the continuum and subtraction of the SB99 models. We provide all the measurements in tabular form in the Appendix.

Unfortunately, at $z \sim 0.065$, the Si II* 1309 line is likely to be contaminated by the Milky Way (MW) absorption line Si IV 1394. We check this by looking for another MW absorption line Si IV 1402.8. The Si II* 1309 lines in the spectra of J0831(N), J1157, and J1618 display various degrees of contamination.

Imaging

Images were taken with UVIS/F280N, F343N, and F395N filters on the WFC3, all of which were reprocessed with the standard pipeline `astrodrizzle`. We align them

through spline interpolation to achieve subpixel precision. The three exposures of F280N are stacked via exposure-time–weighted average, while the cosmic rays in the single exposures of F343N and F395N are identified using the L.A.Cosmic algorithm (van Dokkum, 2001; McCully et al., 2018) and subsequently masked. All the images are then converted from units of electron s^{-1} per pixel to that of flux density in erg cm^{-2} s^{-1} $Å^{-1}$ per pixel. As the F343N filter maps the UV stellar continuum, an Fe II* image is obtained by subtracting an F343N image from the stacked F280N one, and an [O II] 3727 image is obtained by subtracting it from the F395N one.

We see small but systematic variations in the residual background in these difference images. We therefore undertake an additional step in subtracting this spatially-varying residual background. We estimate it on a mesh whose cells have scales larger than the source, but small enough to encapsulate the background variations. After subtracting the inferred spatially varying background, we examine the histogram showing the distribution of individual pixel values after five sigma-clipping, and ensure that it follows a Gaussian centered around zero.

We show contours of the continuum-subtracted Fe II* and [O II] overplotted on the continuum images in Figure 4.2. The radial surface brightness as shown in Figure 4.3 is measured in a set of apertures/annuli, which centers on the strongest peak found in the continuum and extends to 6.4″. We estimate the uncertainty by measuring the flux in the same set of apertures/annuli centered on many locations of the blank sky, and then quote the $1\,\sigma$ values of the Gaussian fits to the distribution of background fluctuations.

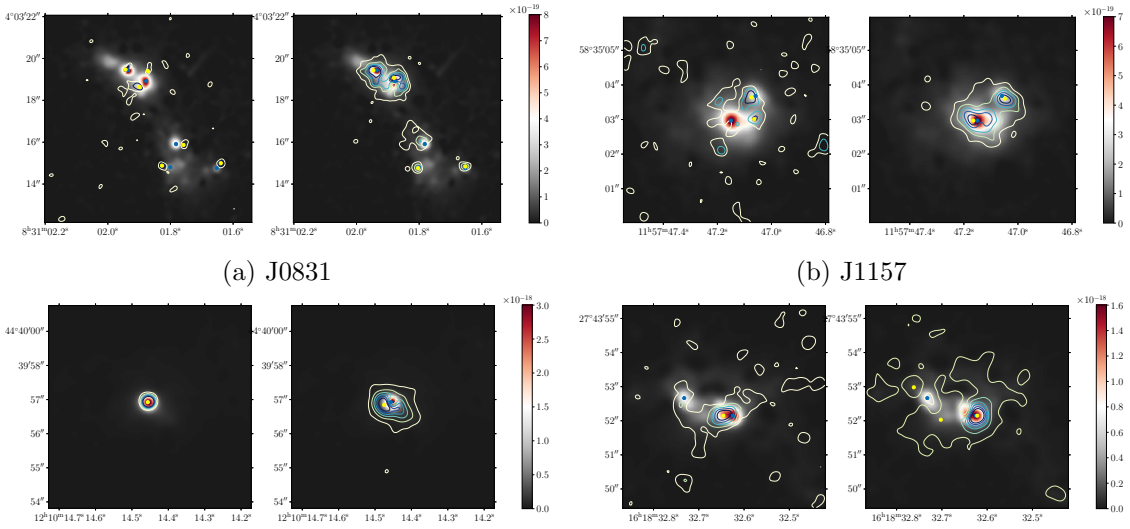

(a) J0831 (b) J1157

(c) J1210 (d) J1618

Figure 4.2: Contours of the continuum-subtracted Fe II* (left) and [O II] (right) images overplotted on the continuum images for each galaxy. Peaks of the emission-line images are shown in yellow, while those of the continuum images are shown in blue. Note that all images are smoothed with a Gaussian of FWHM = 0.01″. Angular scale is indicated on the y-axis.

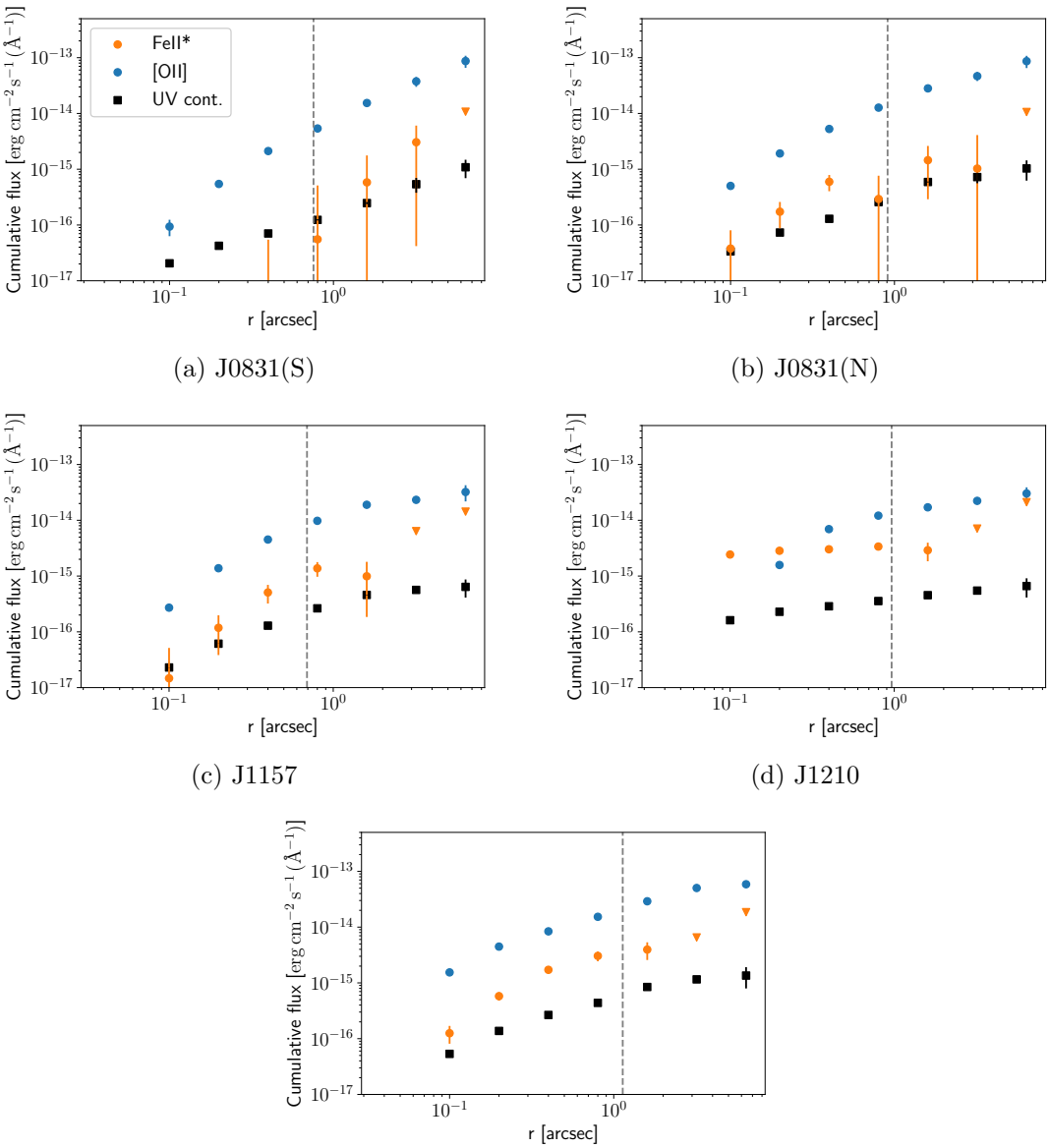

(a) J0831(S)

(b) J0831(N)

(c) J1157

(d) J1210

(e) J1618

Figure 4.3: Enclosed flux plotted as a function of radius. Data points for Fe II* and [O II] shown in dots are in units of flux, whereas those for the UV continuum shown in black squares are in units of flux density. Triangles are upper limits estimated from background fluctuations. Gray dashed lines indicate the r_{50} of each WFC3 UV continuum image. We infer that nearly all of the detectable Fe II* emission is from inside the starburst region, and is associated with regions of high surface brightness in [O II] and the UV continuum.

Archival data

The individual spectra of the LBAs are reanalyzed according to the description given in Section 4.2.3. For the sake of consistency, we include only galaxies with COS data and with the set of galaxy parameters that can be measured using the spectra in the SDSS. Their Si II and Si II* line profiles are attached in the Appendix.

We also remeasure the EWs, FWHMs, and velocity centroids of the Si II and Si II* lines in the composite spectrum of 25 LAEs at $z \sim 0.3$ (Scarlata and Panagia, 2015).

As for the LBGs, we take the measurements of the two stacked spectra, which were obtained from two subsamples distinguished by redshifts, from the original paper (Jones et al., 2012). The mean redshifts are 3.76 and 4.70 respectively.

4.2.4 Measured Ancillary Parameters

In this section, we list important ancillary parameters, all of which are listed in Table 4.3. Most of them are determined in the same way as in Wang et al. (2019), so we only briefly reiterate the procedure here for completeness.

We measure the SFRs in two ways. In both cases, we use the same IMF as that used in our SB99 fit. $\mathrm{SFR_{IR}}$ is calculated by using the Wide-field Infrared Survey Explorer (WISE) IR data at 12 and 22 μm (Wright et al., 2010) to estimate the rest-frame 24 μm luminosity, and then using the relation given in Kennicutt and Evans (2012). $\mathrm{SFR_{H\alpha}}$ is calculated from extinction-corrected Hα and Hβ fluxes, and then using the relation given in Calzetti (2011).

We also determine the half-light radii, r_{50}, in two sets of images. First, the COS NUV ACQ images are used, as shown in Figure 4.4. Second, we use the WFC3 images

Table 4.3: Measured Ancillary Parameters for the Five Galaxies of This Paper and LBAs

	FWHM(Balmer)	$A_{H\alpha}$	$SFR_{H\alpha}$	$SFR_{IR,UV}$	$M_\star$	$12+\log(O/H)$	r_{50}(NUV)	r_{50}(UV cont.)	r_{COS}
	(km s^{-1})		($M_\odot yr^{-1}$)	($M_\odot yr^{-1}$)	(log $M_\odot$)		(kpc)	(kpc)	(kpc)
J0831(S)	224 ± 1	1.21 ± 0.04	6.2	17.9 ± 1.1	9.88	8.43	1.04	0.98	1.61
J0831(N)	205 ± 1	0.76 ± 0.03	7.0	12.0 ± 1.1	9.76	8.00	0.99	1.17	1.61
J1157	135 ± 1	0.26 ± 0.03	1.7	4.6 ± 0.3	9.42	8.25	0.70	0.89	1.60
J1210	235 ± 1	0.71 ± 0.03	4.6	10.4 ± 0.4	9.88	8.41	0.17	1.26	1.64
J1618	192 ± 1	0.35 ± 0.03	6.8	17.4 ± 0.4	9.28	8.15	0.63	1.45	1.60
J0055	339 ± 1	0.60 ± 0.02	28.8	23.6	9.70	8.28	0.32	-	3.70
J0150	240 ± 1	0.74 ± 0.03	20.0	37.4	10.30	8.40	1.37	-	3.31
J0213	218 ± 5	0.80 ± 0.11	5.7	19.0	10.50	8.76	0.39	-	4.57
J0808	362 ± 3	0.54 ± 0.04	4.3	8.5	9.80	8.77	0.08	-	2.20
J0921	395 ± 4	0.86 ± 0.06	23.4	29.4	10.80	8.69	0.78	-	4.82
J0926	241 ± 1	0.21 ± 0.03	17.6	10.4	9.10	8.05	0.69	-	3.93
J0938	213 ± 1	0.38 ± 0.02	16.1	11.2	9.40	8.19	0.67	-	2.43
J2103	496 ± 3	0.89 ± 0.03	43.1	41.4	10.90	8.70	0.46	-	3.13
J0021	307 ± 1	0.09 ± 0.01	18.6	14.9	9.30	8.19	0.53	-	2.35
J0823	197 ± 1	0.57 ± 0.02	9.4	9.6	8.60	8.23	0.34	-	1.20
J1025	187 ± 1	0.25 ± 0.03	12.2	7.6	9.20	8.11	0.61	-	2.92
J1112	309 ± 1	0.60 ± 0.03	24.8	28.7	10.20	8.52	0.33	-	3.03
J1113	179 ± 9	0.17 ± 0.16	1.2	7.1	9.60	8.35	1.09	-	3.83
J1144	171 ± 2	0.51 ± 0.04	7.1	8.9	9.90	8.40	0.76	-	2.93
J1414	-	-	6.3	5.1	8.50	8.28	0.63	-	1.99
J1416	257 ± 1	0.65 ± 0.03	19.9	23.4	10.00	8.47	0.19	-	2.86
J1428	214 ± 1	0.37 ± 0.03	19.8	13.9	9.60	8.31	0.71	-	3.95
J1429	300 ± 1	0.13 ± 0.03	36.0	26.8	9.40	8.12	0.29	-	3.81
J1521	258 ± 1	0.32 ± 0.03	6.0	5.8	9.50	8.27	0.37	-	2.26
J1525	213 ± 1	0.52 ± 0.03	6.3	9.1	9.40	8.46	0.51	-	1.86
J1612	290 ± 1	0.77 ± 0.03	32.2	36.1	10.00	8.51	0.31	-	3.36
Uncertainty	-	-	± 15%	-	-	± 0.14 dex	< 0.1 dex	< 0.1 dex	-

Notes. The typical uncertainties are estimated following Heckman et al. (2015). The uncertainties quoted for SFR_{IR} only account for that from the magnitude measurements of WISE.

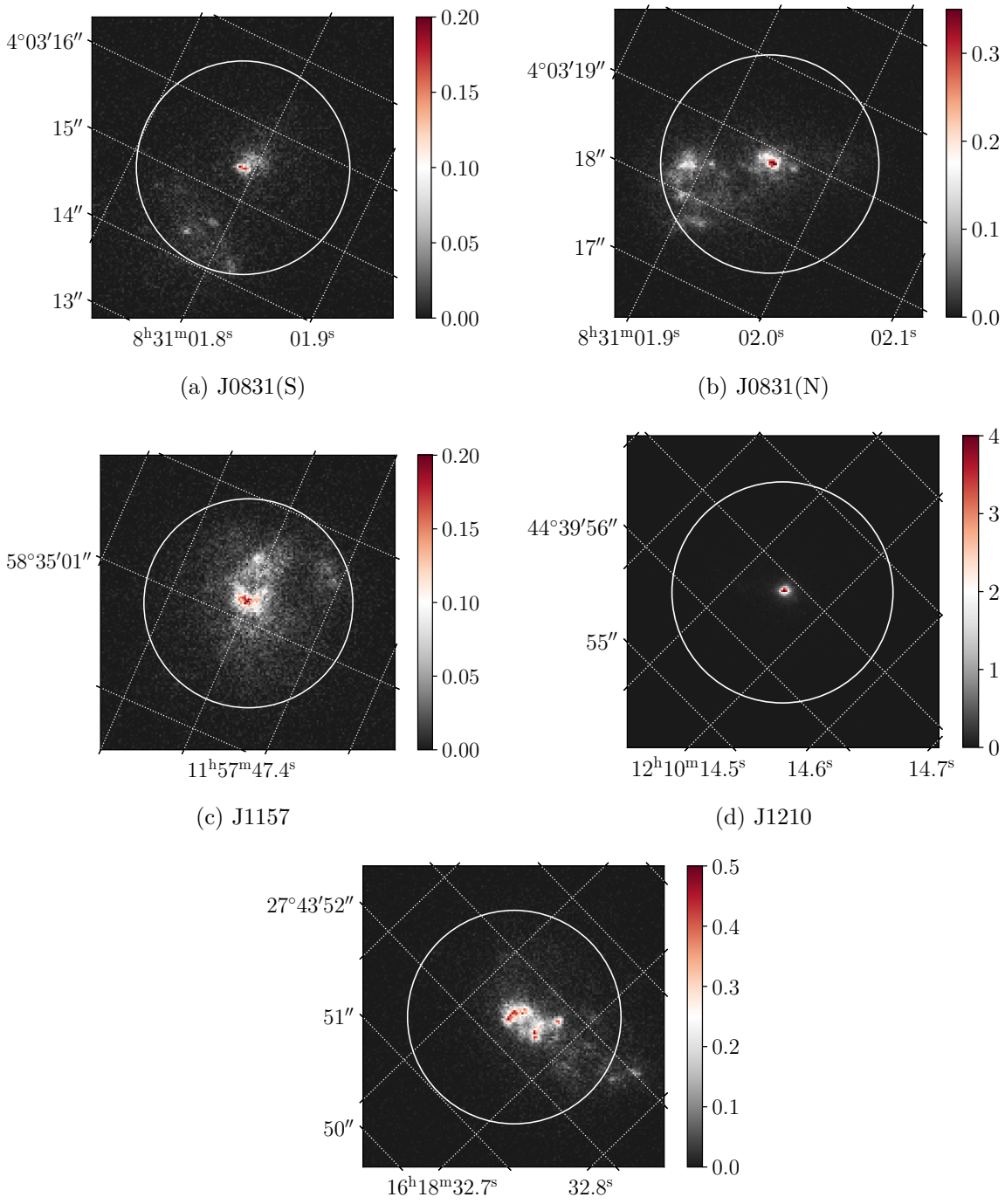

(a) J0831(S)

(b) J0831(N)

(c) J1157

(d) J1210

(e) J1618

Figure 4.4: COS NUV ACQ images. White circles indicate the COS aperture of radius 1.25″.

taken with the F343N filter, which maps the UV stellar continuum. We note that the half-light radii obtained in the UV continuum images are larger for J1210 and J1618. In the former case, diffuse light outside the field of view of the COS ACQ image is seen in the WFC3 image, while in the latter, extended faint light is detected by WFC3, due to its deeper imaging.

We use the FWHM of the Balmer emission lines in the SDSS to characterize the kinematics of the ionized interstellar medium in each galaxy. These widths have been corrected for the SDSS spectral resolution as part of the SDSS pipeline. Finally, the stellar masses are taken from the median of the corresponding probability density function in the MPA–JHU catalog.

4.3 Results

4.3.1 Spectra

In Figure 4.5, we show distributions of EW and FWHM of the fluorescence and resonance lines, as well as their ratios for the union of samples. They are estimated by applying Gaussian kernels on the data sets. Four features are evident. First, the emission lines are mostly centered at the systemic velocity of the galaxy, while the absorption lines are blue-shifted. Second, the fluorescence line widths more closely trace the Balmer emission-line widths. Third, the fluorescence emission lines are usually significantly weaker and narrower than the resonance absorption lines. Finally, there is much greater similarity between the widths and strengths of the Si II 1304, Si II* 1309 resonant, fluorescent pair than for the others. This is a significant clue, since the relatively small oscillator strength for the Si II 1304 line means that it will

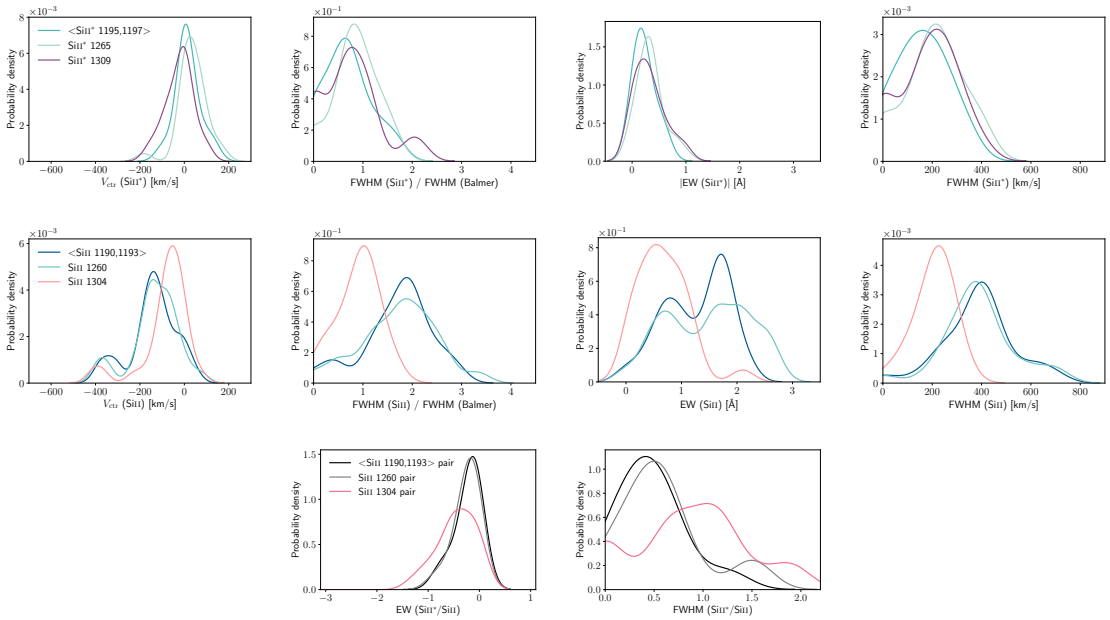

Figure 4.5: Kernel density estimates of the distributions of fluorescence lines (upper panel), resonance lines (middle panel), and ratios between the fluorescence and resonance lines (lower panel) for the union of samples considered in this paper. These results imply that a range of conditions is presented, spanning the majority of cases where the fluorescence emission lines are weak and narrow ("ISM-dominated") to a minority of cases where the emission and absorption lines have similar strengths and widths ("wind-dominated").

have correspondingly smaller optical depth (τ) at a given velocity than the other resonance lines (e.g., by a factor of $\sim$13 smaller than the Si II 1260 line).

Taken together, these results suggest that, in most cases, the fluorescence emission lines primarily trace the star-forming ionized ISM and/or the gas with the highest column densities and lowest outflow speeds.

However, we also note that there is a range in the relative strengths of the resonance absorption and fluorescence emission lines, even for the Si II 1260, Si II* 1265 pair (tracing gas with the greatest optical depths). To study any trends that may be manifested in our data, we use the Kendall τ test in assessing the statistical signifi-

cance between the ratios of emission/absorption line strength and other parameters. Those correlations, and their corresponding correlation coefficients τ_k and p-values, are shown on each of the scatter plots in Figure 4.6.

Most notable is the correlation between the ratio of fluorescence line EW to resonance line EW with the ratio of the FWHM of the two lines. A weaker correlation (but still significant) is present between the fluorescence to resonance line EW ratio and the fluorescence to Balmer line widths ratio. Both these correlations imply that we observe a range of conditions, spanning the majority of cases where the fluorescence emission lines are weak and narrow to a minority of cases in which the emission and absorption lines have similar strengths and widths.

4.3.2 Images

The five galaxies for which we have obtained images of the Fe II* fluorescence line emission are all members of the majority population of weak and narrow emission lines. In Figure 4.2, we see that the Fe II* emission in each case is concentrated within the star-bursting regions, which are characterized by high surface-brightness UV continuum and [O II] 3727 line emission.

To further quantify the consistency between the amount of Si II* emission present in the spectra and the amount of Fe II* emission in the images, we translate the photometric data of Fe II* to spectral fluxes via the following relation:

$$F(\mathrm{Fe\,II}) = \mathrm{F}_\lambda(\mathrm{Fe\,II}) \times \Delta\mathrm{W(F280N)}, \tag{4.1}$$

where F_λ is the sum of the flux density inside the aperture of the same size as the COS,

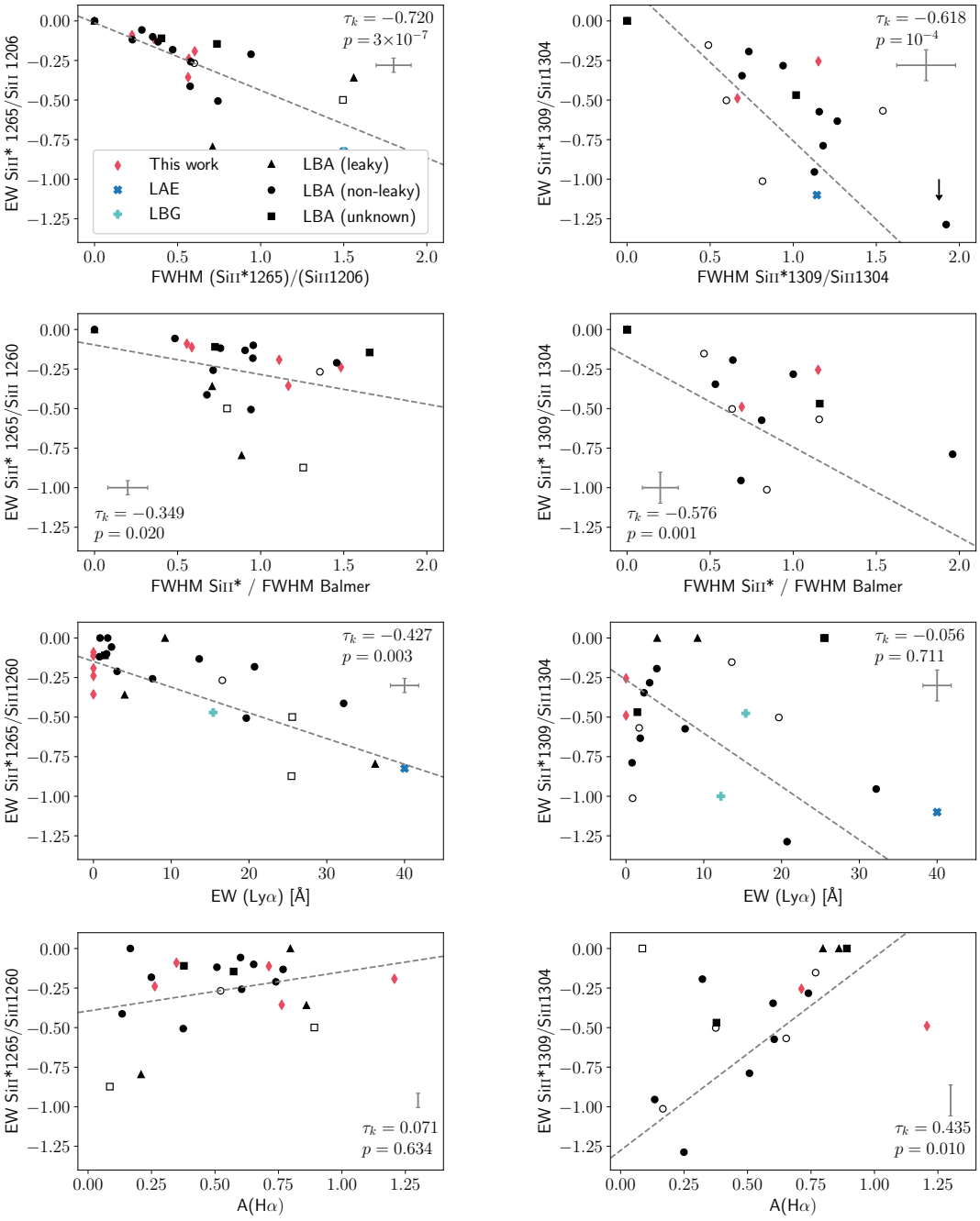

Figure 4.6: Scatter plots showing various correlations. Each statistical significance is indicated by Kendall's τ coefficient and p-value. An unfilled marker indicates that the measurement is likely to be affected by additional systematic errors due to a low signal-to-noise (S/N) spectrum or blended lines. The Si II 1190 pair is quantitatively the same as the Si II 1260 pair, and is hence omitted.

and ΔW is the width of the filter. We take $\Delta W(\mathrm{F280N}) = 42.52$Å from the WFC3 instrument handbook. A similar calculation is done to obtain the [O II] emission-line fluxes.

In Table 4.4 we summarize all the spectral and imaging measurements. Note that the uncertainties quoted for the Fe II* flux include only those from the background fluctuations. It is worth pointing out that Fe II* EW/λ is subjected to an additional systematic uncertainty induced during the process of estimating its continuum level via an interpolation between the SDSS and COS spectra.

Given that the associated resonance absorption lines will be optically thick, the repeated scattering reabsorption of resonance photons will eventually convert all the absorbed photons into fluorescence emission lines. In this case:

$$\begin{aligned} F(\mathrm{Fe\,II,\ tot}) &= \mathrm{EW}_{2587} F_{\lambda,\mathrm{cont}}(2587) + \\ &\quad \mathrm{EW}_{2600} F_{\lambda,\mathrm{cont}}(2600), \end{aligned} \tag{4.2a}$$

To estimate the EWs for these Fe II absorption lines, we assume that they have the same value of EW/λ as the Si II absorption lines measured with COS. More specifically, we use combinations of Si II line strengths that lead to the same mean oscillator strength f as the corresponding Fe II lines:

$$\frac{\mathrm{EW}_{2587}}{\lambda_{2587}} = \frac{1}{2}\left(\frac{\mathrm{EW}_{1304}}{\lambda_{1304}} + \frac{\mathrm{EW}_{1190}}{\lambda_{1190}}\right) \tag{4.2b}$$

$$\frac{\mathrm{EW}_{2600}}{\lambda_{2600}} = \frac{1}{2}\left(\frac{\mathrm{EW}_{1193}}{\lambda_{1193}} + \frac{\mathrm{EW}_{1190}}{\lambda_{1190}}\right). \tag{4.2c}$$

Table 4.4: Line Properties Inferred from WFC3 Imaging

	Fe II*	Fe II*	[O II]	Fe II*$_{\rm total}$[a]
	(10^{-16} erg cm^{-2} s^{-1} Å^{-1})	($10^{-4}\frac{\rm EW}{\lambda 2620}$)	(10^{-16} erg cm^{-2} s^{-1} Å^{-1})	(10^{-16} erg cm^{-2} s^{-1} Å^{-1})
J0831(S)	5.1 ± 7.5	6.1 ± 8.9	118 ± 9	20 ± 13
J0831(N)	19.0 ± 8.3	10.1 ± 4.4	224 ± 16	50 ± 28
J1157	23.0 ± 7.0	12.6 ± 3.9	168 ± 5	30 ± 16
J1210	31.4 ± 7.6	12.9 ± 3.1	157 ± 5	65 ± 36
J1618	31.1 ± 10.5	10.8 ± 3.7	203 ± 3	71 ± 40

Notes. The flux densities of Fe II* are measured in apertures the same size as the COS ($r = 1.25''$), and the uncertainties are the $1\,\sigma$ variances from many measurements on the blank sky using the same apertures.

[a] Fe II*$_{\rm total}$ is the expected total flux of Fe II* emission estimated from Si II* emission, as given in Equation 4.2.

Strictly speaking, Equation 4.2 applies to photon rates rather than fluxes, but we ignore this because the fluorescence and resonance photons have nearly the same energy.

While the uncertainties in the measured/estimated fluxes in Table 4.4 are substantial, we conclude that the amount of Fe II* emission is consistent with COS Si II* emission. This implies that a significant fraction of the weak and narrow fluorescence emission seen in the spectra can be ascribed to the emission associated with regions of intense star-formation seen in the images (consistent with an ISM-dominated origin).

4.4 Discussion

So far, we have presented a continuum of relative emission-line strengths and widths. In the majority of cases, the emission lines are much weaker and narrower than the

absorption lines. Direct imaging shows that the fluorescence emission in such cases is produced in regions with high surface brightness in the UV continuum and [O II] 3737 emission lines. These results indicate that, in these cases, the emission is "ISM-dominated" (i.e., the outflow makes little contribution). In other cases, the presence of stronger and broader emission lines suggest that the outflow is making a significant contribution. In this section, we discuss implications for wind structure based on both these empirical properties and a simple outflow model.

4.4.1 A Brief Primer

The use of the fluorescence emission lines as probes of the structure of galactic outflows has been discussed at length in a number of papers (Prochaska et al., 2011; Scarlata and Panagia, 2015; Zhu et al., 2015). Here, we want to simply summarize a few salient points that will be used below to interpret our data.

Concerning the resonance absorption lines, the profiles (line depth at a given velocity) are specified by the product of the column density of the relevant ion along the line-of-sight times the oscillator strength of a given transition times the covering factor (the fraction of the background continuum source covered by the foreground gas at a given velocity). It is important to note that the observed Si II resonance transition span a range of 13 in oscillator strength—and hence optical depth (see Table 4.1).

Once a resonance photon has been absorbed, the excited ion will decay radiatively into either the ground state (emission due to resonance scattering) or into the excited fine-structure level (emission due to fluorescence). The ratio of the number of photons initially produced in these two ways is given simply by the ratio of the respective

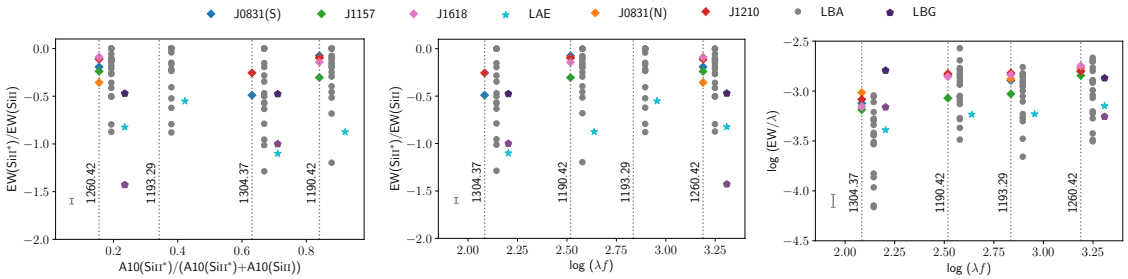

Figure 4.7: (a) EW ratios of fluorescence/resonance lines plotted against ratios of Einstein As. No correlation is shown. (b) EW ratios plotted as a function of oscillator strengths f. (c) Evolution of rest-frame EWs of Si II transitions plotted as a function of f. The characteristic transition from optically thin absorption (EW/$\lambda \propto f\lambda$) to optically thick absorption (flat) is evident except for J1157 (in green). Data from different samples are offset for clarity. Typical error bars are shown in gray.

Einstein As (see Table 4.1). The most and least effective reprocessing of absorbed resonance photons into fluorescence emission occurs for the Si II 1190, 1193 pair (84% efficiency) and the Si II 1260, 1265 pair (16% efficiency). This will be true in the limit where the resonance lines are optically thin (a single absorption occurs). If the resonance lines are optically think, then eventually (via multiple absorption events) all the absorbed photons are converted into fluorescence emission lines.

With that in mind, we show in Figure 4.7 the correlation between the oscillator strength and EW for four of the observed Si II transitions. From this, we see that the absorption lines are mainly optically thick for the Si II 1260, 1193, and 1190 transitions (they show the same EWs), but are starting to become optically thin for the Si II 1304 line.

It is even more instructive to compare the absorption-line profiles for different Si II transitions. To do so, we stack all the COS spectra of the LBAs and fit the resulting profiles' Gaussians. The results are shown in Figure 4.8 for the Si II 1260,

1527, and 1304 lines (in order of decreasing τ), with the lines becoming progressively narrower and less blue-shifted. This shows that the highest-velocity material has the lowest column density. Combining this with our previous result showing that the best agreement between the strengths and widths of the resonance and fluorescence lines was for the Si II 1304, 1309 pair (Figure 4.5) implies that the observed fluorescence emission lines are primarily tracing the highest-column-density gas (e.g., either a static ISM or the slower parts of the outflow).

Figure 4.7 also shows that the ratio of the strengths of the fluorescence emission lines and the resonance absorption lines does not depend on the reprocessing efficiency. This implies that the gas responsible for the observed fluorescence emission is optically thick for the associated resonance lines (meaning that all the absorbed photons there are being reprocessed into fluorescence emission lines). The fact these emission lines are usually much weaker (and narrower) than the absorption lines returns us to the question raised in the introduction to the paper—why are these emission lines usually so weak and narrow in the majority of the starbursts?

There are several processes/circumstances that could explain this: (1) outflows are confined to small solid angles ($\ll 4\pi$ sr); (2) the material producing the absorption is located at radii beyond those probed by the spectra; (3) the emission-line photons from the outflow are absorbed by dust in the outflow rather than escaping. The fact that outflows are seen in 100% of the galaxies we have observed is inconsistent with the first explanation, and so we do not consider it further. To test the other possibilities, and to gain more insight into the nature of the emission lines, we examine correlations between their properties and other potentially relevant parameters.

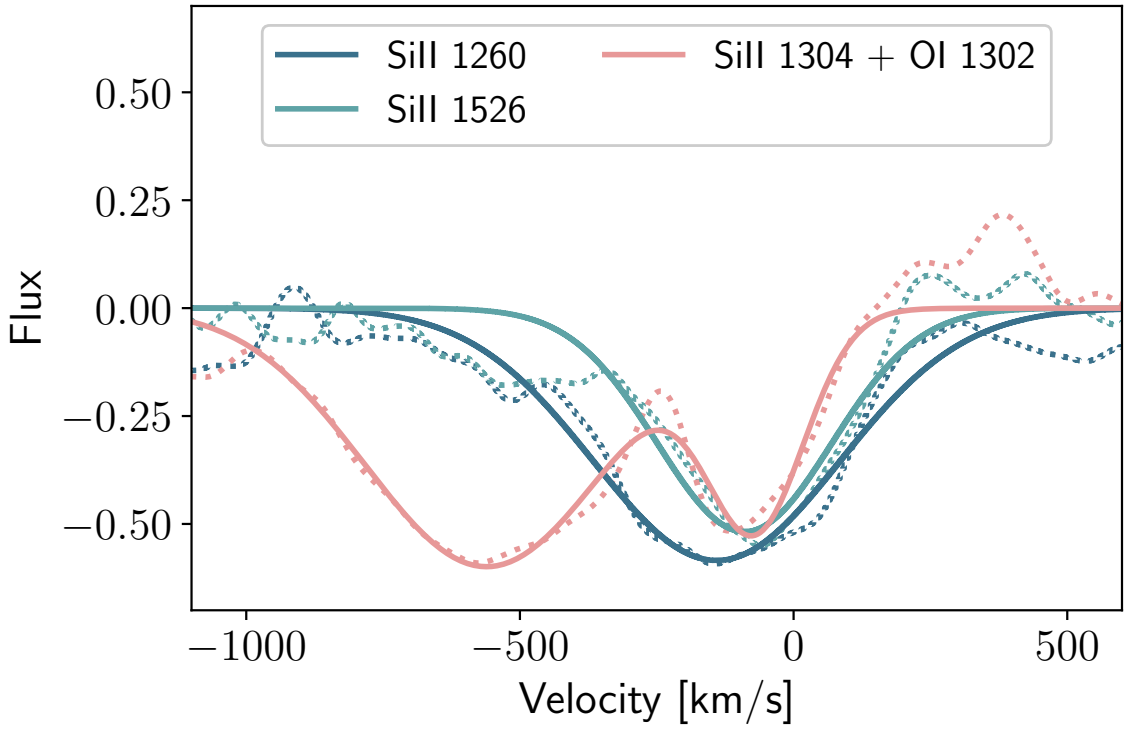

Figure 4.8: Comparison of the absorption-line profiles of Si II 1260, 1526, and 1304 from a stacked spectrum including all the LBAs. Dashed lines are the data, while the solid lines are the Gaussian fits. Note that the O I 1302 line is responsible for the strong and broad absorption feature seen centered around -600 km/s blueward of Si II 1304. Velocities on the x-axis are measured relative to the systemic velocity of the galaxy. The Si II 1260 (1304) line is the most (least) optically thick, showing that the highest-velocity outflowing gas has the lowest column density.

4.4.2 Correlations

Here, we examine correlations of properties of fluorescence and resonance absorption lines with properties of the galaxy and its starburst.

To begin, we can further test our inference of a continuum of properties, ranging from spectra in which the fluorescence lines are ISM-dominated (the majority) to more wind-dominated (the minority). We have argued that the key diagnostics are the ratios of both the EWs and line widths of the fluorescence emission lines and the resonance absorption lines. Indeed, Figure 4.6 shows that these two ratios are correlated for both the most and least optically thick transitions (Si II 1260 and 1304). We also see that, as the EW ratio increases, the ratio of the widths of the fluorescence emission lines and the Balmer emission lines (tracing the static ionized ISM) increases.

Perhaps most importantly, we find little correlation between relative strengths of the fluorescence emission lines and the resonance absorption lines with the projected size of the COS aperture (e.g., the ratio of radius of the COS aperture and the radius of the starburst measured in the NUV). In fact, Figure 4.9 reveals that, in most cases, the fluorescence lines remain weak even when the COS aperture is more than an order of magnitude larger than the starburst. We will explore the implications of this quantitatively in the next section.

As noted above, the weakness of the emission lines could be due in part to their absorption by dust that is located in the outflow. To test this, we show the correlations between the relative emission-line strengths and the amount of extinction (from the Balmer decrement in SDSS data). We see no correlation in the case of the Si II 1260, 1265 pair, but a significant correlation in the case of the Si II 1304, 1309 pair.

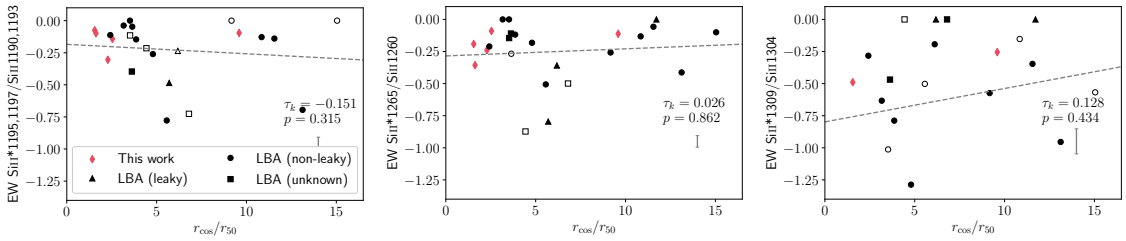

Figure 4.9: Relative strengths of the fluorescence emission lines and the resonance absorption lines plotted as functions of the projected size of the COS aperture. Typical error bars are shown on the right in gray. An unfilled marker indicates that the measurement is likely to be affected by additional systematic errors, due to a low S/N spectrum or blended lines. Little correlation is found.

Since the Si II 1260 transition is much more optically thick than Si II 1304 (requiring many more resonance scattering event to escape), and has such a low reprocessing efficiency (low likelihood of producing fluorescence emission), the lack of a correlation between the relative strengths of Si II* 1265 and Si II 1260 features with the Balmer decrement argues against dust absorption in the outflow as the cause of the weak emission. Regarding the Si II 1304, 1309 pair, we lean toward an explanation alluded to earlier: the Si II 1304 absorption line only traces gas that has high column density but low velocity, much of which is likely to be the static ISM. Therefore, this particular correlation is likely between the strength of absorption from this material and the amount of dust along the line of sight, as already seen in Heckman et al. (1998).

The strongest correlation is found between the fluorescence to resonance line EW ratio and the Lyα emission-line EW. This is driven mainly by the inverse correlation between the Lyα and resonant EWs (see Figure 4.10). This finding was also reported at high z in KLCS (Steidel et al., 2018). This correlation is intriguing because both large values of Lyα EW and weak low-ionization absorption lines have been empirically linked to the galaxies with significant amounts of escaping Lyman-continuum

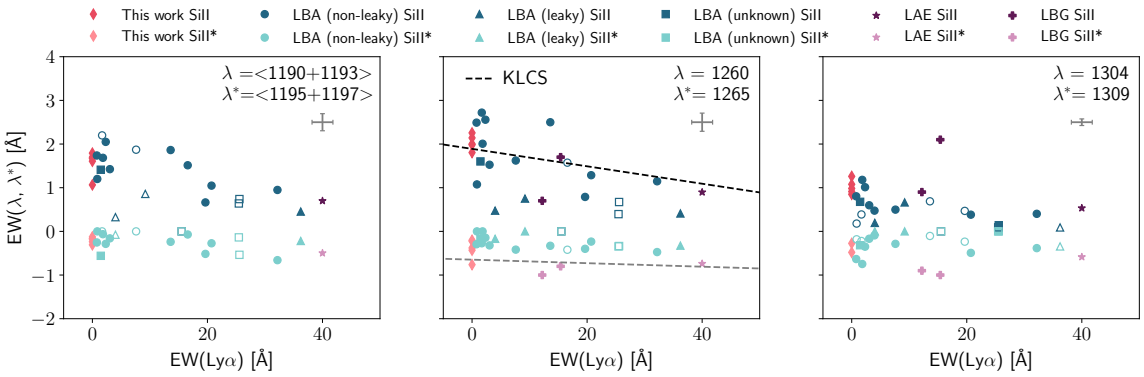

Figure 4.10: EWs of absorption and emission lines plotted as functions of $\mathrm{EW_{Ly\alpha}}$. Dashed lines in the middle panel are the best-fit relations from KLCS (Steidel et al., 2018). LAE data points are obtained from a stacked spectrum, of which $\mathrm{EW_{Ly\alpha}}$ is not measured, and so are placed along the x-axis for illustration purposes only. These plots suggest that the strongest correlation found, which is between EW(Si II*)/EW(Si II) and $\mathrm{EW_{Ly\alpha}}$ is driven mainly by the inverse correlation between the Lyα and resonant EWs.

(LyC) emission in $z \sim 3$ stacked samples (e.g., Marchi et al. 2018; Steidel et al. 2018) and among individual low-z LyC emitters (e.g., Verhamme et al. 2017; Chisholm et al. 2018; Wang et al. 2019). Taken together, the cases with the relatively strong fluorescence emission perhaps have clearer channels through which ionizing photons can escape the hosting galaxy (Heckman et al., 2015). However, a note of caution is due here, because we see no correlations between the relative strengths and widths of the emission lines and other proposed LyC leakage diagnostics, such as a significantly blue-shifted component in Lyα emission or [O III]/[O II] as discussed in Wang et al. (2019).

4.4.3 Implications for the Structure of Outflows

From the above discussion, we establish the cause for the weakness of the observed fluorescence emission being that most of the actual emission lies beyond the radii probed by the COS data ("slit loss"). We therefore conclude by considering the implications of this result for the structure of starburst-driven outflows. We begin with the subsample of our data that has the most constraining power: the group of galaxies observed with the largest apertures as compared to their observed sizes ($r_{\rm COS}/r_{50} \gtrsim 9$; see Figure 4.9).

To start, it is useful to remind ourselves that most of the fluorescence emission is expected to be generated within the "photosphere" of the outflow: the region where $\tau \gtrsim 1$ for the associated resonance line. The fact that the observed fluorescence emission lines are much weaker and narrower than the resonance absorption lines then implies that this photosphere is located at a greater distance from the starburst than what is captured in the COS aperture. This is quite plausible, as the projected radii of the COS apertures are typically two to four kpc (as shown in Table 4.3). In what follows, we use this idea to constrain the properties of the radial profile of the outflowing material responsible for the observed absorption lines.

We note that any fluorescence emission from the portion of the outflow captured by the COS aperture must be associated with material that is optically thin in the associated resonance line (otherwise the strength of the emission line should be similar to that of the absorption line). Taking then the case where $\tau \ll 1$ inside the region probed by COS, we can approximate the ratio between the observed flux of the

fluorescence emission, $F_{\rm fs}$, and that of the resonance absorption, $F_{\rm res}$, as

$$\frac{F_{\rm fs}}{F_{\rm res}} \simeq f_{\rm reproc}\tau, \tag{4.3}$$

where $f_{\rm reproc}$ is the fraction of the total absorbed photons that have been reprocessed into emission-line photons, and can be simply determined by the corresponding Einstein As:

$$f_{\rm reproc} = \frac{A_{\rm fs}}{A_{\rm fs} + A_{\rm res}}. \tag{4.4}$$

We focus on the Si II 1190/Si II* 1195 pair, where its numerical value is about 0.84. This means that by measuring $F_{\rm fs}/F_{\rm res}$, we effectively probe τ in the resonance line integrated from the starburst to the projected radius of the COS aperture.

For simplicity, we assume that the radial density, $n(r)$, follows a power law for the ion of interest:

$$n(r) \propto \left(\frac{r}{r_0}\right)^{-\alpha}, \tag{4.5}$$

where $\alpha > 0$ and r is the distance to the starburst. We assume this power law extends inward only as far as the starburst radius r_0 (i.e., the launch point for the outflow, which we effectively take to be r_{50}). The column density as a function of r, $N(r)$, is then simply given as

$$N(r) = \int_{r_0}^{r} n(r)\,{\rm d}r,\ r > r_0. \tag{4.6}$$

Since $\tau(r) \propto N(r)$, we can then relate $N(r)$ to our directly observable $F_{\rm fs}/F_{\rm res}$ such that we have

$$\frac{N(r_{\rm COS})}{N(\infty)} = \frac{\tau(r_{\rm COS})}{\tau(\infty)} \simeq \frac{F_{\rm fs}}{F_{\rm res}}. \tag{4.7}$$

As seen in Figure 4.9, we find $F_{\rm fs}/F_{\rm res} \lesssim 0.25$ even when $r_{\rm COS}/r_0 \gtrsim 9$. Equations

4.5–4.7 then imply that $\alpha \lesssim 1.13$.

More generally, we show the α-dependence of Equation 4.7 in Figure 4.11 for a range of $r_{\rm COS}/r_0$. Taking Equation 4.7, we can plot each galaxy in our sample in this figure. From this, we see those galaxies observed with smaller effective aperture sizes (even most of the "wind-dominated" cases), require $\alpha < 1.5$ (the only exception is the LBA J1428).

These results have some important implications. Let us adopt an outflow velocity that scales with radius as a power law:

$$v(r) \propto r^{-\beta}, \tag{4.8}$$

and adopt a mass-outflow rate that varies with radius as

$$\dot{M} \propto r^{\gamma}. \tag{4.9}$$

Then from

$$\dot{M} \propto n(r)\, v(r)\, r^2, \tag{4.10}$$

we arrive at the result that

$$\gamma = 2 - \alpha - \beta. \tag{4.11}$$

For the outflow to be mass-conserving ($\gamma = 0$), the requirement of $0 < \alpha < 1.5$ means the outflow must be strongly decelerating as it travels out ($2 > \beta > 0.5$). This would require that the fastest-moving material is closest to the starburst. This is inconsistent with the both the narrowness of the fluorescence emission lines observed within the COS aperture, and with direct observations of the nebular emission-line

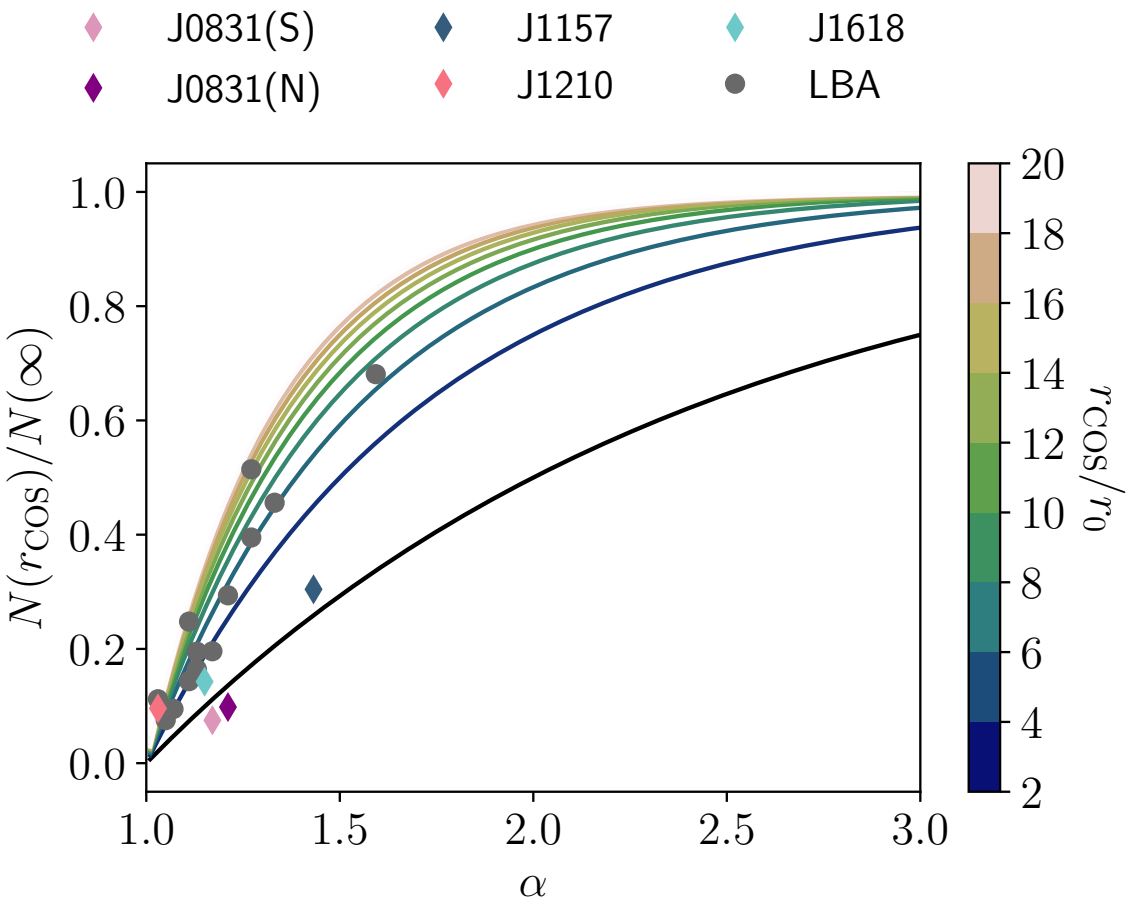

Figure 4.11: Ratio between the column density of absorbing material inside the radius probed by COS and the total column density (as inferred from the ratio of the fluxes in the fluorescence emission and that in resonance absorption) plotted as a function of the power-law index α of the radial density profile for the absorbing gas. Shades of color denote the ratio of the radius of the COS aperture ($r_{\rm COS}$) relative to the starburst radius r_0. We show the locations of the individual galaxies in our sample, and find that a shallow density profile ($\alpha < 1.5$) is required in nearly all cases.

gas in outflows (Heckman et al., 1990; Shopbell and Bland-Hawthorn, 1998).

As an example, for the simple case of a constant wind velocity ($\beta = 0$), $\alpha = 1.5$ yields $\dot{M} \propto r^{1/2}$. Thus, the wind would not be mass-conserving, and most of the outflowing material would be added at radii much larger than the starburst. Such a "mass-growing" scenario is consistent with several recent studies that have found that the gas producing the absorption lines may form *in situ* via radiative cooling instabilities in a much hotter wind fluid (Thompson et al., 2016; Schneider et al., 2018). The latter would be too hot to produce the observed absorption lines. In particular, Gronke and Oh (2018, 2020) have shown that absorbing clouds that exceed a critical size can not only survive destruction by the wind fluid, they enable new gas to condense out of the wind. This could increase the mass flux in absorbing gas with increasing radius through the depletion of the hot gas (i.e., the outflow as a whole could still be mass-conserving). Alternatively, models of wind-blown bubbles driven by starbursts (e.g., Lochhaas et al. 2018) imply an increasing mass in swept-up material with increasing radius (i.e., they are not mass-conserving).

Those new models are certainly encouraging, but more studies are needed to bridge the theoretical and observational fronts—e.g., simulations of mass growth in a full galactic context, as well as more sensitive imaging observations of emission from large-scale galactic outflows.

4.4.4 Implications for Deriving Outflow Rates

As emphasized in the introduction, one of the main motivations for better understanding the structure of the outflow of the absorbing material is to use this to improve estimates of the outflow rates as derived from the analysis of the absorption-line data.

A simple argument showing the importance of the size/structure of the outflow is as follows:

The mass-outflow rate is given by the outflowing mass divided by the outflow time. The latter is just the outflow size divided by the outflow velocity. What can be estimated from the absorption-line data is actually the total column density (N), which is essentially (half) the total mass divided by the cross-sectional area of the outflow. For a spherically symmetric outflow this implies that

$$\dot{M} \sim 4\pi N \mu v r, \tag{4.12}$$

where μ is the mean mass per particle and r is some kind of column-density weighted mean outflow radius. This is usually taken to be only a few times larger than the starburst radius r_0 (e.g., Heckman et al. 2000, 2015). Taken at face value, our results imply that the effective value for r is much larger than the starburst radius, and therefore the mass outflow rates will be correspondingly larger. More fundamentally, the outflow is unlikely to be mass-conserving, so there is no single well-defined value for $\dot{M}$.

Finally, we wish to emphasize a further complication. Galactic outflows are known to be multiphase, with hot, warm, and cold gas spanning about five orders of magnitude in temperature (Heckman and Thompson, 2017). Whatever information about mass-outflow rates is derived from the resonance absorption-line data will only pertain to the warm phase ($T \sim 10^4$–10^5 K).

4.5 Conclusions

We have reported on the analysis of HST imaging and spectroscopic data for a sample of low-z starburst galaxies, focusing on exploiting the diagnostic power of the UV emission lines that are created via fluorescent reprocessing of absorbed resonance-line photons in galactic outflows. Our principal conclusions are as follows:

1. We find that, in the majority of cases, the Si II* emission lines in the COS spectra have significantly smaller EWs than the associated resonance absorption lines, and are usually much narrower. The resonance absorption lines are strongly blue-shifted, tracing an outflow, while the emission lines are usually centered near the systemic velocity of the galaxy.

2. Direct imaging of the Fe II* emission in five of these galaxies shows that the emission arises in or near regions of intense star-formation (regions with high surface brightness in the UV continuum and the [O II] 3727 emission line).

3. By comparing the properties of the five different Si II resonance lines, which span a range of 13 in oscillator strength (optical depth), we find that the highest column density gas has the lowest outflow velocity. The weakest absorption line (Si II 1304) also most strongly resembles its associated fluorescence line (Si II* 1309) in terms of EW and FWHM.

4. These results all imply that, in the majority of cases, the observed fluorescence emission is associated with the static ISM and/or the slow-moving, most central region in the outflow.

5. We do, however, see a range in these properties, and find a good correlation between the ratio of the EWs of the fluorescence emission and resonance absorption lines and the ratio of their line widths. We interpret this as sequence from a majority of cases in which the fluorescence lines are "ISM-dominated" to a minority of cases in which the outflow contributes significantly.

6. The strongest correlation we see is between the ratio of the fluorescence and resonance EWs and the EW of the Lyα emission line. This is driven largely by an inverse correlation between the Lyα and Si II EWs. This is very similar to what is observed in high-z star-forming galaxies. Intriguingly, both strong Lyα emission and weak absorption from low ions like Si II have been empirically related to the escape of LyC radiation. This suggests a link between the outflow structure and LyC leakage.

7. We conclude that the relative weakness of fluorescence from the outflow (as traced by the absorption lines) means that the bulk of the wind emission arises on larger scales than what is probed by the COS aperture. We use a simple model to show that the radial falloff in the outflow density cannot be significantly steeper than $r^{-\alpha}$, where $\alpha \sim 1$–1.5.

8. Unless the outflow is rapidly decelerating with radius (which is inconsistent with other observations of outflows), the shallow radial density profile implies that the mass flux in the outflowing absorbing material increases with radius. This is consistent with some recent models in which either relatively cool absorbing gas condenses out of a hotter wind fluid at large radii, or in which the wind fluid sweeps up more and more ambient cool gas as it travels outward.

9. These results imply that existing estimates of the outflow rates in starbursts are unlikely to be accurate, may systematically underestimate the true values, and do not capture any radial dependence in the rates.

We thank Max Gronke and Claudia Scarlata for valuable input to the paper. We also thank Claudia Scarlata for sharing the stacked spectrum of LAEs. B.W. thanks Caroline Huang, David Thilker, and Wenlong Yuan for helpful discussions on data analysis. This work is supported by *HST*-GO-15340, provided by NASA through a grant from the Space Telescope Science Institute, which is operated by the Association of Universities for Research in Astronomy, Inc., under NASA contract NAS5-26555. This publication made use of data products from the Wide-field Infrared Survey Explorer, which is a joint project of the University of California, Los Angeles, and the Jet Propulsion Laboratory/California Institute of Technology, funded by NASA; the NASA/IPAC Extragalactic Database, which is operated by the Jet Propulsion Laboratory, California Institute of Technology, under contract with NASA; and the NASA Astrophysical Data System for bibliographic information. This project also made use of SDSS data. Funding for the Sloan Digital Sky Survey IV has been provided by the Alfred P. Sloan Foundation, the U.S. Department of Energy Office of Science, and the Participating Institutions. SDSS-IV acknowledges support and resources from the Center for High-Performance Computing at the University of Utah. The SDSS web site is www.sdss.org. SDSS-IV is managed by the Astrophysical Research Consortium for the Participating Institutions of the SDSS Collaboration including the Brazilian Participation Group, the Carnegie Institution for Science, Carnegie Mellon University, the Chilean Participation Group, the French Participation Group, Harvard-Smithsonian Center for Astrophysics, Instituto de Astrofísica de Canarias,

The Johns Hopkins University, Kavli Institute for the Physics and Mathematics of the Universe (IPMU) / University of Tokyo, the Korean Participation Group, Lawrence Berkeley National Laboratory, Leibniz Institut für Astrophysik Potsdam (AIP), Max-Planck-Institut für Astronomie (MPIA Heidelberg), Max-Planck-Institut für Astrophysik (MPA Garching), Max-Planck-Institut für Extraterrestrische Physik (MPE), National Astronomical Observatories of China, New Mexico State University, New York University, University of Notre Dame, Observatário Nacional / MCTI, The Ohio State University, Pennsylvania State University, Shanghai Astronomical Observatory, United Kingdom Participation Group, Universidad Nacional Autónoma de México, University of Arizona, University of Colorado Boulder, University of Oxford, University of Portsmouth, University of Utah, University of Virginia, University of Washington, University of Wisconsin, Vanderbilt University, and Yale University.

Appendix

Additional spectra are shown in Figure 4.12; measured Si II and Si II* line profiles of the five galaxies of this paper and LBAs are listed in Table 4.5 and 4.6 respectively.

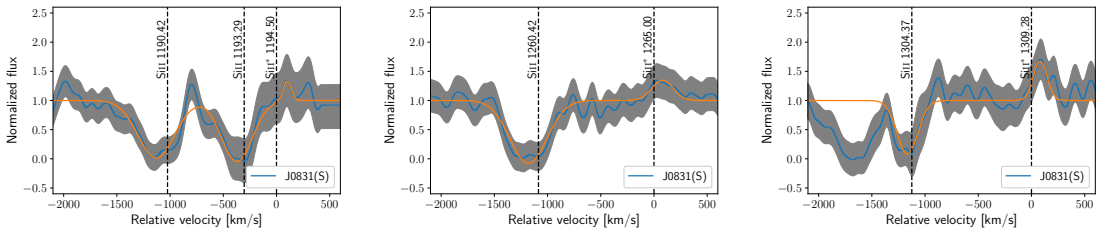

(a) J0831(S)

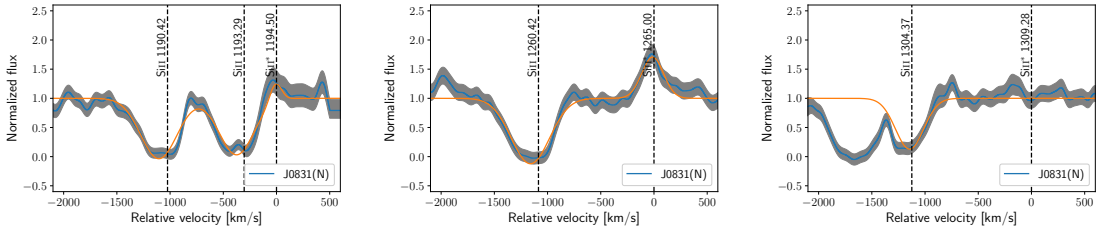

(b) J0831(N)

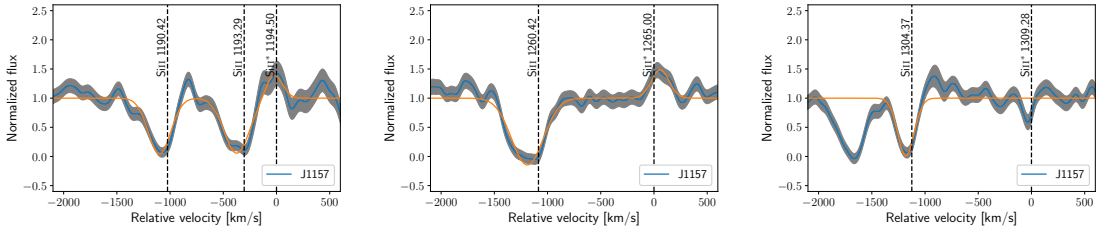

(c) J1157

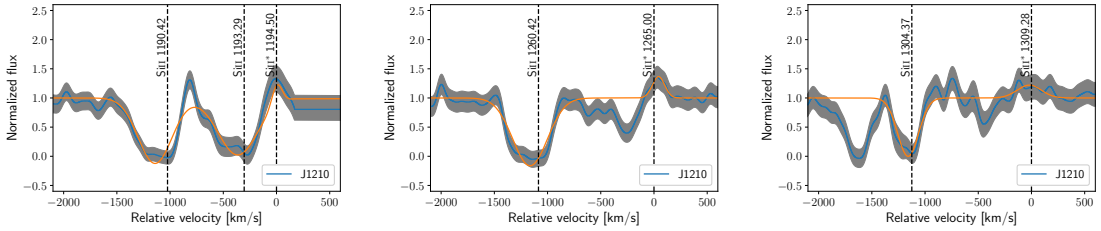

(d) J1210

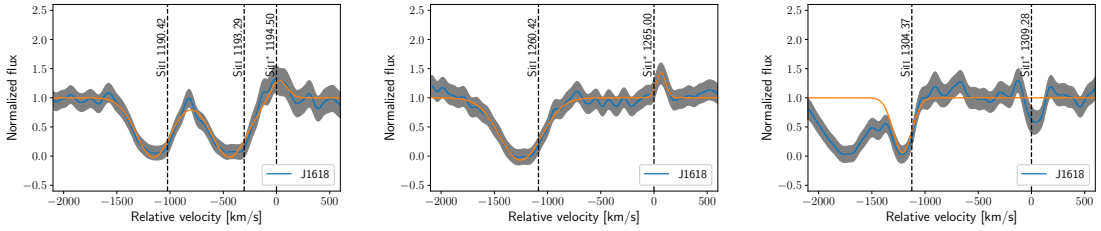

(e) J1618

Figure 4.12: Continuum-normalized spectra with the stellar features removed, zooming in on lines of interest. Overplotted in orange are the Gaussian fits.

Table 4.5: Measured Spectral Line Properties

	Line	$V_{\rm ctr}$ (km/s)	EW (Å)	FWHM (km/s)	FW90[a] (km/s)
J0831(S)					
	Si II 1193	-60	1.8	439	796
	Si II* 1195	4	-0.2	115	204
	Si II* 1197[b]	-	-	-	-
	Si II 1260	-80	2.0	385	701
	Si II* 1265	43	-0.2	137	248
	Si II 1304	-35	1.1	234	423
	Si II* 1309	-22	-0.3	270	490
J1618					
	Si II 1190	-133	1.7	387	703
	Si II 1193	-138	1.7	402	736
	Si II* 1195	21	-0.2	176	322
	Si II* 1197[b]	-	-	-	-
	Si II 1260	-168	2.3	472	862
	Si II* 1265	66	-0.2	107	193
	Si II 1304	-87	0.9	209	379
	Si II* 1309[c]	-	-	-	-

Notes. All measurements can be assumed to have errors on the order of 10%–15% dominated by systematics in the polynomial fit to the continuum and subtraction of the SB99 models.

[a] FW90: FW at 90% continuum.

[b] Line falls on the detector gap.

[c] Line is likely contaminated by the MW absorption Si IV 1402.8.

Table 4.6: Measured Spectral Line Properties of LBAs

	Line	$V_{\rm ctr}$ (km/s)	EW (Å)	FWHM (km/s)	FW90[a] (km/s)
J0055					
	Si II 1190	-145	2.0	477	868
	Si II 1193	-110	2.1	457	834
	Si II* 1195	59	-0.2	266	484
	Si II* 1197	-32	-0.3	271	496
	Si II 1260	-169	2.6	576	1047
	Si II* 1265	6	-0.1	164	298
	Si II 1304	-59	1.0	260	472
	Si II* 1309	41	-0.4	180	331
J0150					
	Si II 1190	-131	1.4	368	670
	Si II 1193	-98	1.5	433	789
	Si II* 1195	0	0.0	0	0
	Si II* 1197	55	-0.3	233	422
	Si II 1260	-139	1.5	371	670
	Si II* 1265	151	-0.3	349	633
	Si II 1304	-85	0.6	255	466
	Si II* 1309	96	-0.2	240	435
J0921					
	Si II 1190	42	0.4	152	277
	Si II 1193	48	0.3	142	261
	Si II* 1195	142	-0.2	191	351
	Si II* 1197	0	0.0	0	0

(To be continued)

Galaxy	Line	$V_{\rm ctr}$ (km/s)	EW (Å)	FWHM (km/s)	FW90[a] (km/s)
	Si II 1260	73	0.5	179	330
	Si II* 1265	84	-0.2	279	509
	Si II 1304	67	0.2	84	148
	Si II* 1309	0	0.0	0	0
J0926					
	Si II 1190	-329	0.5	402	733
	Si II 1193	-282	0.4	286	522
	Si II* 1195	-20	-0.2	161	292
	Si II* 1197	-18	-0.2	142	258
	Si II 1260	-371	0.4	301	547
	Si II* 1265	4	-0.3	214	388
	Si II 1304	-100	0.1	124	224
	Si II* 1309	-11	-0.3	233	425
J0938					
	Si II 1190	-52	1.4	410	745
	Si II 1193	2	1.4	434	788
	Si II* 1195	70	-0.2	150	277
	Si II* 1197	-49	-0.9	566	1028
	Si II 1260	-3	1.6	383	697
	Si II* 1265	58	-0.2	154	283
	Si II 1304	-1	0.7	242	444
	Si II* 1309	-11	-0.3	247	448
J2103					
	Si II 1190	-337	0.9	303	552

(To be continued)

Galaxy	Line	$V_{\rm ctr}$ (km/s)	EW (Å)	FWHM (km/s)	FW90[a] (km/s)
	Si II 1193	-299	0.6	185	337
	Si II* 1195	-46	-0.6	189	343
	Si II* 1197	-119	-0.5	369	672
	Si II 1260	-168	0.7	265	481
	Si II* 1265	83	-0.3	396	720
	Si II 1304	-74	0.1	104	191
	Si II* 1309	0	0.0	0	0
J0021					
	Si II 1190	-212	0.6	410	746
	Si II 1193	-212	0.6	410	746
	Si II* 1195	115	-0.1	162	296
	Si II* 1197	-49	-0.2	311	568
	Si II 1260	-227	0.4	265	483
	Si II* 1265	19	-0.3	385	701
	Si II 1304	-95	0.1	105	187
	Si II* 1309	0	0.0	0	0
J0823					
	Si II 1190	-38	1.6	378	690
	Si II 1193	8	1.8	413	753
	Si II* 1195	126	-0.3	212	389
	Si II* 1197	124	-0.1	90	167
	Si II 1260	-64	2.2	443	808
	Si II* 1265	165	-0.3	327	593
	Si II 1304	16	1.1	232	396

(To be continued)

Galaxy	Line	$V_{\rm ctr}$ (km/s)	EW (Å)	FWHM (km/s)	FW90[a] (km/s)
	Si II* 1309	-	-	-	-
J1025					
	Si II 1190	-147	1.0	332	608
	Si II 1193	-147	1.1	371	674
	Si II* 1195	60	-0.3	184	338
	Si II* 1197	-35	-0.2	246	450
	Si II 1260	-139	1.3	379	690
	Si II* 1265	18	-0.2	178	323
	Si II 1304	-130	0.4	207	377
	Si II* 1309	10	-0.5	398	727
J1112					
	Si II 1190	-94	2.4	657	1194
	Si II 1193	-175	1.3	409	748
	Si II* 1195	0	0.0	0	0
	Si II* 1197	0	0.0	0	0
	Si II 1260	-151	1.6	381	696
	Si II* 1265	43	-0.4	221	407
	Si II 1304	-71	0.5	216	393
	Si II* 1309	-43	-0.3	250	458
J1113					
	Si II 1190	-236	1.0	363	662
	Si II 1193	-118	1.4	482	876
	Si II* 1195	0	0.0	0	0
	Si II* 1197	0	0.0	0	0

(To be continued)

Galaxy	Line	$V_{\rm ctr}$ (km/s)	EW (Å)	FWHM (km/s)	FW90[a] (km/s)
	Si II 1260	-84	1.1	354	647
	Si II* 1265	0	0.0	0	0
	Si II 1304	-39	0.2	184	338
	Si II* 1309	-133	-0.2	150	274
J1144					
	Si II 1190	-196	1.8	439	798
	Si II 1193	-181	1.7	427	778
	Si II* 1195	4	-0.3	186	340
	Si II* 1197	-61	-0.3	210	385
	Si II 1260	-151	2.5	570	1042
	Si II* 1265	41	-0.3	130	239
	Si II 1304	-158	0.8	285	517
	Si II* 1309	-88	-0.6	336	610
J1414					
	Si II 1190	-78	1.7	389	712
	Si II 1193	-65	1.7	433	789
	Si II* 1195	19	-0.1	159	289
	Si II* 1197	0	0.0	0	0
	Si II 1260	-62	2.0	383	699
	Si II* 1265	0	0.0	0	0
	Si II 1304	-14	1.2	260	476
	Si II* 1309	12	-0.7	329	596
J1416					
	Si II 1190	-39	3.2	968	1768

(To be continued)

Galaxy	Line	$V_{\rm ctr}$ (km/s)	EW (Å)	FWHM (km/s)	FW90[a] (km/s)
	Si II 1193	33	1.2	426	778
	Si II* 1195	0	0.0	0	0
	Si II* 1197	0	0.0	0	0
	Si II 1260	-49	2.7	701	1279
	Si II* 1265	61	-0.3	245	447
	Si II 1304	-36	0.4	193	351
	Si II* 1309	-49	-0.2	297	542
J1428					
	Si II 1190	-181	0.6	227	416
	Si II 1193	-152	0.7	273	496
	Si II* 1195	167	-0.7	485	881
	Si II* 1197	-41	-0.3	184	334
	Si II 1260	-152	0.8	271	495
	Si II* 1265	1	-0.4	201	366
	Si II 1304	-411	0.5	226	412
	Si II* 1309	-79	-0.2	135	249
J1429					
	Si II 1190	-179	1.0	319	580
	Si II 1193	-147	0.9	316	574
	Si II* 1195	2	-0.5	171	313
	Si II* 1197	38	-0.8	251	455
	Si II 1260	-139	1.1	352	640
	Si II* 1265	30	-0.5	203	368
	Si II 1304	-100	0.4	182	336

(To be continued)

Galaxy	Line	$V_{\rm ctr}$ (km/s)	EW (Å)	FWHM (km/s)	FW90[a] (km/s)
	Si II* 1309	16	-0.4	205	373
J1521					
	Si II 1190	-	-	-	-
	Si II 1193	-	-	-	-
	Si II* 1195	-	-	-	-
	Si II* 1197	0	0.0	0	0
	Si II 1260	-	-	-	-
	Si II* 1265	-	-	-	-
	Si II 1304	-69	0.5	224	404
	Si II* 1309	-86	-0.1	164	302
J1525					
	Si II 1190	-375	1.5	471	860
	Si II 1193	-358	1.5	498	905
	Si II* 1195	1	-0.1	121	221
	Si II* 1197	0	0.0	0	0
	Si II 1260	-343	1.6	482	879
	Si II* 1265	102	-0.4	290	529
	Si II 1304	-	-	-	-
	Si II* 1309	-	-	-	-
J1612					
	Si II 1190	-410	1.9	636	1160
	Si II 1193	-354	1.8	573	1044
	Si II* 1195	270	-0.5	459	836
	Si II* 1197	0	0.0	0	0

(To be continued)

Galaxy	Line	$V_{\rm ctr}$ (km/s)	EW (Å)	FWHM (km/s)	FW90[a] (km/s)
	Si II 1260	-395	2.5	687	1249
	Si II* 1265	3	-0.3	263	480
	Si II 1304	-369	0.7	274	504
	Si II* 1309	-70	-0.1	134	246

Notes. "–" indicates that data is not valid due to MW absorption or detector gap. All measurements can be assumed to have errors on the order of 10%–15% dominated by systematics in the polynomial fit to the continuum and subtraction of the SB99 models.

Chapter 5

Concluding Remarks

This dissertation presents two new methods to probe the interstellar and the circumgalactic environments of galaxies, and connects them to the cosmic reionization. In this concluding chapter, we summarize the current status and the future prospective.

5.1 The Search for Ionizing Sources

Progress on understanding how galaxies reionized the universe has continuously been made with the HST on the low- and high-redshift fronts. The work presented in Chapters 2–3 is among the various efforts to identify analogs to EoR galaxies at $z \sim 0.3$. We find that [S II] deficiency is a robust indicator for LyC leakage using data from a pilot program (HST-GO-15341) and LzLCS. This new diagnostic thus expands the parameter space in which investigations of how galaxies could maintain reionization can be carried out. Interestingly, we discover that [S II] deficiency can select LCEs that are more massive than the LyC-emitting Green Pea galaxies at similar redshift. Therefore it provides laboratories for examining the non-conventional scenario where

massive galaxies dominate the reionization process (Naidu et al., 2020). In addition, the added diversity to the population of LCEs has led to new interpretations on their physical models (Cen, 2020; Katz et al., 2020; Ramambason et al., 2020).

Considering the other efforts in studying low-z LCEs, such as utilizing rest-frame UV absorption lines (Chisholm et al., 2018), Mg II emission (Henry et al., 2018), and [O III]/[O II] flux ratio (Izotov et al., 2021), the sample size of local EoR analogs promises to increase. It is expected that our knowledge on the conditions that enable LyC escape will be improved in the near future.

On the high-z side, there are breakthroughs on the search of LCEs at $z \sim 3$ (Steidel et al., 2018; Fletcher et al., 2019) as well as on constraints of $\rho_{\rm UV}$ and $\xi_{\rm ion}$ mostly due to the Hubble Ultra Deep Field (Beckwith et al., 2006) and the Hubble Frontier Fields (Lotz et al., 2017; Ishigaki et al., 2018). With the launch of the JWST in sight, we expect tighter constraints on all three parameters in Equation 1.8. Ultradeep infrared imaging with the JWST is posited to reveal the UV luminosity function at luminosities below $M_{\rm UV} = -17$. Spectroscopic investigations of $z > 6$ galaxies promise improved constraints on $\xi_{\rm ion}$. Determining $f_{\rm esc}$ at $z > 6$ would still be challenging. However, it is possible to confirm LyC leakage in $z \sim 3$ galaxies directly and study the redshift evolution of various LyC predictors to extrapolate to higher redshifts. In addition, JWST may be able to identify $z > 7$ galaxies with significant LyC leakage through the comparison of Hβ and UV continuum star-formation rates.

5.2 Feedback in Galaxy Formation

Theory of galactic formation and evolution in the cosmological context is well established (Springel et al., 2005; Vogelsberger et al., 2020). What remains elusive is a robust understanding of the interplay among various physical processes such as stellar formation and feedback, which operates at scales below the resolution of any cosmological simulation. Both hydrodynamic simulations and semi-analytic models often rely on simple theoretical arguments and/or empirical relations to include feedback processes (Somerville and Davé, 2015).

An important feedback mechanism is known to be galactic wind associated with star formation (Veilleux et al., 2005; Heckman and Thompson, 2017; Veilleux et al., 2020). In Chapter 4, we probe the degree of influence of outflows via UV emission lines. We argue that outflowing materials likely are added at a distance greater than the commonly assumed value of a few times the radius of the starburst based on an order-of-magnitude calculation. Taking a step further, we intend to systematically explore a grid of outflow models which are simulated with a modified version of the public radiative transfer code RASCAS (Michel-Dansac et al., 2020). The results will put tighter constraints on the gas kinematics and morphology, improving our estimates of mass outflow rates and our understanding of the origin of the outflowing gas.

More broadly speaking, various kinds of models on galaxy formation have seen progress with increasing physical precision; for example, a full accounting of energy and momentum from stellar feedback in zoom-in simulations (Hopkins et al., 2013; Agertz and Kravtsov, 2016), and unified multiwavelength semi-analytical mod-

els (Lacey et al., 2016). Ultimately, the goal is to eliminate the need for empirically tuning parameters, but instead to create models that are motivated by our physical understanding of the detailed processes involved in feedback from stars and supermassive black holes.

Ideally, we would like to obtain more direct observations to be compared with simulations. There are several important observational developments that are taking place now, or are on the horizon. To name a few, submillimeter and radio interferometers, including the Atacama Large Millimeter/Submillimeter Array and the Square Kilometer Array, can characterize the cold gas in the ISM of galaxies out to high redshift. Integral field unit spectrographs on the JWST will lead to improved characterizations of stellar and AGN-driven winds. Combining with observations from ground-based telescopes, large samples of nearby and distant galaxies will be available for examining parameters of spatially resolved stellar population and kinematics.

We thus live in interesting times in which the interplay between state-of-the-art models and telescopes is advancing our understanding of the cosmic history. Explicit predictions are being made by theorists, while data covering greater spatial and temporal dimensions are being, or soon to be, delivered by multiple facilities. It is almost certain that there will be surprises forthcoming and discrepancies needed to be resolved. Hence there is much work to be done for the exciting journey ahead.

Bibliography

Agertz, O. and Kravtsov, A. V.: 2016, *ApJ* **824(2)**, 79

Alexandroff, R. M., Heckman, T. M., Borthakur, S., Overzier, R., and Leitherer, C.: 2015, *ApJ* **810(2)**, 104

Armus, L., Heckman, T. M., and Miley, G. K.: 1990, *ApJ* **364**, 471

Baldwin, J. A., Phillips, M. M., and Terlevich, R.: 1981, *PASP* **93**, 5

Barkana, R. and Loeb, A.: 2001, *Phys Rep* **349**, 125

Beckwith, S. V. W., Stiavelli, M., Koekemoer, A. M., Caldwell, J. A. R., Ferguson, H. C., Hook, R., Lucas, R. A., Bergeron, L. E., Corbin, M., Jogee, S., Panagia, N., Robberto, M., Royle, P., Somerville, R. S., and Sosey, M.: 2006, *AJ* **132(5)**, 1729

Bennett, C. L., Larson, D., Weiland, J. L., Jarosik, N., Hinshaw, G., Odegard, N., Smith, K. M., Hill, R. S., Gold, B., Halpern, M., Komatsu, E., Nolta, M. R., Page, L., Spergel, D. N., Wollack, E., Dunkley, J., Kogut, A., Limon, M., Meyer, S. S., Tucker, G. S., and Wright, E. L.: 2013, *ApJS* **208**, 20

Bergvall, N., Zackrisson, E., Andersson, B. G., Arnberg, D., Masegosa, J., and Östlin, G.: 2006, *A&A* **448(2)**, 513

Borthakur, S., Heckman, T. M., Leitherer, C., and Overzier, R. A.: 2014, *Science* **346(6206)**, 216

Bouwens, R. J., Illingworth, G. D., Oesch, P. A., Caruana, J., Holwerda, B., Smit, R., and Wilkins, S.: 2015, *ApJ* **811(2)**, 140

Bouwens, R. J., Oesch, P. A., Stefanon, M., Illingworth, G., Labbé, I., Reddy, N., Atek, H., Montes, M., Naidu, R., Nanayakkara, T., Nelson, E., and Wilkins, S.: 2021, *AJ* **162(2)**, 47

Bouwens, R. J., Smit, R., Labbé, I., Franx, M., Caruana, J., Oesch, P., Stefanon, M., and Rasappu, N.: 2016, *ApJ* **831(2)**, 176

Bruzual, G. and Charlot, S.: 2003, *MNRAS* **344(4)**, 1000

Bryan, G. L. and Norman, M. L.: 1998, *ApJ* **495(1)**, 80

Calzetti, D.: 2011, in J. Falcon-Barroso and J. H. Knapen (eds.), *Secul. Evol. Galaxies*, pp 419–458, Cambridge University Press, Cambridge

Calzetti, D., Armus, L., Bohlin, R. C., Kinney, A. L., Koornneef, J., and Storchi-Bergmann, T.: 1999, *ApJ* **533**, 682

Cen, R.: 2020, *ApJL* **889(1)**, L22

Cen, R. and Kimm, T.: 2015, *ApJL* **801(2)**, L25

Charlot, S. and Fall, S. M.: 2000, *ApJ* **539(2)**, 718

Chisholm, J., Gazagnes, S., Schaerer, D., Verhamme, A., Rigby, J. R., Bayliss, M., Sharon, K., Gladders, M., and Dahle, H.: 2018, *A&A* **616**, A30

Chisholm, J., Prochaska, J. X., Schaerer, D., Gazagnes, S., and Henry, A.: 2020, *MNRAS* **498(2)**, 2554

Chisholm, J., Rigby, J. R., Bayliss, M., Berg, D. A., Dahle, H., Gladders, M., and Sharon, K.: 2019, *ApJ* **882(2)**, 182

Chisholm, J., Tremonti, C. A., Leitherer, C., and Chen, Y.: 2017, *MNRAS* **469(4)**, 4831

Choi, Y., Dalcanton, J. J., Williams, B. F., Skillman, E. D., Fouesneau, M., Gordon, K. D., Sandstrom, K. M., Weisz, D. R., and Gilbert, K. M.: 2020, *ApJ* **902(1)**, 54

Dunlop, J. S., Rogers, A. B., McLure, R. J., Ellis, R. S., Robertson, B. E., Koekemoer, A., Dayal, P., Curtis-Lake, E., Wild, V., Charlot, S., Bowler, R. A. A., Schenker, M. A., Ouchi, M., Ono, Y., Cirasuolo, M., Furlanetto, S. R., Stark, D. P., Targett, T. A., and Schneider, E.: 2013, *MNRAS* **432(4)**, 3520

Ellis, R. S., McLure, R. J., Dunlop, J. S., Robertson, B. E., Ono, Y., Schenker, M. A., Koekemoer, A., Bowler, R. A. A., Ouchi, M., Rogers, A. B., Curtis-Lake, E., Schneider, E., Charlot, S., Stark, D. P., Furlanetto, S. R., and Cirasuolo, M.: 2013, *ApJL* **763(1)**, L7

Erb, D. K., Quider, A. M., Henry, A. L., and Martin, C. L.: 2012, *ApJ* **759(1)**, 26

Fan, X., Carilli, C., and Keating, B.: 2006, *ARA&A* **44(1)**, 415

Fan, X., Strauss, M. A., Becker, R. H., White, R. L., Gunn, J. E., Knapp, G. R., Richards, G. T., Schneider, D. P., Brinkmann, J., and Fukugita, M.: 2006, *AJ* **132**, 117

Finkelstein, S. L., Ryan, Russell E., J., Papovich, C., Dickinson, M., Song, M., Somerville, R. S., Ferguson, H. C., Salmon, B., Giavalisco, M., Koekemoer, A. M., Ashby, M. L. N., Behroozi, P., Castellano, M., Dunlop, J. S., Faber, S. M., Fazio, G. G., Fontana, A., Grogin, N. A., Hathi, N., Jaacks, J., Kocevski, D. D., Livermore, R., McLure, R. J., Merlin, E., Mobasher, B., Newman, J. A., Rafelski, M., Tilvi, V., and Willner, S. P.: 2015, *ApJ* **810(1)**, 71

Finley, H., Bouché, N., Contini, T., Epinat, B., Bacon, R., Brinchmann, J., Cantalupo, S., Erroz-Ferrer, S., Marino, R. A., Maseda, M., Richard, J., Schroetter, I., Verhamme, A., Weilbacher, P. M., Wendt, M., and Wisotzki, L.: 2017, *A&A* **605**, A118

Finley, H., Bouché, N., Contini, T., Paalvast, M., Boogaard, L., Maseda, M., Bacon, R., Blaizot, J., Brinchmann, J., Epinat, B., Feltre, A., Marino, R. A., Muzahid, S., Richard, J., Schaye, J., Verhamme, A., Weilbacher, P. M., and Wisotzki, L.: 2017, *A&A* **608**, A7

Fletcher, T. J., Tang, M., Robertson, B. E., Nakajima, K., Ellis, R. S., Stark, D. P., and Inoue, A.: 2019, *The Astrophysical Journal* **878(2)**, 87

Flury, S., Jaskot, A. E., Ferguson, H., Worseck, G., Makan, K., Chisholm, J., Saldana-Lopez, A., Schaerer, D., McCandliss, S., Wang, B., Ford, N. M., Oey, M. S., Heckman, T. M., Ji, Z., Giavalisco, M., Amorín, R., Atek, H., Blaizot, J., Borthakur, S., Carr, C., Castellano, M., De Barros, S., Dickinson, M., Finkelstein, S. L., Fleming, B., Fontanot, F., Garel, T., Grazian, A., Hayes, M., Henry, A., Mauerhofer, V., Micheva, G., Östlin, G., Papovich, C., Pentericci, L., Ravindranath, S., Rosdahl,

J., Rutkowski, M., Santini, P., Scarlata, C., Teplitz, H., Thuan, T., Trebitsch, M., Vanzella, E., Verhamme, A., and Xu, X.: 2021a, *in prep.*

Flury, S., Jaskot, A. E., Ferguson, H., Worseck, G., Makan, K., Chisholm, J., Saldana-Lopez, A., Schaerer, D., McCandliss, S., Wang, B., Ford, N. M., Oey, M. S., Heckman, T. M., Ji, Z., Giavalisco, M., Amorín, R., Atek, H., Blaizot, J., Borthakur, S., Carr, C., Castellano, M., De Barros, S., Dickinson, M., Finkelstein, S. L., Fleming, B., Fontanot, F., Garel, T., Grazian, A., Hayes, M., Henry, A., Mauerhofer, V., Micheva, G., Östlin, G., Papovich, C., Pentericci, L., Ravindranath, S., Rosdahl, J., Rutkowski, M., Santini, P., Scarlata, C., Teplitz, H., Thuan, T., Trebitsch, M., Vanzella, E., and Verhamme, A.: 2021b, *in prep.*

Gazagnes, S., Chisholm, J., Schaerer, D., Verhamme, A., and Izotov, Y.: 2020, *A&A* **639**, A85

Gazagnes, S., Chisholm, J., Schaerer, D., Verhamme, A., Rigby, J. R., and Bayliss, M.: 2018, *A&A* **616**, A29

Giallongo, E., Grazian, A., Fiore, F., Fontana, A., Pentericci, L., Vanzella, E., Dickinson, M., Kocevski, D., Castellano, M., Cristiani, S., Ferguson, H., Finkelstein, S., Grogin, N., Hathi, N., Koekemoer, A. M., Newman, J. A., and Salvato, M.: 2015, *A&A* **578**, A83

Green, J. C., Froning, C. S., Osterman, S., Ebbets, D., Heap, S. H., Leitherer, C., Linsky, J. L., Savage, B. D., Sembach, K., Shull, J. M., Siegmund, O. H. W., Snow, T. P., Spencer, J., Stern, S. A., Stocke, J., Welsh, B., Béland, S., Burgh, E. B.,

Danforth, C., France, K., Keeney, B., McPhate, J., Penton, S. V., Andrews, J., Brownsberger, K., Morse, J., and Wilkinson, E.: 2012, *ApJ* **744**, 60

Gronke, M. and Oh, S. P.: 2018, *MNRAS* **480(1)**, L111

Gronke, M. and Oh, S. P.: 2020, *MNRAS* **492(2)**, 1970

Gunn, J. E. and Peterson, B. A.: 1965, *ApJ* **142**, 1633

Heckman, T. M., Alexandroff, R. M., Borthakur, S., Overzier, R., and Leitherer, C.: 2015, *ApJ* **809(2)**, 147

Heckman, T. M., Armus, L., and Miley, G. K.: 1990, *ApJS* **74**, 833

Heckman, T. M., Borthakur, S., Overzier, R., Kauffmann, G., Basu-Zych, A., Leitherer, C., Sembach, K., Martin, D. C., Rich, R. M., Schiminovich, D., and Seibert, M.: 2011, *ApJ* 730(1)

Heckman, T. M., Lehnert, M. D., Strickland, D. K., and Armus, L.: 2000, *ApJS* **129(2)**, 493

Heckman, T. M., Robert, C., Leitherer, C., Garnett, D. R., and van der Rydt, F.: 1998, *ApJ* **503(2)**, 646

Heckman, T. M. and Thompson, T. A.: 2017, *arXiv e-prints* p. arXiv:1701.09062

Henry, A., Berg, D. A., Scarlata, C., Verhamme, A., and Erb, D.: 2018, *ApJ* **855(2)**, 96

Hogarth, L., Amorín, R., Vílchez, J. M., Hägele, G. F., Cardaci, M., Pérez-Montero, E., Firpo, V., Jaskot, A., and Chávez, R.: 2020, *MNRAS* **494(3)**, 3541

Hopkins, P. F., Cox, T. J., Hernquist, L., Narayanan, D., Hayward, C. C., and Murray, N.: 2013, *MNRAS* **430(3)**, 1901

Hui, L. and Haiman, Z.: 2003, *ApJ* **596(1)**, 9

Ishigaki, M., Kawamata, R., Ouchi, M., Oguri, M., Shimasaku, K., and Ono, Y.: 2018, *ApJ* **854(1)**, 73

Isobe, T., Feigelson, E. D., and Nelson, P. I.: 1986, *ApJ* **306**, 490

Izotov, Y. I., Orlitová, I., Schaerer, D., Thuan, T. X., Verhamme, A., Guseva, N. G., and Worseck, G.: 2016a, *Nature* **529(7585)**, 178

Izotov, Y. I., Schaerer, D., Thuan, T. X., Worseck, G., Guseva, N. G., Orlitová, I., and Verhamme, A.: 2016b, *MNRAS* **461(4)**, 3683

Izotov, Y. I., Schaerer, D., Worseck, G., Guseva, N. G., Thuan, T. X., Verhamme, A., Orlitová, I., and Fricke, K. J.: 2018a, *MNRAS* **474(4)**, 4514

Izotov, Y. I., Worseck, G., Schaerer, D., Guseva, N. G., Chisholm, J., Thuan, T. X., Fricke, K. J., and Verhamme, A.: 2021, *MNRAS* **503(2)**, 1734

Izotov, Y. I., Worseck, G., Schaerer, D., Guseva, N. G., Thuan, T. X., Fricke, K. J., Verhamme, A., and Orlitová, I.: 2018b, *MNRAS* **478(4)**, 4851

Jaskot, A. E., Dowd, T., Oey, M. S., Scarlata, C., and McKinney, J.: 2019, *ApJ* **885(1)**, 96

Jones, T., Stark, D. P., and Ellis, R. S.: 2012, *ApJ* **751(1)**, 51

Katz, H., Ďurovčíková, D., Kimm, T., Rosdahl, J., Blaizot, J., Haehnelt, M. G., Devriendt, J., Slyz, A., Ellis, R., and Laporte, N.: 2020, *MNRAS* **498(1)**, 164

Kennicutt, R. C. and Evans, N. J.: 2012, *ARA&A* **50(1)**, 531

Kewley, L. J., Groves, B., Kauffmann, G., and Heckman, T.: 2006, *MNRAS* **372(3)**, 961

Kim, K., Malhotra, S., Rhoads, J. E., Butler, N. R., and Yang, H.: 2020, *ApJ* **893(2)**, 134

Kim, K. J., Malhotra, S., Rhoads, J. E., and Yang, H.: 2021, *arXiv e-prints* p. arXiv:2104.08282

Koekemoer, A. M., Ellis, R. S., McLure, R. J., Dunlop, J. S., Robertson, B. E., Ono, Y., Schenker, M. A., Ouchi, M., Bowler, R. A. A., Rogers, A. B., Curtis-Lake, E., Schneider, E., Charlot, S., Stark, D. P., Furlanetto, S. R., Cirasuolo, M., Wild, V., and Targett, T.: 2013, *ApJS* **209(1)**, 3

Kornei, K. A., Shapley, A. E., Martin, C. L., Coil, A. L., Lotz, J. M., and Weiner, B. J.: 2013, *ApJ* **774(1)**, 50

Kroupa, P.: 2001, *MNRAS* **322(2)**, 231

Kroupa, P.: 2002, *Science* **295(5552)**, 82

Kuhlen, M. and Faucher-Giguère, C.-A.: 2012, *MNRAS* **423(1)**, 862

Lacey, C. G., Baugh, C. M., Frenk, C. S., Benson, A. J., Bower, R. G., Cole, S., Gonzalez-Perez, V., Helly, J. C., Lagos, C. D. P., and Mitchell, P. D.: 2016, *MNRAS* **462(4)**, 3854

Leitherer, C., Hernandez, S., Lee, J. C., and Oey, M. S.: 2016, *ApJ* **823(1)**, 64

Leitherer, C., Ortiz Otálvaro, P. A., Bresolin, F., Kudritzki, R.-P., Lo Faro, B., Pauldrach, A. W. A., Pettini, M., and Rix, S. A.: 2010, *ApJS* **189(2)**, 309

Leitherer, C., Schaerer, D., Goldader, J. D., Delgado, R. M. G., Robert, C., Kune, D. F., de Mello, D. F., Devost, D., and Heckman, T. M.: 1999, *ApJS* **123(1)**, 3

Lochhaas, C., Thompson, T. A., Quataert, E., and Weinberg, D. H.: 2018, *MNRAS* **481(2)**, 1873

Lotz, J. M., Koekemoer, A., Coe, D., Grogin, N., Capak, P., Mack, J., Anderson, J., Avila, R., Barker, E. A., Borncamp, D., Brammer, G., Durbin, M., Gunning, H., Hilbert, B., Jenkner, H., Khandrika, H., Levay, Z., Lucas, R. A., MacKenty, J., Ogaz, S., Porterfield, B., Reid, N., Robberto, M., Royle, P., Smith, L. J., Storrie-Lombardi, L. J., Sunnquist, B., Surace, J., Taylor, D. C., Williams, R., Bullock, J., Dickinson, M., Finkelstein, S., Natarajan, P., Richard, J., Robertson, B., Tumlinson, J., Zitrin, A., Flanagan, K., Sembach, K., Soifer, B. T., and Mountain, M.: 2017, *ApJ* **837(1)**, 97

Madau, P. and Haardt, F.: 2015, *ApJL* **813(1)**, L8

Madau, P., Haardt, F., and Rees, M. J.: 1999, *ApJ* **514(2)**, 648

Madau, P., Pozzetti, L., and Dickinson, M.: 1998, *ApJ* **498(1)**, 106

Maiolino, R., Nagao, T., Grazian, A., Cocchia, F., Marconi, A., Mannucci, F., Cimatti, A., Pipino, A., Ballero, S., Calura, F., Chiappini, C., Fontana, A.,

Granato, G. L., Matteucci, F., Pastorini, G., Pentericci, L., Risaliti, G., Salvati, M., and Silva, L.: 2008, *A&A* **488(2)**, 463

Marchi, F., Pentericci, L., Guaita, L., Schaerer, D., Verhamme, A., Castellano, M., Ribeiro, B., Garilli, B., Le Fèvre, O., Amorin, R., Bardelli, S., Cassata, P., Durkalec, A., Grazian, A., Hathi, N. P., Lemaux, B. C., Maccagni, D., Vanzella, E., and Zucca, E.: 2018, *A&A* **614**, A11

Mathis, J.: 1990, *ARA&A* **28(1)**, 37

McCully, C., Crawford, S., Kovacs, G., Tollerud, E., Betts, E., Bradley, L., Craig, M., Turner, J., Streicher, O., Sipocz, B., Robitaille, T., and Deil, C.: 2018, *astropy/astroscrappy: v1.0.5 Zenodo Release*

McLeod, D. J., McLure, R. J., and Dunlop, J. S.: 2016, *MNRAS* **459(4)**, 3812

McQuinn, M.: 2016, *ARA&A*

McQuinn, M., Oh, S. P., and Faucher-Giguère, C.-A.: 2011, *ApJ* **743(1)**, 82

Meynet, G., Maeder, A., Schaller, G., Schaerer, D., and Charbonnel, C.: 1994, *A&AS* **103**, 97

Michel-Dansac, L., Blaizot, J., Garel, T., Verhamme, A., Kimm, T., and Trebitsch, M.: 2020, *A&A* **635**, A154

Mostardi, R. E., Shapley, A. E., Steidel, C. C., Trainor, R. F., Reddy, N. A., and Siana, B.: 2015, *ApJ* **810(2)**, 107

Naidu, R. P., Tacchella, S., Mason, C. A., Bose, S., Oesch, P. A., and Conroy, C.: 2020, *ApJ* **892(2)**, 109

Nakajima, K., Ellis, R. S., Robertson, B. E., Tang, M., and Stark, D. P.: 2020, *ApJ* **889(2)**, 161

Oesch, P. A., Bouwens, R. J., Illingworth, G. D., Labbé, I., Smit, R., Franx, M., van Dokkum, P. G., Momcheva, I., Ashby, M. L. N., Fazio, G. G., Huang, J. S., Willner, S. P., Gonzalez, V., Magee, D., Trenti, M., Brammer, G. B., Skelton, R. E., and Spitler, L. R.: 2014, *ApJ* **786(2)**, 108

Overzier, R. A., Heckman, T. M., Tremonti, C., Armus, L., Basu-Zych, A., Gonçalves, T., Rich, R. M., Martin, D. C., Ptak, A., Schiminovich, D., Ford, H. C., Madore, B., and Seibert, M.: 2009, *ApJ* **706(1)**, 203

Pellegrini, E. W., Oey, M. S., Winkler, P. F., Points, S. D., Smith, R. C., Jaskot, A. E., and Zastrow, J.: 2012, *ApJ* **755(1)**, 40

Pettini, M. and Pagel, B. E. J.: 2004, *MNRAS* **348(3)**, L59

Planck Collaboration, Aghanim, N., Akrami, Y., Arroja, F., Ashdown, M., Aumont, J., Baccigalupi, C., Ballardini, M., Banday, A. J., Barreiro, R. B., Bartolo, N., Basak, S., Battye, R., Benabed, K., Bernard, J. P., Bersanelli, M., Bielewicz, P., Bock, J. J., Bond, J. R., Borrill, J., Bouchet, F. R., Boulanger, F., Bucher, M., Burigana, C., Butler, R. C., Calabrese, E., Cardoso, J. F., Carron, J., Casaponsa, B., Challinor, A., Chiang, H. C., Colombo, L. P. L., Combet, C., Contreras, D., Crill, B. P., Cuttaia, F., de Bernardis, P., de Zotti, G., Delabrouille, J., Delouis, J. M., Désert, F. X., Di Valentino, E., Dickinson, C., Diego, J. M., Donzelli, S., Doré, O., Douspis, M., Ducout, A., Dupac, X., Efstathiou, G., Elsner, F., Enßlin, T. A., Eriksen, H. K., Falgarone, E., Fantaye, Y., Fergusson, J., Fernandez-Cobos, R.,

Finelli, F., Forastieri, F., Frailis, M., Franceschi, E., Frolov, A., Galeotta, S., Galli, S., Ganga, K., Génova-Santos, R. T., Gerbino, M., Ghosh, T., González-Nuevo, J., Górski, K. M., Gratton, S., Gruppuso, A., Gudmundsson, J. E., Hamann, J., Handley, W., Hansen, F. K., Helou, G., Herranz, D., Hildebrandt, S. R., Hivon, E., Huang, Z., Jaffe, A. H., Jones, W. C., Karakci, A., Keihänen, E., Keskitalo, R., Kiiveri, K., Kim, J., Kisner, T. S., Knox, L., Krachmalnicoff, N., Kunz, M., Kurki-Suonio, H., Lagache, G., Lamarre, J. M., Langer, M., Lasenby, A., Lattanzi, M., Lawrence, C. R., Le Jeune, M., Leahy, J. P., Lesgourgues, J., Levrier, F., Lewis, A., Liguori, M., Lilje, P. B., Lilley, M., Lindholm, V., López-Caniego, M., Lubin, P. M., Ma, Y. Z., Macías-Pérez, J. F., Maggio, G., Maino, D., Mandolesi, N., Mangilli, A., Marcos-Caballero, A., Maris, M., Martin, P. G., Martinelli, M., Martínez-González, E., Matarrese, S., Mauri, N., McEwen, J. D., Meerburg, P. D., Meinhold, P. R., Melchiorri, A., Mennella, A., Migliaccio, M., Millea, M., Mitra, S., Miville-Deschênes, M. A., Molinari, D., Moneti, A., Montier, L., Morgante, G., Moss, A., Mottet, S., Münchmeyer, M., Natoli, P., Nørgaard-Nielsen, H. U., Oxborrow, C. A., Pagano, L., Paoletti, D., Partridge, B., Patanchon, G., Pearson, T. J., Peel, M., Peiris, H. V., Perrotta, F., Pettorino, V., Piacentini, F., Polastri, L., Polenta, G., Puget, J. L., Rachen, J. P., Reinecke, M., Remazeilles, M., Renault, C., Renzi, A., Rocha, G., Rosset, C., Roudier, G., Rubiño-Martín, J. A., Ruiz-Granados, B., Salvati, L., Sandri, M., Savelainen, M., Scott, D., Shellard, E. P. S., Shiraishi, M., Sirignano, C., Sirri, G., Spencer, L. D., Sunyaev, R., Suur-Uski, A. S., Tauber, J. A., Tavagnacco, D., Tenti, M., Terenzi, L., Toffolatti, L., Tomasi, M., Trombetti, T., Valiviita, J., Van Tent, B., Vibert, L., Vielva, P., Villa, F., Vittorio, N., Wandelt, B. D., Wehus, I. K., White, M., White, S. D. M.,

Zacchei, A., and Zonca, A.: 2020a, *A&A* **641**, A1

Planck Collaboration, Aghanim, N., Akrami, Y., Ashdown, M., Aumont, J., Baccigalupi, C., Ballardini, M., Banday, A. J., Barreiro, R. B., Bartolo, N., Basak, S., Battye, R., Benabed, K., Bernard, J. P., Bersanelli, M., Bielewicz, P., Bock, J. J., Bond, J. R., Borrill, J., Bouchet, F. R., Boulanger, F., Bucher, M., Burigana, C., Butler, R. C., Calabrese, E., Cardoso, J. F., Carron, J., Challinor, A., Chiang, H. C., Chluba, J., Colombo, L. P. L., Combet, C., Contreras, D., Crill, B. P., Cuttaia, F., de Bernardis, P., de Zotti, G., Delabrouille, J., Delouis, J. M., Di Valentino, E., Diego, J. M., Doré, O., Douspis, M., Ducout, A., Dupac, X., Dusini, S., Efstathiou, G., Elsner, F., Enßlin, T. A., Eriksen, H. K., Fantaye, Y., Farhang, M., Fergusson, J., Fernandez-Cobos, R., Finelli, F., Forastieri, F., Frailis, M., Fraisse, A. A., Franceschi, E., Frolov, A., Galeotta, S., Galli, S., Ganga, K., Génova-Santos, R. T., Gerbino, M., Ghosh, T., González-Nuevo, J., Górski, K. M., Gratton, S., Gruppuso, A., Gudmundsson, J. E., Hamann, J., Handley, W., Hansen, F. K., Herranz, D., Hildebrandt, S. R., Hivon, E., Huang, Z., Jaffe, A. H., Jones, W. C., Karakci, A., Keihänen, E., Keskitalo, R., Kiiveri, K., Kim, J., Kisner, T. S., Knox, L., Krachmalnicoff, N., Kunz, M., Kurki-Suonio, H., Lagache, G., Lamarre, J. M., Lasenby, A., Lattanzi, M., Lawrence, C. R., Le Jeune, M., Lemos, P., Lesgourgues, J., Levrier, F., Lewis, A., Liguori, M., Lilje, P. B., Lilley, M., Lindholm, V., López-Caniego, M., Lubin, P. M., Ma, Y. Z., Macías-Pérez, J. F., Maggio, G., Maino, D., Mandolesi, N., Mangilli, A., Marcos-Caballero, A., Maris, M., Martin, P. G., Martinelli, M., Martínez-González, E., Matarrese, S., Mauri, N., McEwen, J. D., Meinhold, P. R., Melchiorri, A., Mennella, A., Migliaccio, M., Millea, M., Mitra, S., Miville-Deschênes, M. A., Molinari, D., Montier, L., Morgante, G., Moss,

A., Natoli, P., Nørgaard-Nielsen, H. U., Pagano, L., Paoletti, D., Partridge, B., Patanchon, G., Peiris, H. V., Perrotta, F., Pettorino, V., Piacentini, F., Polastri, L., Polenta, G., Puget, J. L., Rachen, J. P., Reinecke, M., Remazeilles, M., Renzi, A., Rocha, G., Rosset, C., Roudier, G., Rubiño-Martín, J. A., Ruiz-Granados, B., Salvati, L., Sandri, M., Savelainen, M., Scott, D., Shellard, E. P. S., Sirignano, C., Sirri, G., Spencer, L. D., Sunyaev, R., Suur-Uski, A. S., Tauber, J. A., Tavagnacco, D., Tenti, M., Toffolatti, L., Tomasi, M., Trombetti, T., Valenziano, L., Valiviita, J., Van Tent, B., Vibert, L., Vielva, P., Villa, F., Vittorio, N., Wandelt, B. D., Wehus, I. K., White, M., White, S. D. M., Zacchei, A., and Zonca, A.: 2020b, *A&A* **641**, A6

Prochaska, J. X., Kasen, D., and Rubin, K.: 2011, *ApJ* **734(1)**, 24

Ramambason, L., Schaerer, D., Stasińska, G., Izotov, Y. I., Guseva, N. G., Vílchez, J. M., Amorín, R., and Morisset, C.: 2020, *A&A* **644**, A21

Reddy, N. A., Kriek, M., Shapley, A. E., Freeman, W. R., Siana, B., Coil, A. L., Mobasher, B., Price, S. H., Sanders, R. L., and Shivaei, I.: 2015, *ApJ* **806(2)**, 259

Reddy, N. A., Pettini, M., Steidel, C. C., Shapley, A. E., Erb, D. K., and Law, D. R.: 2012, *ApJ* **754(1)**, 25

Reddy, N. A., Steidel, C. C., Pettini, M., and Bogosavljevic, M.: 2016, *ApJ*

Robertson, B. E., Ellis, R. S., Furlanetto, S. R., and Dunlop, J. S.: 2015, *ApJ* **802(2)**, L19

Robertson, B. E., Furlanetto, S. R., Schneider, E., Charlot, S., Ellis, R. S., Stark, D. P., McLure, R. J., Dunlop, J. S., Koekemoer, A., Schenker, M. A., Ouchi, M.,

Ono, Y., Curtis-Lake, E., Rogers, A. B., Bowler, R. A. A., and Cirasuolo, M.: 2013, *ApJ* **768(1)**, 71

Rubin, K. H. R., Prochaska, J. X., Ménard, B., Murray, N., Kasen, D., Koo, D. C., and Phillips, A. C.: 2011, *ApJ* **728(1)**, 55

Runnholm, A., Hayes, M., Melinder, J., Rivera-Thorsen, E., Östlin, G., Cannon, J., and Kunth, D.: 2020, *ApJ* **892(1)**, 48

Saldana-Lopez, A., Schaerer, D., Chisholm, J., Flury, S., Jaskot, A. E., Gábor, Makan, K., Gazagnes, S., Mauerhofer, V., Verhamme, A., Amorín, R., Ferguson, H. C., Giavalisco, M., Grazian, A., Hayes, M. J., Heckman, T. M., Henry, A., Ji, Z., Marques-Chaves, R., McCandliss, S., Oey, M. S., Östlin, G., Pentericci, L., Thuan, T. X., Trebitsch, M., Vanzella, E., and Xu, X.: 2021, *in prep.*

Scarlata, C. and Panagia, N.: 2015, *ApJ* **801(1)**, 43

Schechter, P.: 1976, *ApJ* **203**, 297

Schneider, E. E., Robertson, B. E., and Thompson, T. A.: 2018, *ApJ* **862(1)**, 56

Sheth, R. K., Mo, H. J., and Tormen, G.: 2001, *MNRAS* **323(1)**, 1

Shopbell, P. L. and Bland-Hawthorn, J.: 1998, *ApJ* **493(1)**, 129

Somerville, R. S. and Davé, R.: 2015, *ARA&A* **53(1)**, 51

Springel, V., White, S. D. M., Jenkins, A., Frenk, C. S., Yoshida, N., Gao, L., Navarro, J., Thacker, R., Croton, D., Helly, J., Peacock, J. A., Cole, S., Thomas, P., Couchman, H., Evrard, A., Colberg, J., and Pearce, F.: 2005, *Nature* **435(7042)**, 629

Steidel, C. C., Bogosavljević, M., Shapley, A. E., Kollmeier, J. A., Reddy, N. A., Erb, D. K., and Pettini, M.: 2011, *ApJ* **736(2)**, 160

Steidel, C. C., Bogosavljević, M., Shapley, A. E., Reddy, N. A., Rudie, G. C., Pettini, M., Trainor, R. F., and Strom, A. L.: 2018, *ApJ* **869(2)**, 123

Steidel, C. C., Pettini, M., and Adelberger, K. L.: 2001, *ApJ* **546(2)**, 665

Strom, A. L., Steidel, C. C., Rudie, G. C., Trainor, R. F., and Pettini, M.: 2018, *ApJ* **868(2)**, 117

Tang, Y., Giavalisco, M., Guo, Y., and Kurk, J.: 2014, *ApJ* **793(2)**, 92

Thomas, D., Steele, O., Maraston, C., Johansson, J., Beifiori, A., Pforr, J., Strömbäck, G., Tremonti, C. A., Wake, D., Bizyaev, D., Bolton, A., Brewington, H., Brownstein, J. R., Comparat, J., Kneib, J.-P., Malanushenko, E., Malanushenko, V., Oravetz, D., Pan, K., Parejko, J. K., Schneider, D. P., Shelden, A., Simmons, A., Snedden, S., Tanaka, M., Weaver, B. A., and Yan, R.: 2013, *MNRAS* **431**, 1383

Thompson, T. A., Quataert, E., Zhang, D., and Weinberg, D. H.: 2016, *MNRAS* **455(2)**, 1830

Topping, M. W., Shapley, A. E., Reddy, N. A., Sanders, R. L., Coil, A. L., Kriek, M., Mobasher, B., and Siana, B.: 2020, *MNRAS* **4444**, 4430

van Dokkum, P. G.: 2001, *PASP* **113(789)**, 1420

Vanzella, E., Caminha, G. B., Calura, F., Cupani, G., Meneghetti, M., Castellano, M., Rosati, P., Mercurio, A., Sani, E., Grillo, C., Gilli, R., Mignoli, M., Comastri,

A., Nonino, M., Cristiani, S., Giavalisco, M., and Caputi, K.: 2020, *MNRAS* **491(1)**, 1093

Vanzella, E., de Barros, S., Castellano, M., Grazian, A., Inoue, A. K., Schaerer, D., Guaita, L., Zamorani, G., Giavalisco, M., Siana, B., Pentericci, L., Giallongo, E., Fontana, A., and Vignali, C.: 2015, *A&A* **576**, A116

Vanzella, E., Nonino, M., Cupani, G., Castellano, M., Sani, E., Mignoli, M., Calura, F., Meneghetti, M., Gilli, R., Comastri, A., Mercurio, A., Caminha, G. B., Caputi, K., Rosati, P., Grillo, C., Cristiani, S., Balestra, I., Fontana, A., and Giavalisco, M.: 2018, *MNRAS* **476(1)**, L15

Veilleux, S., Cecil, G., and Bland-Hawthorn, J.: 2005, *ARA&A* **43(1)**, 769

Veilleux, S., Maiolino, R., Bolatto, A. D., and Aalto, S.: 2020, *A&A Rv* **28(1)**, 2

Veilleux, S. and Osterbrock, D. E.: 1987, *ApJS* **63**, 295

Verhamme, A., Orlitová, I., Schaerer, D., and Hayes, M.: 2015, *A&A* **578**, A7

Verhamme, A., Orlitová, I., Schaerer, D., Izotov, Y., Worseck, G., Thuan, T. X., and Guseva, N.: 2017, *A&A* **597**, A13

Vogelsberger, M., Marinacci, F., Torrey, P., and Puchwein, E.: 2020, *Nature Reviews Physics* **2(1)**, 42

Wang, B., Heckman, T. M., Amorín, R., Borthakur, S., Chisholm, J., Ferguson, H., Flury, S., Giavalisco, M., Grazian, A., Hayes, M., Henry, A., Jaskot, A., Ji, Z., Makan, K., McCandliss, S., Oey, M. S., Östlin, G., Saldana-Lopez, A., Schaerer, D., Thuan, T., Worseck, G., and Xu, X.: 2021, *ApJ* **916(1)**, 3

Wang, B., Heckman, T. M., Leitherer, C., Alexandroff, R., Borthakur, S., and Overzier, R. A.: 2019, *ApJ* **885(1)**, 57

Wang, B., Heckman, T. M., Zhu, G., and Norman, C. A.: 2020, *ApJ* **894(2)**, 149

Worseck, G., Prochaska, J. X., Hennawi, J. F., and McQuinn, M.: 2016, *ApJ* **825(2)**, 144

Wright, E. L., Eisenhardt, P. R. M., Mainzer, A. K., Ressler, M. E., Cutri, R. M., Jarrett, T., Kirkpatrick, J. D., Padgett, D., McMillan, R. S., Skrutskie, M., Stanford, S. A., Cohen, M., Walker, R. G., Mather, J. C., Leisawitz, D., Gautier, Thomas N., I., McLean, I., Benford, D., Lonsdale, C. J., Blain, A., Mendez, B., Irace, W. R., Duval, V., Liu, F., Royer, D., Heinrichsen, I., Howard, J., Shannon, M., Kendall, M., Walsh, A. L., Larsen, M., Cardon, J. G., Schick, S., Schwalm, M., Abid, M., Fabinsky, B., Naes, L., and Tsai, C.-W.: 2010, *AJ* **140(6)**, 1868

Zackrisson, E., Inoue, A. K., and Jensen, H.: 2013, *ApJ* **777(1)**, 39

Zastrow, J., Oey, M. S., Veilleux, S., McDonald, M., and Martin, C. L.: 2011, *ApJL* **741(1)**, L17

Zhu, G. B., Comparat, J., Kneib, J.-P., Delubac, T., Raichoor, A., Dawson, K. S., Newman, J., Yèche, C., Zhou, X., and Schneider, D. P.: 2015, *ApJ* **815(1)**, 48

Vita

Bingjie Wang was born in Shanghai, China. She received the degree of the Bachelor of Arts in Philosophy, and the degree of the Bachelor of Philosophy in Physics with honors from the University of Pittsburgh in 2016, graduating magna cum laude. She was inducted into the ΣΠΣ national physics honors society the same year. Wang became a graduate student in Physics and Astronomy at the Johns Hopkins University in 2016, and received the degree of the Doctor of Philosophy in Astrophysics in 2021 for her dissertation on understanding the cosmic reionization from the local universe. She was awarded the Rodger Doxsey Travel Prize from the American Astronomical Society in 2020. She is currently a junior member of the American Astronomical Society.